



SAPIENZA  
UNIVERSITÀ DI ROMA

## Anatomy of a binary neutron star merger

Facoltà di Scienze Matematiche Fisiche e Naturali  
Corso di Laurea Magistrale in Astronomia e Astrofisica

Candidate

Lavinia Paiella

ID number 1808256

Thesis Advisor

Prof. Paolo Pani

Co-Advisor

Prof. Andrea Maselli

Academic Year 2021/2022

---

**Anatomy of a binary neutron star merger**

Master's thesis. Sapienza – University of Rome

© 2022 Lavinia Paiella. All rights reserved

This thesis has been typeset by L<sup>A</sup>T<sub>E</sub>X and the Sapthesis class.

Author's email: [paiella.1808256@studenti.uniroma1.it](mailto:paiella.1808256@studenti.uniroma1.it)

*Ai miei due grandi eroi di sempre,*

## Abstract

The joint detection of the gravitational-wave signal GW170817 and its electromagnetic counterparts, the gamma-ray-burst GRB170817A and the kilonova AT2017gfo, marked the beginning of multimessenger astrophysics. This ensemble of observations showed the unique potential of gravitational wave astronomy to enhance our understanding of fundamental physics laws, and to study phenomena hardly reproducible with terrestrial experiments. Among the latter, binary neutron star observations opened a new window to explore the extreme density regimes reached by nuclear matter within the stellar cores.

In this thesis we carried out a new study aimed to infer direct information on the properties of nucleon dynamics at supra-nuclear densities exploiting joint gravitational-wave and electromagnetic observations. In particular, we built a numerical pipeline which combines the information carried by the inspiral gravitational-wave signal, with the post-merger kilonova emission, to directly probe the behavior of three-body nucleon repulsive forces within the neutron cores. The amplitude of such interactions, which we introduced in our equation of state as a free parameter, determines the stiffness of nuclear matter, and hence the stellar observables. We analysed both simulated and real gravitational wave and kilonova datasets, focusing for the latter on GW170817 and AT2017gfo. For mock signals, we applied our pipeline to current and future detectors comparing their sensitivity to constrain the microphysical features of the equation of state. Our results show that the introduction of a 3rd generation interferometer, such as the Einstein Telescope, leads to remarkable improvements on the accuracy with which the properties of nucleon dynamics can be inferred. Working with real observations, our analysis provides the first constraint on repulsive three-body nucleon forces based on GW170817 multimessenger data. These results support stellar configurations with mildly-stiff equations of state, and are fully consistent with other constraints derived from gravitational-wave and electromagnetic analyses.

# Contents

<b>1</b>	<b>Introduction</b>	<b>1</b>
<b>2</b>	<b>Neutron stars</b>	<b>3</b>
2.1	Origin and composition . . . . .	3
2.2	Relativistic overview of a neutron star . . . . .	5
2.2.1	Basic ingredients of General Relativity . . . . .	5
2.2.2	Stellar equations . . . . .	7
2.3	The equation of state . . . . .	9
2.3.1	Thermodynamics and barotropic EoS . . . . .	9
2.3.2	Non-relativistic many body nuclear model . . . . .	11
2.4	Love numbers . . . . .	13
2.4.1	Love Numbers in a Newtonian framework . . . . .	13
2.4.2	Love Numbers in a Relativistic framework . . . . .	24
<b>3</b>	<b>Neutron star mergers</b>	<b>32</b>
3.1	System evolution . . . . .	32
3.1.1	Formation, inspiral and merger . . . . .	32
3.1.2	Post-merger evolution and fate of the remnant . . . . .	33
3.2	Gravitational wave emission . . . . .	34
3.2.1	Inspiral emission and tidal imprint . . . . .	35
3.2.2	Merger and post-merger emission . . . . .	36
3.3	Kilonovae . . . . .	39
3.3.1	Toy model . . . . .	39
3.3.2	The role of opacity: blue and red kilonova . . . . .	40
3.3.3	Multi-component model . . . . .	41
<b>4</b>	<b>Bayesian inference</b>	<b>44</b>
4.1	Bayes theorem . . . . .	44
4.2	Parameter estimation . . . . .	45
4.3	Monte Carlo Markov Chains . . . . .	46
4.3.1	Metropolis-Hastings algorithm . . . . .	48
4.4	Affine invariant MCMC sampling . . . . .	50
4.5	Our case of study: retrieving nucleon interactions . . . . .	52
4.5.1	Inference framework . . . . .	52
4.5.2	Sampling procedure . . . . .	53
<b>5</b>	<b>Multimessenger analysis of neutron star mergers</b>	<b>55</b>
5.1	GW170817 and GW190425 . . . . .	56
5.1.1	Code overview . . . . .	56
5.1.2	Mock signals parameter estimation . . . . .	61
5.1.3	Retrieving $\alpha$ . . . . .	73

5.2	AT2017gfo . . . . .	77
5.2.1	Code overview . . . . .	78
5.2.2	Real data . . . . .	81
5.2.3	Mock data . . . . .	82
5.3	Multimessenger analysis of GW170817 and AT2017gfo . . . . .	84
5.3.1	Real data . . . . .	85
5.3.2	Mock data . . . . .	88
<b>6</b>	<b>Conclusions</b>	<b>90</b>
<b>A</b>	<b>Example code in bilby</b>	<b>94</b>
	<b>Bibliography</b>	<b>101</b>

# Chapter 1

## Introduction

*Neutron stars (NS)* are among the most compact objects in the Universe. Matter within their cores is compressed to such a degree that it may exceed several times the density of atomic nuclei,  $\rho_0 = 2.7 \cdot 10^{14} \text{ g/cm}^3$ , and its behaviour, encoded by the so-called *equation of state (EoS)*, is challenging to constrain, at present time, with terrestrial experiments.

Neutron stars can evolve as binary systems and eventually coalesce through the emission of *gravitational waves (GWs)*, which subtract energy and angular momentum from the binary, leading its orbital separation to shrink up to the merger. Gravitational waves are ripples in the space-time which travel at the speed of light, produced by time-varying distribution of matter and energy with a certain degree of asymmetry, and represent a gold mine of information on the properties of astrophysical compact objects. Indeed, unlike electromagnetic radiation, they weakly interact with any astrophysical environment between the source and the observer, leaving all the information on the former almost intact. For NS binaries, the equation of state leaves a detectable footprint on the emitted gravitational waves through tidal interactions, which act predominantly in the late stages of the coalescence, deforming the NSs and affecting their orbital evolution. The magnitude of the deformations is proportional to the so-called *Love Numbers* [Thorne & Campolattaro (1967); Hinderer (2008)], a set of quantities which depend on the stellar internal composition. Measurements or constraints on such parameters from GW signals emitted by coalescing binaries can therefore provide valuable insight on the NS EoS and help to disentangle the different models of nuclear matter proposed in literature, to date highly degenerate.

Alongside the GW emission, the coalescence of a NS binary is expected to power several other signals in the electromagnetic spectrum, such as the *kilonova*, a quasi-isotropic thermal emission observable in the UV-optical-infrared band and produced by the radioactive decay of the neutron-rich matter ejected in the coalescence. The ejection dynamics, and ultimately the kilonova features, depends on the composition of the binary progenitors (Metzger, 2020), and therefore offer a view on the stellar EoS complementary to the information carried by the Love numbers.

The study of the synergy between these two messengers, made possible after the combined detection on August 17 2017 of the GW event GW170817 (Abbott et al., 2017a) and its two electromagnetic counterparts, the gamma-ray burst GRB170817A and the kilonova AT2017gfo, is the main focus of this project. The goal of the thesis is twofold: (i) develop a data-analysis strategy to combines EOS-dependent observables from the inspiral phase of the coalescence and the post-merger kilonova emission

---

(ii) apply such approach to current and next generation of interferometers, like the Einstein Telescope, to determine their ability to constrain the behavior of nucleon dynamics above the saturation density. To these aims we built a numerical pipeline that combines the posterior distributions of the tidal deformability, a convenient quantity defined from the star mass, radius and Love Numbers and measured by GW observations, with the constraints inferred on parameters which determine the properties of kilonova spectra. Our goal is to exploit such data to constrain a specific feature of the EoS, namely the strength of the repulsive three-nucleon forces at supranuclear densities. The latter is encoded in our baseline model by the free parameter  $\alpha$ , which we hierarchically infer from the multimessenger observations described above.

Our analysis can be thought as composed of three parts. In the first part, we define an injection campaign of simulated GW signals based on the properties of GW170817 and GW190425 for the different detector configurations using `bilby`, a LIGO-Virgo Python library designed for Bayesian inference of compact binary coalescence events, and discuss the accuracy to which the injected values of  $\alpha$  are recovered from the GW signals in the different scenarios. In the second part we change focus to the kilonova AT2017gfo and obtain the posterior of the NS tidal deformabilities, masses, and, ultimately, of the parameter  $\alpha$  also generalizing this procedure to mock kilonovae spectra which could be produced by events similar to GW170817 and GW190425. In the third part we combine the studies conducted on the two emission channels tackled the first and second part introducing a novel approach to provide a multimessenger estimate of the parameter  $\alpha$ . We tested this method both on the observed data of the GW170817 and its kilonova AT2017gfo, and on GW and kilonova mock signals.

The thesis is structured as following. In Chapter 2 we review the NS structure and introduce the basic formalism needed to solve the relativistic equations of stellar structure in General Relativity, as well as to compute the Love Numbers both in a Newtonian and Relativistic framework. Furthermore, we describe the properties of the EoS currently understood and the baseline model chosen to describe nuclear interactions in the stellar cores, reviewing the dependence of the NS observables on the microphysical properties of nucleon dynamics. In Chapter 3 we discuss the evolution of a binary NS merger and describe the features of its GW and kilonova emission explaining how they are connected to the NS properties. In Chapter 4 we introduce the Bayesian inference approach based on Monte Carlo Markov Chains simulations, which were used to recover the posterior of  $\alpha$  from measurements of the NS tidal deformabilities and masses obtained by GW observations. Finally, in Chapter 5 we present and discuss the results of our analyses. Conclusions and the future prospects of the work are presented in Chapter 6.

# Chapter 2

## Neutron stars

### 2.1 Origin and composition

Neutron stars represent the endpoint for the stellar evolution of stars with masses in the interval  $M \in (8, 20)M_{\odot}$ . These stars are massive enough to undergo all the nuclear burning stages until  $^{56}\text{Fe}$  is synthesized from  $^{28}\text{Si}$  in the innermost regions. At this stage of its evolution the star presents the "onion structure" in Fig. 2.1. No further exothermic fusions are possible and the core is so hot and dense that heavy elements start photo-disintegrating into lighter ones. These reactions are endothermic and further subtract energy to the core, accelerating its collapse (Kippenhahn et al., 2012). Additionally, degenerate relativistic electrons in the core are captured by heavy nuclei through the inverse  $\beta$  decay reaction

$$(Z, N) + e^- \rightarrow (Z - 1, N + 1) + \nu_e , \quad (2.1)$$

gradually producing more neutron-rich nuclei (*neutronization* process). When the nuclei become too neutron rich they start to break up, releasing free neutrons in the environment. This *neutron drip* takes place when the central density of the core is  $\rho_c \gtrsim 10^{11} \text{ g/cm}^3$ . At  $\rho_c \sim 10^{14} \text{ g/cm}^3$  the degenerate neutron core is so rigid that it is almost incompressible and the outer layers of the stars falling onto it bounce back, producing a violent shock called *supernova*. The remnant of these explosion is a nebula at the center of which sits the dead core of the massive star, the neutron star. The latter is a very *compact objects* having a typical mass between 1-2  $M_{\odot}$  and radius of 10-14 km.

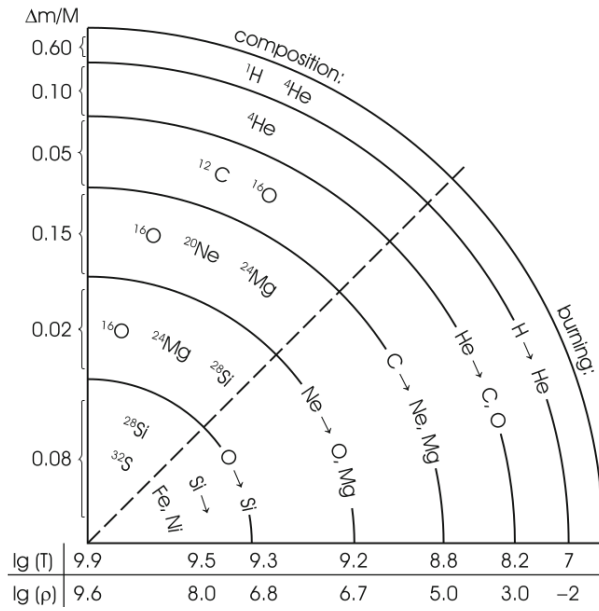


**Figure 2.1.** Schematic illustration of the internal structure of a highly evolved massive star. Along the vertical radius and below the horizontal radius are presented some typical values of the mass, the temperature (in K), and the density (in g/cm<sup>3</sup>) (Kippenhahn et al., 2012).

The model of the internal structure of a neutron star is presented in Figure 2.2. In the following we will denote the matter density of the neutron star with  $\rho$ . Proceeding from the outermost layers to the core, i.e. towards more dense regions, we encounter (Ferrari et al., 2020):

- the *outer crust* ( $\sim 10^7 \text{ g/cm}^3 < \rho < \rho_d = 4 \cdot 10^{11} \text{ g/cm}^3$ ). This region is composed of a lattice of heavy nuclei immersed in a gas of degenerate electrons which provides most of the pressure. Moving towards the next layer, density increases and electron captures become more efficient. Similarly to the neutronization of the core of the progenitor massive star, at  $\rho_d = 4 \cdot 10^{11} \text{ g/cm}^3$  neutrons can no longer live bound to the nuclei and start leaking out (neutron drip);
- the *inner crust* ( $\rho_d < \rho < \rho_0 = 2.67 \cdot 10^{14} \text{ g/cm}^3$ ). At these densities, the dominant contribution to the internal pressure is given by degenerate neutrons. Matter is composed of neutron rich nuclei, free neutrons and an electron gas which ensures charge neutrality. As the density increases matter re-arranges itself into different configurations (called *pasta phases*) until  $\rho$  reaches the *nuclear saturation density*,  $\rho_0$ , and protons, neutrons and electrons form a homogeneous fluid;
- the *outer core* ( $\rho_0 < \rho < 2\rho_0$ ). Here matter is composed of a homogeneous fluid of protons, neutrons and electrons in  $\beta$ -equilibrium, i.e. in equilibrium with respect to the reactions:

$$\begin{aligned} n &\rightarrow p + e^- + \bar{\nu}_e \\ e^- + p &\rightarrow n + \nu_e \end{aligned} . \quad (2.2)$$

The main contribution to the pressure is still given by neutrons which can, however, no longer be considered as non-interacting particles.

- the *inner core* ( $\rho \gtrsim 2\rho_0$ ). There is still much debate on what is the behaviour of matter at the extreme densities reached in the inner core of a NS. At these densities a wide variety of particles may form depending on the theoretical model for nuclear interactions assumed. Some of these models also hypothesize that if the density of the core reaches a value of  $\sim 10^{15} \text{ g/cm}^3$ , quarks may no longer be confined into nucleons or hadrons. In this case, NS matter is said to undergo a transition of phase.

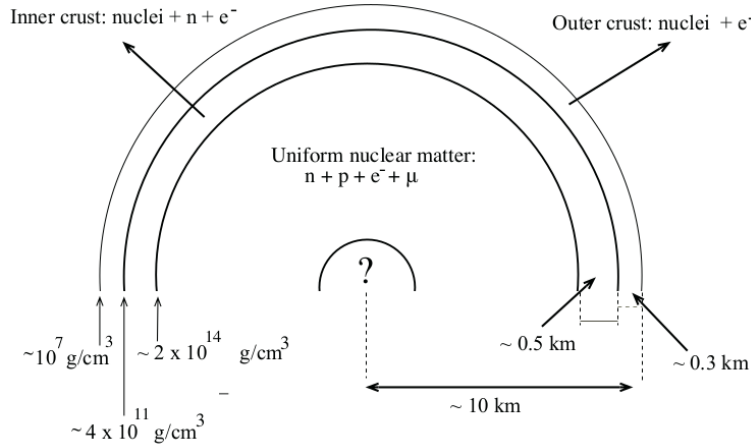


**Figure 2.2.** Schematic view of a NS internal structure (Ferrari et al., 2020).

As we shall see in Section 2.3, the behaviour of matter inside a NS is encoded by its EoS. The latter is a relation between the fundamental thermodynamical properties of the material to which it refers to, e.g. the density, temperature and pressure. In the case of NSs, there is quite general consensus on the EoS in the regions surrounding the core since the behaviour of matter at these densities is constrained by experimental data on neutron-rich nuclei. However, the densities reached in the innermost regions of NSs are, presently, very hard to reach in a laboratory and many different nuclear models are present in literature. Fortunately, these models can be constrained, to a certain extent, by astrophysical and gravitational wave observations of NSs. Indeed, it will be our intent in the last Chapter of this thesis to test the nuclear model which we will describe in 2.3.2, and assess the capability of next generation interferometers in recovering the information on nuclear interactions from the multimessenger emission of coalescing neutron star binaries.

## 2.2 Relativistic overview of a neutron star

### 2.2.1 Basic ingredients of General Relativity

Let us set the theoretical framework in which we will describe a neutron star, namely the one of *General Relativity (GR)*. General relativity is the theory of gravity formulated by Albert Einstein in 1915, based on two fundamental principles:

- *Strong Equivalence Principle*: at any given space-time point, it is possible to choose a *locally inertial reference frame (LIF)* such that, in the vicinity of that point, all laws of physics have the same form they would take without gravity, i.e. the one prescribed by Special Relativity.

- *Principle of General Covariance:* physical laws must have the same form in every coordinate system, i.e. they must be generally covariant.

As stated by the Strong Equivalence Principle, in a LIF the distance between two close points in time and space, two *events*, can be computed as in Special Relativity:

$$ds^2 = -c^2 dt^2 + dx^2 + dy^2 + dz^2 = \eta_{\mu\nu} dx^\mu dx^\nu , \quad (2.3)$$

where  $\eta^{\mu\nu}$  is the *Minkowski tensor*

$$\eta_{\mu\nu} = \begin{pmatrix} -1 & 0 & 0 & 0 \\ 0 & 1 & 0 & 0 \\ 0 & 0 & 1 & 0 \\ 0 & 0 & 0 & 1 \end{pmatrix} , \quad (2.4)$$

while the distance between two events in a generic reference frame is computed as:

$$ds^2 = g_{\mu\nu} dx^\mu dx^\nu , \quad (2.5)$$

and  $g_{\mu\nu}$  is called the *metric tensor*. The concepts of geometry and metric are fundamental in GR and gravity indeed represents the effect of the curvature of space-time in the presence of massive bodies. This statement is encoded in *Einstein's equation*:

$$G^{\mu\nu} = \frac{8\pi G}{c^4} T^{\mu\nu} . \quad (2.6)$$

In the equations above  $G^{\mu\nu}$  is the *Einstein tensor* and contains the information on the geometry of the space-time, while  $T^{\mu\nu}$  is called the *stress-energy tensor* and describes the energy density and flux of generic matter fields. Its components are defined as following:  $T^{00}$  is the energy density,  $T^{0i}$  is the energy which flows per unit time across a unit surface orthogonal to the axis  $x^i$ , and  $T^{ij}$  is the amount of the  $i$ -th component of momentum which flows per unit time across the unit surface orthogonal to the axis  $x^j$ . Note that the stress-energy always satisfies the so-called GR expression of the *energy and momentum conservation law*:

$$T^{\mu\nu}_{;\nu} = 0 , \quad (2.7)$$

where the punctuation symbol ";" denotes the *covariant derivative* operator. When applied to a generic  $(^2_0)$  tensor this operator gives

$$A^{\mu\nu}_{;\beta} = (\nabla A^{\mu\nu})_\beta = A^{\mu\nu}_{,\beta} + A^{\alpha\nu}\Gamma_{\alpha\beta}^\mu + A^{\alpha\mu}\Gamma_{\alpha\beta}^\nu , \quad (2.8)$$

where "," denotes the standard derivative operator with respect to the chosen coordinates, while  $\Gamma_{\mu\nu}^\alpha$  are called the *Christoffel symbols* and are defined as:

$$\Gamma_{\mu\nu}^\alpha = \frac{1}{2} g^{\alpha\lambda} (g_{\mu\lambda,\nu} + g_{\lambda\nu,\mu} - g_{\mu\nu,\lambda}) . \quad (2.9)$$

The objects and the definitions just mentioned will come in hand shortly as our goal now will be to define the equations of stellar structure for NSs in GR.

### 2.2.2 Stellar equations

Let us assume the NS to be made of a perfect fluid, i.e. a non-viscous fluid in which heat flux is absent, having a fixed chemical composition and in thermodynamical equilibrium. We can describe the macroscopic motion of the fluid in terms of its *four-velocity*  $u^\alpha(x)$  which is tangent to the worldlines of the small fluid elements. The latter are considered to have a 3-volume which is much larger than the scale of the typical microphysical interactions but small with respect to the macroscopic length-scale of the system.

Let us also define a convenient reference frame which is locally inertial, i.e. a LIF, and instantaneously comoving with a fluid element: the *locally comoving inertial frame (LICF)*. Since the fluid is in thermodynamical equilibrium, we can define the following thermodynamical quantities measured in the LICF:

- $n$ , the baryon number density;
- $\epsilon$ , the mass-energy density;
- $p$ , the pressure;
- $T$ , the temperature;
- $s$ , the entropy per baryon.

Next, let us write the stress-energy tensor in this reference frame:

$$T^{\mu\nu} = \begin{pmatrix} \epsilon & 0 & 0 & 0 \\ 0 & p & 0 & 0 \\ 0 & 0 & p & 0 \\ 0 & 0 & 0 & p \end{pmatrix}. \quad (2.10)$$

The components  $T^{0i}$  vanish because there is no energy exchange between the fluid element and its surroundings (no heat flow), while the absence of viscosity puts to zero the components  $T^{ij}$  with  $i \neq j$  (no tangential stresses). Since in the LICF a fluid element has four-velocity  $u^\mu = (1, 0, 0, 0)$  and  $g_{\mu\nu} = \eta_{\mu\nu}$ ,  $T^{\mu\nu}$  can be written as:

$$T^{\mu\nu} = (\epsilon + p)u^\mu u^\nu + p\eta^{\mu\nu}, \quad (2.11)$$

which is a tensorial definition and thus it is covariant for all reference frames. Exploiting Eqns. (2.6) and the expression obtained for  $T^{\mu\nu}$ , we can now derive the equations governing a non-rotating spherically symmetric star in static equilibrium. Note that, in the following, we will use geometric units, i.e.  $G = c = 1$ .

For a star with these characteristics the metric is given by:

$$ds^2 = g_{\mu\nu}dx^\mu dx^\nu = -e^{\nu(r)}dt^2 + e^{\lambda(r)}dr^2 + r^2(d\theta^2 + \sin^2\theta d\phi^2), \quad (2.12)$$

where we have used the spherical coordinates  $(t, r, \theta, \phi)$  and  $\nu(r), \lambda(r)$  are generic functions of the radial coordinate. Let us also note that the Einstein tensor  $G_{\mu\nu}$  in Eqns. (2.6) is defined as:

$$G_{\mu\nu} = \left( R_{\mu\nu} - \frac{1}{2}g_{\mu\nu}R \right), \quad (2.13)$$

where the *Ricci tensor*,  $R_{\mu\nu}$ , and *Ricci scalar*,  $R$ , ultimately depend on the metric and its second derivatives. Moreover, exploiting the covariancy of Eqns. (2.11), we can obtain the expression of  $T^{\mu\nu}$  in these coordinate system:

$$T^{\mu\nu} = (\epsilon + p)u^\mu u^\nu + p\eta^{\mu\nu}, \quad (2.14)$$

where  $g_{\mu\nu}$  is the metric defined in (2.12). Note that from the normalization of the four-velocity vector we can derive the expression of the four-velocity in the LICF:

$$g_{\mu\nu}u^\mu u^\nu = -1 \rightarrow g_{00}(u^0)^2 = -1 \rightarrow u^0 = e^{-\nu(r)} , \quad (2.15)$$

thus, in this metric,  $u^\alpha = (e^{-\nu(r)}, 0, 0, 0)$ .

Other than exploiting Einstein's equation, the calculations of the stellar equations are simplified significantly using the GR equation of the energy and momentum conservation law in Eqns (2.7). The only non trivial component of the latter is the  $\mu = r$  component which gives the differential equation:

$$\nu_{,r} = -\frac{p_{,r}}{\epsilon + p} . \quad (2.16)$$

Next, we compute  $G_{\mu\nu}$  from Eqns. (2.13) remembering that

$$R_{\mu\nu} = \left( \Gamma_{\mu\alpha,\nu}^\alpha - \Gamma_{\mu\nu,\alpha}^\alpha - \Gamma_{\mu\nu}^\alpha \Gamma_{\alpha\beta}^\beta + \Gamma_{\mu\beta}^\alpha \Gamma_{\nu\alpha}^\beta \right) , \quad (2.17)$$

and

$$R = g^{\mu\nu} R_{\mu\nu} , \quad (2.18)$$

also exploiting the definition of the Christoffel symbols in Eqns. (2.9).

Finally, we can write the non-vanishing components of the Einsteins equations:

$$\begin{aligned} G_{00} &= 8\pi T_{00} \rightarrow \frac{1}{r^2} e^{2\nu} \frac{d}{dr} \left[ r(1 - e^{-2\nu}) \right] = 8\pi \epsilon e^{2\nu} \\ G_{rr} &= 8\pi T_{rr} \rightarrow -\frac{1}{r^2} e^{2\lambda} (1 - e^{-2\lambda}) + \frac{2}{r} \nu_{,r} = 8\pi p e^{2\lambda} \\ G_{\theta\theta} &= 8\pi T_{\theta\theta} \rightarrow r^2 e^{-2\lambda} \left[ \nu_{,rr} + \nu_{,r}^2 + \frac{\nu_{,r}}{r} + \nu_{,r} \lambda_{,r} - \frac{\lambda_{,r}}{r} \right] = 8\pi r^2 . \end{aligned} \quad (2.19)$$

Combining Eq. (2.16) and Eqns. (2.19) we obtain the final set of equations:

$$\begin{cases} \frac{dm}{dr} = 4\pi r^2 \epsilon(r) \\ \frac{dp}{dr} = -\frac{[\epsilon(r) + p(r)] \cdot [m(r) + 4\pi r^3 p(r)]}{r[r - 2m(r)]} , \end{cases} \quad (2.20)$$

where  $m(r)$  is defined as:

$$m(r) = \frac{1}{2} r(1 - e^{2\lambda(r)}) . \quad (2.21)$$

The set of equations in (2.20) are known as *Tolman, Oppenheimer and Volkoff (TOV) equations*. They represent the generalization of the Newtonian stellar structure equations:

$$\begin{cases} \frac{dm}{dr} = 4\pi r^2 \rho(r) \\ \frac{dp}{dr} = -\frac{\rho(r)m(r)}{r^2} . \end{cases} \quad (2.22)$$

Thus, the first of the (2.20) represents the generalization of the Newtonian mass continuity equation, with the mass density being replaced by the energy density. The second of Eqns. (2.20) generalizes the equation of hydrostatic equilibrium in a star.

## 2.3 The equation of state

As mentioned in Section 2.1 the EoS is a relation between the thermodynamic properties (temperature, pressure etc.) of a system which ultimately determines its observable properties and depends on the microscopic interactions of nuclear matter.

In the following we will see how the EoS complements the information carried by the TOV equations (Eqns. (2.20)) and we will describe the nuclear model considered as our baseline model throughout the analyses in Chapter 5.

### 2.3.1 Thermodynamics and barotropic EoS

In 2.2.2 we have observed that by assuming the NS to be composed of a (perfect) fluid in thermal equilibrium, we can define a set of macroscopic thermodinamical observables of the star, such as its temperature, pressure and entropy per barion. These properties are related between one another through the *first law of thermodynamics* which in a LICF is formally identical to its Newtonian expression<sup>1</sup>:

$$dE = -pdV + TdS , \quad (2.23)$$

where  $E$  is the total energy,  $V$  is the volume of the star and  $S$  is the total entropy. Calling  $A$  the total number of baryons, we can rewrite these quantities as

$$E = \epsilon V , \quad V = A/n , \quad S = sA , \quad (2.24)$$

and substitute them into Eq. (2.23):

$$d\left(\frac{A}{n}\epsilon\right) = -pd\left(\frac{A}{n}\right) + Td(As) . \quad (2.25)$$

Finally, multiplying everything by  $n/A$  we obtain:

$$d\epsilon = \frac{\epsilon + p}{n} dn + nTds . \quad (2.26)$$

We can now observe that if we choose, for instance, an EoS of the form  $\epsilon(n, s)$  the pressure and temperature can be found from the first law of thermodynamics as:

$$\begin{aligned} \left(\frac{\partial\epsilon}{\partial n}\right)_s &= \frac{\epsilon + p}{n} \rightarrow p(n, s) = n \left(\frac{\partial\epsilon}{\partial n}\right)_s - \epsilon \\ \left(\frac{\partial\epsilon}{\partial s}\right)_n &= nT \rightarrow T(n, s) = \frac{1}{n} \left(\frac{\partial\epsilon}{\partial s}\right)_n . \end{aligned} \quad (2.27)$$

It is, indeed, valid in general for perfect fluids with fixed chemical composition that given the EoS, which can be expressed as the relation between one thermodynamical variable (e.g.  $\epsilon$ ) and two others (e.g.  $s$  and  $n$ ), the remaining variables can be found from the first law of thermodynamics.

An EoS is said to be *barotropic* when it reduces to the relation  $p \equiv p(\epsilon)$  or, equivalently,  $\epsilon = \epsilon(p)$ . From what we have just said we might not expect the NS EoS to be barotropic. However, we will now briefly explain why this still provides a reliable approximation for realistic stars. First, in 2.1 we have mentioned that a NS is mainly sustained by the degenerate pressure of neutrons. Indeed, the degeneracy of

---

<sup>1</sup>This is a consequence of the Strong Equivalence Principle.

neutrons is a consequence of the fact that the NS is "cold" with respect to the *Fermi temperature*  $T_F$  of neutrons. The latter defines a threshold below which quantum effects become non-negligible. As a matter of fact, after  $\sim 1$  year from its birth, the temperature of the NS decreases to  $T \simeq 10^9$ K, far below the Fermi temperature which, at the typical densities of the NS ( $\rho \approx 10^{14}$ g/cm<sup>3</sup>), is around  $T_F \simeq 10^{11}$ K. In this sense, we can consider the temperature of the star to be zero and, thus, rewrite the first law of thermodynamic in Eq. (2.26) as:

$$d\epsilon = \frac{\epsilon + p}{n} dn , \quad (2.28)$$

which combined with the first relation found in Eq. (2.27) allows to rewrite the EoS in a barotropic form.

**Barotropic EoS and integration of the TOV equations.** A barotropic EoS is also very useful because it easily closes the TOV equation system and allows to integrate it. To integrate the system in Eq. (2.20) we need two<sup>2</sup> boundary conditions:  $m(0)$  and  $\epsilon(0)$ . The first boundary condition can be fixed as  $m(0) = 0$ . Indeed, if we take a tiny sphere surrounding the center of the star with radius  $r = x$ , circumference  $2\pi x$  and proper radius

$$\int_0^x e^\lambda dr \sim e^\lambda x , \quad (2.29)$$

the ratio between the circumference and the proper radius is  $2\pi e^{-\lambda}$ . Since by the Strong Equivalence Principle the spacetime is locally flat, the ratio between the circumference of the sphere and its radius must be  $2\pi$ . This implies that  $e^\lambda \rightarrow 1$  as  $r \rightarrow 0$  and since

$$e^{2\lambda} = \frac{1}{1 - \frac{2m}{r}} , \quad (2.30)$$

it ultimately implies that  $m(0) = 0$ . Therefore, for any assigned barotropic EoS, we obtain a one-parameter family of solutions identified by the boundary condition  $\epsilon(0) = \epsilon_c$ , i.e. the value of the energy density at the center of the star. Note that integrating the TOV equations for a certain EoS and  $\epsilon_c$  returns the mass and radius of the respective equilibrium configuration of the NS. Thus, if we continue to integrate the TOV for the same EoS changing the value of the central energy we would eventually come out with one of the curves in the *mass-radius diagram* as in Fig. 2.3.

**Stiffness and softness.** In Fig. 2.3 we can distinguish different types of curves, some steeper which correspond to bigger radii, some softer which correspond to smaller radii. Indeed, an EoS is usually categorized as either a *stiff EoSs* or a *soft EoSs*. An EoS is considered *stiff* when a variation of the mass-energy density causes a large increase in the internal pressure of the star, while *soft* otherwise. For instance, a star with a stiff EoS resists more efficiently to its own self gravity than a soft EoS. This implies that, given a certain mass, stiff EoSs predict a more expanded and less compact equilibrium configuration than a soft one. Therefore, in Fig. 2.3 stiff EoSs are placed on the right hand side, i.e. larger radii, and have higher maximum masses, conversely, the ones less stretched on the left are soft EoSs. Note that these EoSs, rather than in their analytic expression, are commonly provided in *tabulated form*, i.e. an ordered list of  $\{\epsilon, p(\epsilon)\}$  computed using complex nuclear-physics models.

---

<sup>2</sup>The third boundary condition for  $p$  is obtained from the EoS, i.e.  $p(0) = p(\epsilon(0))$ .

We can conclude that the EoS affects the mass and radius of a neutron star, as well as any other stellar macroscopic feature, as its moment of inertia, or its response to external tidal "solicitations". As we will discuss in the following, the latter is encoded in the so called *Love Numbers*, and the related tidal deformability. Masses and deformabilities represent key parameters encoding information on the EoS and, crucially, affect the GW emission of coalescing neutron star binaries. Therefore, from the study of these emissions one can ultimately recover through these parameters the properties of the NS EoS. For this reason they will be the focus of the next Chapters and of the analyses conducted in Chapter 5.

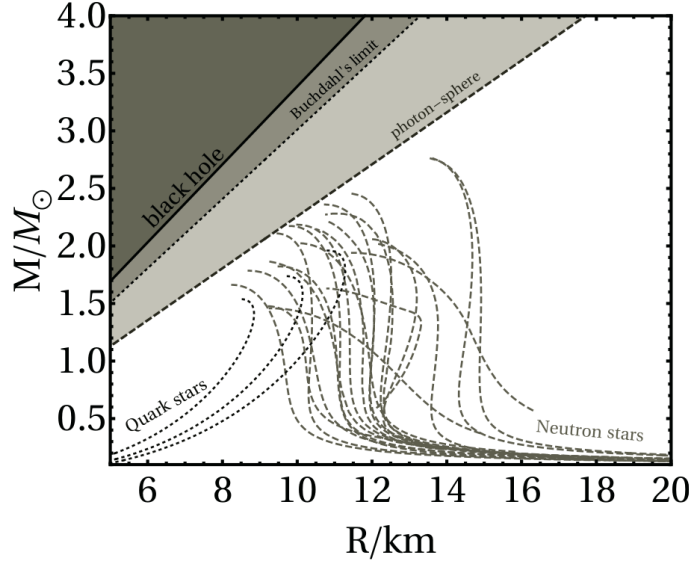


**Figure 2.3.** Mass-radius diagram of non-spinning neutron stars for several EoSs. Note that the dotted curves starting in the bottom-left part of the diagram correspond to quark stars, while ordinary neutron star are displayed as the dashed curves on the bottom-right part of the diagram (Ferrari et al., 2020).

### 2.3.2 Non-relativistic many body nuclear model

As we have already mentioned, the EoS of a NS and its observable properties ultimately depend on the model we choose to describe nuclear interactions. Therefore, to continue with our analyses of NSs and their emission we first need to fix the baseline model which will consider throughout the next Chapters.

In particular, we will describe nucleons dynamics through the non-relativistic Hamiltonian (Tonetto et al., 2021):

$$H = \sum_i \frac{p_i^2}{2m} + \sum_{i < j} v_{ij} + \sum_{i < j < k} V_{ijk}, \quad (2.31)$$

where  $m, \vec{p}$  are, respectively, the nucleon mass and momentum. The framework defined above falls within the so-called *Nuclear Many-Body Theory* (NMBT) approaches, in which nuclear systems are described in terms of point-like nucleons interacting through two- and three-body forces, thus the nucleon-nucleon (NN) potential  $v_{ij}$  and the nucleon-nucleon-nucleon (NNN) potential  $V_{ijk}$  in Eq. (2.31). The NNN potential contribution becomes particularly significant in the regions of highest density in the NS. This term is commonly described as the sum of two potentials

(see Eq. (2.32)): the attractive Fujita-Miyazawa potential ( $V_{ijk}^{2\pi}$ ), describing the two-pion exchange process in which a NN interaction leads to the excitation of a  $\Delta$  resonance (Fig. 2.4), and a purely phenomenological repulsive potential ( $V_{ijk}^R$ ),

$$V_{ijk} = V_{ijk}^{2\pi} + V_{ijk}^R . \quad (2.32)$$

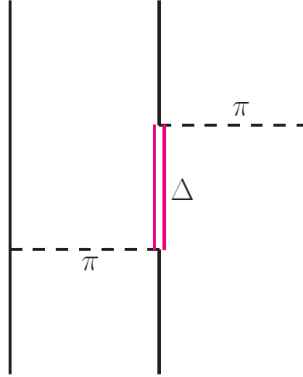


**Figure 2.4.** Diagrammatic representation of the NNN interaction described by the Fujita-Miyazawa potential. Dashed lines represent the pion-exchange, while the solid lines and the double line represent nucleons and the  $\Delta$  resonance, respectively (Tonetto et al., 2021).

The amplitude of  $V_{ijk}^R$  is strongly related to the stiffness of the EoS but it is almost unconstrained above nuclear saturation density. Thus, to investigate different scenarios we will modify the Hamiltonian in Eq. (2.31) introducing a free-parameter which defines the strength of 3-nucleon repulsive interactions called  $\alpha$  (Sabatucci et al., 2022). This is done through the transformation:

$$V_{ijk}^R \rightarrow \alpha V_{ijk}^R . \quad (2.33)$$

In the top panel of Fig. 2.5 we show the mass-radius relation for different values of  $\alpha$  in the range  $0.7 \leq \alpha \leq 2$  (Sabatucci et al., 2022). As we can observe, larger values of  $\alpha$ , i.e. stronger repulsive three-nucleon forces, yield stiffer EoSs. The bottom panel of Figure 2.5 also displays the normalized<sup>3</sup> tidal deformability  $\lambda/M^5$  as a function of the NS mass  $M$ , for different values of  $\alpha$ . As discussed before, the NS deformability, which we will properly introduce in Section 2.4, determines the resistance of the NS to an external tidal field. For a fixed mass, the larger  $\alpha$ , the stiffer the EoS, and the more diluted in space the equilibrium configuration predicted by the TOV equations, i.e. the bigger the dimensionless tidal deformability.

<sup>3</sup>Note that in geometric units such quantity is dimensionless.

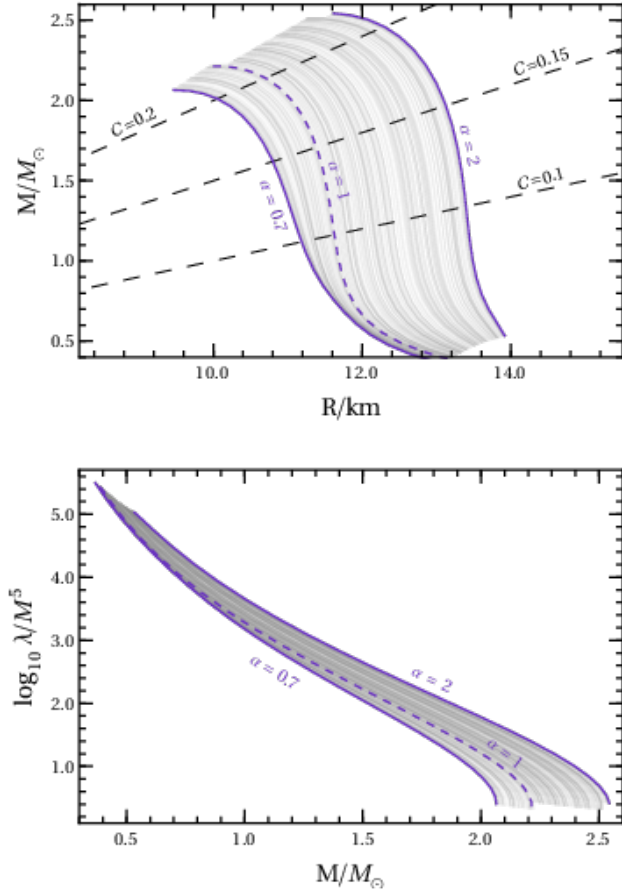


**Figure 2.5.** Top panel: mass-radius profiles for different values of the parameter  $\alpha$ . Bottom panel: profile of the dimensionless tidal deformability in terms of the NS mass. Each gray line corresponds to a value of  $\alpha \in [0.7, 2]$  while the dashed purple line corresponds to  $\alpha = 1$  (Sabatucci et al., 2022).

## 2.4 Love numbers

In this Section we will derive the expression of the NS Love Numbers both in a Newtonian framework and in a Relativistic framework. These quantities represent the key parameters to access the information on the EoS carried by the gravitational wave and electromagnetic emission of coalescing neutron stars binaries which will be introduced in Chapter 3 and will represent our main focus for the rest of the work.

### 2.4.1 Love Numbers in a Newtonian framework

We will follow the *perturbative* approach developed in Poisson & Will (2014), firstly defining the equations of a self-gravitating spherical fluid and then perturbing these equations with the introduction of an external potential (*tidal field*).

**Fluid equations.** Let us consider a body  $A$  which we will assume to be made of a perfect fluid and to belong to a system of  $N$  interacting bodies<sup>4</sup>. A perfect fluid's essential properties (its density  $\rho(\vec{x}, t)$ , pressure  $p(\vec{x}, t)$  and velocity field  $\vec{v}(\vec{x}, t)$ ) are governed by the *continuity equation*:

$$\frac{\partial \rho}{\partial t} + \nabla \rho \cdot v = 0 , \quad (2.34)$$

and the *Euler equation*:

$$\rho \frac{d\vec{v}}{dt} = \rho \nabla U - \nabla p , \quad (2.35)$$

where  $U(t, \vec{x})$  is the gravitational potential (per mass unit) produced by all the bodies in the system which satisfies the *Poisson equation*:

$$\nabla^2 U = -4\pi G \rho . \quad (2.36)$$

The general solution to the Poisson equation has the expression:

$$U(t, \vec{x}) = G \int d^3 x' \frac{\rho(t, \vec{x}')}{|\vec{x} - \vec{x}'|} . \quad (2.37)$$

We will express this potential as the sum of two contributions: the *internal potential* produced by body  $A$  ( $U_A$ ) and the *external potential* produced by the remaining bodies ( $U_{-A}$ ). Inserting  $U = U_A + U_{-A}$  and putting ourselves in the reference frame of  $A$ 's center of mass, Eq. (2.35) becomes:

$$\rho \frac{d\vec{v}}{dt} = \rho \nabla U_A - \nabla p + \rho \nabla (U_{-A} - \vec{a}_A \cdot \vec{x}) , \quad (2.38)$$

where,  $\vec{r}_A \equiv \vec{0}$  represents the position of  $A$ 's center of mass,  $\vec{x} = \vec{x} - \vec{r}_A$  denotes the position relative to  $A$ 's center of mass,  $\vec{v} = \frac{d\vec{x}}{dt}$  is the relative velocity field and  $\vec{a}_A$  is the center of mass' acceleration. For simplicity the gradient in this new coordinate system will still be denoted with the symbol  $\nabla$ . Note that the first two terms on the right in Eq. (2.38) account for internal aspects of the body's dynamics while the last term on the left accounts for the influence of the external bodies. Moreover, the term  $\nabla(U_{-A} - \vec{a}_A \cdot \vec{x})$  in Eq. (2.38) can be interpreted as the gradient of an effective external potential  $U_{eff}$  defined as:

$$U_{eff} = U_{-A} - \vec{a}_A \cdot \vec{x} , \quad (2.39)$$

where  $-\nabla(\vec{a}_A \cdot \vec{x})$  represents the fictitious force that arises because of the non-inertial motion of the center of mass.

Since the internal potential satisfies Poisson equation, it can be expressed, as in Eq. (2.37), as:

$$U_A(t, \vec{x}) = G \int_A d^3 x' \frac{\rho(t, \vec{x}')}{|\vec{x} - \vec{x}'|} , \quad (2.40)$$

---

<sup>4</sup>Further on we will restrict ourselves to a binary systems of compact objects ( $N=2$ ).

while we will define the external potential in terms of its Taylor expansion around A's center of mass:

$$\begin{aligned}
U_{-A}(t, \vec{x}) &= \sum_{\ell=0}^{\infty} \frac{1}{\ell!} (\partial_{j_1} \partial_{j_2} \dots \partial_{j_\ell} U_{-A}) \bar{x}^{j_1} \bar{x}^{j_2} \dots \bar{x}^{j_\ell} \\
&= \sum_{\ell=0}^{\infty} \frac{1}{\ell!} (\partial_{j_1, j_2, \dots, j_\ell} U_{-A}) \bar{x}^{j_1, j_2, \dots, j_\ell} \\
&= \sum_{\ell=0}^{\infty} \frac{1}{\ell!} (\partial_L U_{-A}) \bar{x}^L \\
&= U_{-A}(t, \vec{0}) + g_j(t) \bar{x}^j - \sum_{\ell=2}^{\infty} \frac{1}{\ell!} \mathcal{E}_L(t) \bar{x}^L.
\end{aligned} \tag{2.41}$$

In Eq. (2.41) we have used the condensed notation presented in Poisson & Will (2014). The uppercase index  $L$  represents a collection of  $\ell$  indices, i.e.  $\bar{x}_L = \bar{x}_{j_1, j_2, j_3, \dots, j_\ell}$  and  $\partial_L = \partial_{j_1, j_2, j_3, \dots, j_\ell}$ . Moreover, the notation  $\bar{x}_{j_1, j_2, j_3, \dots, j_\ell}$  and  $\partial_{j_1, j_2, j_3, \dots, j_\ell}$  translates into the products  $\bar{x}_{j_1} \cdot \bar{x}_{j_2} \cdot \dots \cdot \bar{x}_{j_\ell}$  and  $\partial_{j_1} \cdot \partial_{j_2} \cdot \dots \cdot \partial_{j_\ell}$ . Note that the indices  $j_1, j_2, \dots, j_\ell$  can only vary between 1 and 3 (they correspond to the three spatial directions). In the last line of Eq. (2.41) we have broken down the expansion of  $U_{-A}$  into three terms:

- **term  $\ell = 0$ :** This corresponds to the constant term  $U_{-A}(t, \vec{0})$  which is not of much interest for our analysis since it vanishes in Eq. (2.35) and thus will be ignored from this point on;
- **term  $\ell = 1$ :** This corresponds to  $g_j(t) x^j$  where we have introduced the quantity  $g_j(t) = \partial_j U_{-A}(\vec{0}, t)$ ;
- **terms  $\ell \geq 2$ :** These are the terms appearing in the sum on the right, where we have defined  $\mathcal{E}_L(t) = -\partial_L U_{-A}(\vec{0}, t)$ .

The tensors  $\mathcal{E}_L(t)$  are the so-called *tidal multipoles*. Note that, since  $U_{-A}$  satisfies the Laplace equation within the volume occupied by  $A$  (i.e.  $\nabla^2 U_{-A} = 0$ ),  $\mathcal{E}_L$  are not only symmetric but also trace-free, i.e. they are symmetric trace-free tensors or *STF tensors*.

Our goal now is to exploit the final relation in Eq.(2.41) to re-express the potential  $U_{\text{eff}}$  in Eq. (2.39) but we first need to find an expression for  $\vec{a}_A$ . Exploiting the definition of the center of mass's acceleration  $\vec{a}_A$  in an arbitrary reference frame we can rewrite:

$$\begin{aligned}
\vec{a}_A(t) &= \frac{1}{M_A} \int_A \rho(\vec{x}, t) \frac{d\vec{v}}{dt} d^3\vec{x} \\
&= \frac{1}{M_A} \int_A \rho(\vec{x}, t) \nabla U_A d^3\vec{x} + \frac{1}{M_A} \int_A \rho(\vec{x}, t) \nabla U_{-A} d^3\vec{x} \\
&= \frac{1}{M_A} \int_A \rho(\vec{x}, t) \nabla U_{-A},
\end{aligned} \tag{2.42}$$

where we substituted Eq. (2.35) and split  $U$  into the internal and external contribution. Note that the integral  $\int_A \rho(\vec{x}, t) \nabla U_A d^3\vec{x} = 0$  because of the conservation of the total momentum of body  $A$ . Next, inserting the final relation presented in Eq.

(2.41), we obtain:

$$\begin{aligned} a_A^j &= \frac{1}{M_A} \sum_{\ell=0}^{\infty} \frac{1}{\ell!} I_A^{(L)}(t) \partial_{jL} U_{-A}(\vec{0}, t) \\ &= g^j - \frac{1}{M_A} \sum_{\ell=2}^{\infty} \frac{1}{\ell!} I_A^{(L)}(t) \mathcal{E}_{jL}(t), \end{aligned} \quad (2.43)$$

where  $g^j$  corresponds to the term  $\ell = 0$  in the sum, while the term for  $\ell = 1$  vanishes because the integral  $M_A^{-1} \int_A \rho x^j = r_A^j$  is zero in the center of mass reference frame. The tensors  $I_A^{(L)}$  are the *multipole moments* of body  $A$ :

$$I_A^{(L)}(t) = \int_A \rho(\vec{x}, t) (\vec{x} - \vec{r}_A)^{(L)} d\vec{x}^3. \quad (2.44)$$

Note that the angular brackets are used to denote that  $I_A^{(L)}$  are indeed STF tensors. Substituting the last line of Eq. (2.41) and Eq. (2.43) into Eq. (2.39) we get:

$$U_{\text{eff}} = - \sum_{\ell=2}^{\infty} \frac{1}{\ell!} \left[ \mathcal{E}_L \bar{x}^L - \frac{I_A^{(L)}(t)}{M_A} \mathcal{E}_{jL} \bar{x}^j \right]. \quad (2.45)$$

Finally, exploiting the fact that for almost spherical bodies the coupling terms between the body multipoles,  $I_A^L$ , and the tidal multipoles,  $\mathcal{E}_L$ , can be neglected, the effective potential can be rewritten as:

$$U_{\text{eff}} = - \sum_{\ell=2}^{\infty} \frac{1}{\ell!} \mathcal{E}_L \bar{x}^L. \quad (2.46)$$

This is the expression for the external potential we will be using in the following paragraphs to obtain the Love Numbers' classic formula. Note that the effect of the external effective potential in Eq. (2.46) has a subdominant contribution on the fluid dynamics, i.e. to Eq. (2.38), compared to the internal potential  $U_A$ . This can be checked, for instance, in the case of a binary system composed of body  $A$  and its companion  $B$ . While the internal potential scales as  $U_A \sim GM_A/\bar{r}_C$ , being  $\bar{r}_C$  a characteristic length scale within the body, the external potential is dominated by the term  $\ell = 2$  and scales as  $U_B \sim GM_B \bar{r}_C^2/r_{AB}^3$ , being  $r_{AB}$  the typical inter-body distance. From these relations we can obtain the typical scale of the ratio between the two potentials' intensities:

$$\frac{U_B}{U_A} \sim \frac{M_B}{M_A} \left( \frac{\bar{r}_C}{r_{AB}} \right)^3. \quad (2.47)$$

As we would intuitively expect, the perturbative influence of the external potential is negligible when the two bodies are well separated ( $\bar{r}_C \ll r_{AB}$ ) but becomes relevant as the inter-body distance becomes comparable to body  $A$ 's typical length scale. In the case of a binary coalescence, then, tidal effects are increasingly relevant as the two bodies approach each other.

It is important to note that although  $\mathcal{E}_L$  and  $I^L$  are in general time-dependent, for our future calculations we limit ourselves to the case of two bodies sufficiently distant that the tidal fields change slowly with respect to their orbital period. Under this assumption of *static tides* the tensors  $\mathcal{E}_L$  and  $I^L$  can be considered approximately constant and the external tidal field is assumed to be too slow to take the stars out of hydrostatic equilibrium. Let us now move on to the computation of the Love Numbers following the perturbative approach of Poisson & Will (2014).

**Unperturbed configuration.** We will first consider body  $A$ 's unperturbed configuration to be spherically-symmetric, non-rotating<sup>5</sup> and in hydrostatic equilibrium. For a spherically symmetric body Poisson equation (Eq. (2.36)) can be rewritten as:

$$\frac{1}{r^2} \frac{d}{dr} \left( r^2 \frac{dU}{dr} \right) = -4\pi G\rho(r) , \quad (2.48)$$

which also leads to the relation:

$$\frac{dU}{dr} = -\frac{Gm(r)}{r^2} , \quad (2.49)$$

where  $m$  is the mass contained in a sphere of radius  $r$  and is related to the density function  $\rho$  by the mass continuity equation:

$$\frac{dm}{dr} = 4\pi\rho(r)r^2 . \quad (2.50)$$

The equilibrium version of Euler equation for body  $A$  in the center of mass reference frame can be derived from Eq. (2.38) by neglecting the external terms and fixing  $\bar{v}^j = 0$ . This leads to the equation of hydrostatic equilibrium of the star:

$$\frac{dp}{dr} = \rho(r) \frac{dU}{dr} = -\frac{G\rho(r)m(r)}{r^2} , \quad (2.51)$$

where here we have exploited Eq. (2.49) found above. Similarly to what we have seen in 2.3.1, to complete the system composed of the mass continuity equation and the hydrostatic equilibrium equation we must specify the EoS of the NS. For our analysis we will assume the EoS to be *polytropic* which means that the pressure only depends on the density as:

$$p = K\rho^\Gamma , \quad (2.52)$$

where  $K$  and  $\Gamma = 1 + 1/n$  are constants and  $n$  is the *polytropic index*. This EoS well represents the behaviour of white dwarfs (i.e. stars sustained by the degenerate pressure of electrons) but is less accurate to depict the behaviour of matter inside neutron stars, although a generalization to this EoS is found for *piecewise polytropes* model (Read et al., 2009).

**Perturbed configuration.** We are now going to consider the linear perturbations to the fluid equations of body  $A$  caused by the influence of the external potential of a body  $B$  (Eq. (2.46)). From this point on  $U_{\text{eff}}$  will be denoted as  $U_{\text{tidal}}$ , the *tidal potential* produced by body  $B$ .

Note that the perturbation of any generic fluid quantity  $Q$  can be described either following a *Eulerian approach* or a *Lagrangian approach*. The former employs a *macroscopic* point of view:  $Q$  is compared to its unperturbed value  $Q_0$  at the same point in space and the perturbation is computed as

$$\delta Q := Q(t, \vec{x}) - Q_0(t, \vec{x}) . \quad (2.53)$$

While, the latter employs a *microscopic* point of view:  $Q$  is compared at the same fluid element, displaced by the vector  $\vec{\xi}(t, \vec{x})$  relative to its unperturbed position  $\vec{x}$ , and the perturbation on  $Q$  is computed as

$$\Delta Q := Q(t, \vec{x} + \vec{\xi}(t, \vec{x})) - Q_0(t, \vec{x}) \simeq \delta Q + \xi^i \partial_i Q_0 . \quad (2.54)$$

---

<sup>5</sup>The hypothesis of non-rotation is just a simplifying assumption (see Poisson & Will (2014) for the complete analysis of the body's rotation).

The commutation rules between these two kinds of perturbations and the operators appearing in Euler equation (Eq. 2.35) are:

$$\begin{aligned} [\delta, \partial_t] &= 0 ; \\ [\delta, \partial_i] &= 0 ; \\ [\Delta, \partial_t] &= -(\partial_t \xi^k) \partial_k ; \\ [\Delta, \partial_i] &= -(\partial_i \xi^k) \partial_k ; \\ \left[ \Delta, \frac{d}{dt} \right] &= 0 . \end{aligned} \quad (2.55)$$

**Perturbed continuity equation.** The mass of a portion of fluid remains the same after that portion is perturbed. Assumed the portion of fluid changes its volume from  $V$  to  $\tilde{V} = V + \Delta V$  and its density from  $\rho$  to  $\rho + \delta\rho$  after the perturbation, this implies that the integrals  $\int_V \rho d^3x$  and  $\int_{\tilde{V}} (\rho + \delta\rho) d^3x$  must produce the same number. The integral for the perturbed mass can be rewritten as:

$$\int_{\tilde{V}} \rho d^3x + \int_{\tilde{V}} \delta\rho d^3x = \int_V \rho d^3x + \int_S \rho \vec{\xi} \cdot d\vec{S} + \int_{\tilde{V}} \delta\rho d^3x , \quad (2.56)$$

where we have expressed  $\int_{\tilde{V}} \rho d^3x$  in terms of the mass flux exiting the surface  $S$  which encloses completely  $V$ . The vector  $d\vec{S}$  is the outward-directed surface element. This surface integral can be expressed as a volume integral through the divergence theorem, which leads the mass conservation statement to take the form:

$$\int_V \partial_i(\rho \xi^i) d^3x + \int_{\tilde{V}} \delta\rho d^3x = 0 \rightarrow \int_V [\partial_i(\rho \xi^i) + \delta\rho] d^3x = 0 , \quad (2.57)$$

where on the right side of Eq. (2.57) we are taking into account only the linear perturbative terms. Since Eq. (2.57) is valid for any volume  $V$ , then  $\delta\rho$  must have the expression:

$$\delta\rho = -\partial_i(\rho \xi^i) . \quad (2.58)$$

From Eq. (2.54) we can get the corresponding lagrangian perturbation:

$$\Delta\rho = -\rho \partial_i \xi^i . \quad (2.59)$$

Equations (2.58) and (2.59) correspond to the time-integrated forms of the perturbed continuity equation.

**Perturbed Euler equation.** To compute the perturbed Euler equation let us first rewrite Eq. (2.35) as:

$$\frac{dv^i}{dt} = \partial_i \Phi - \frac{1}{\rho} \partial_i p . \quad (2.60)$$

Note that  $v^i$  represents the perturbed velocity field and  $\Phi$  represents the perturbed total potential which is given by:

$$\Phi = U + \delta\Phi = U + \delta U + U_{tidal} , \quad (2.61)$$

where  $U$  is the unperturbed internal potential and  $\delta U$  is its Eulerian perturbation. Exploiting the commutation relations in Eq. (2.55) we can compute the Langrangian expression of the perturbed Euler equation:

$$\frac{d^2 \xi^i}{dt^2} = \frac{\Delta\rho}{\rho^2} \partial_i p - \frac{1}{\rho} \partial_i \Delta p + \partial_i \Delta\Phi + (\partial_i \xi^k) \left( \frac{1}{\rho} \partial_k p - \partial_k \Phi \right) . \quad (2.62)$$

Note that we also exploited the relation  $\Delta v^i = d\xi^i/dt$  which directly comes from the displacement vector definition. Since the unperturbed configuration is an equilibrium configuration, the unperturbed velocity field vanishes and, as a consequence, the term multiplying  $\partial_i \xi^k$  also vanishes (see Eq. (2.35)). Moreover, the total time derivative  $d^2 \xi^i / dt^2$  is equivalent to the partial time derivative  $\partial^2 \xi^i / \partial t^2$ . Taking into account these properties, Eq. (2.62) becomes:

$$\frac{\partial^2 \xi^i}{\partial t^2} = \frac{\Delta \rho}{\rho^2} \partial_i p - \frac{1}{\rho} \partial_i \Delta p + \partial_i \Delta \Phi . \quad (2.63)$$

Following the same procedure for the Eulerian variation of Euler equation we get:

$$\frac{\partial^2 \xi^i}{\partial t^2} = \frac{\delta \rho}{\rho^2} \partial_i p - \frac{1}{\rho} \partial_i \delta p + \partial_i \delta \Phi . \quad (2.64)$$

**Pressure and potential perturbations.** The perturbed Euler equation (either Eq. (2.63) or Eq. (2.64)) can be solved once the expressions of  $\Delta p$  ( $\delta p$ ) and  $\Delta U$  ( $\delta U$ ) are specified. Since the EoS is polytropic  $\Delta p$  is directly related to  $\Delta \rho$  as:

$$\frac{\Delta p}{p} = \Gamma \frac{\Delta \rho}{\rho} . \quad (2.65)$$

Exploiting Eq. (2.54) and Eq. (2.59) we can also derive the Eulerian pressure perturbation from the equation above:

$$\delta p = -\Gamma p \partial_i \xi^i - \xi^i \partial_i p . \quad (2.66)$$

Finally, in order to find an expression for the perturbation of  $A$ 's gravitational potential,  $\delta U$ , we can exploit the fact that it still satisfies the Poisson equation (Eq. (2.36)) and get:

$$\nabla^2 \delta U = -4\pi G \delta \rho . \quad (2.67)$$

**Perturbed equilibrium.** If the perturbed configuration of the initial equilibrium configuration is also an hydrostatic equilibrium configuration, then  $\partial \xi^i / \partial t = 0$ . Exploiting this condition, Eq. (2.64) becomes:

$$\frac{\delta \rho}{\rho^2} \partial_i p - \frac{1}{\rho} \partial_i \delta p + \partial_i \delta \Phi = 0 . \quad (2.68)$$

To simplify the perturbed continuity equation we will fix  $\vec{\xi}$  to describe the displacement of a fluid element from a spherical surface  $\rho = \text{constant}$  (unperturbed state) to the deformed surface  $\rho = \text{constant}$  (perturbed state). By doing so, we are assuming the vector field  $\vec{\xi}$  to map surfaces of constant density in the unperturbed configuration to surfaces of the same constant density in the perturbed configuration. This choice implies that  $\Delta \rho = 0$  which in turns means that the displacement vector is solenoidal, i.e.  $\partial_i \xi^i = 0$  (see Eq. (2.59)). The new expression for the Eulerian perturbed continuity equation reads:

$$\delta \rho = -\xi^i \partial_i \rho ; \quad \delta p = -\xi^i \partial_i p . \quad (2.69)$$

where on the right hand side we have also shown the expression for  $\delta p$  which can be easily derived from Eq. (2.66) exploiting the divergence-free condition on  $\vec{\xi}$ . Since

the unperturbed density  $\rho$  and pressure  $p$  only depend on the radial coordinate<sup>6</sup> the only relevant component of the displacement vector in Eq. (2.69) is  $\xi^r$ . We will not solve then for the angular components which will be fixed by the divergence-free condition.

**Clairaut-Radau equations.** To proceed further we shall introduce the decomposition of the perturbation quantities in terms of *spherical harmonics*  $Y_{\ell,m}(\theta, \phi)$  which represent a powerful tool to analyze spherically symmetric differential equations. Spherical harmonics are defined as the solutions to the eigenvalue equation:

$$\left( \frac{1}{\sin \theta} \frac{\partial}{\partial \theta} \sin \theta \frac{\partial}{\partial \theta} + \frac{1}{\sin^2 \theta} \frac{\partial^2}{\partial \phi^2} \right) Y_{\ell m} = -\ell(\ell+1) Y_{\ell m} , \quad (2.70)$$

where  $\ell$  is an integer number defined between 0 and  $\infty$  and  $m$  is an integer number defined between  $-\ell$  and  $\ell$ . Note that the operator applied to  $Y_{\ell m}$  on the left side of Eq. (2.70) is the angular part of the Laplacian operator in spherical coordinates. Since spherical harmonics constitute a complete set of orthonormal functions, any square-integrable function on the surface of a sphere,  $g(\theta, \phi)$ , can be expressed in this basis as:

$$g(\theta, \phi) = \sum_{\ell=0}^{\infty} \sum_{m=-\ell}^{\ell} g_{\ell m} Y_{\ell m}(\theta, \phi) , \quad (2.71)$$

where the coefficients  $g_{\ell m}$  are given by:

$$g_{\ell m} = \int g(\theta, \phi) Y_{\ell m}^*(\theta, \phi) d\Omega . \quad (2.72)$$

Thus, we can decompose the perturbation quantities in spherical harmonics as displayed in Eq. (2.73).

$$\begin{aligned} \xi^r &= \sum_{\ell,m} r f_{\ell m}(r) Y_{\ell m}(\theta, \phi) \\ \delta\rho &= \sum_{\ell,m} \rho_{\ell m}(r) Y_{\ell m}(\theta, \phi) \\ \delta p &= \sum_{\ell,m} p_{\ell m}(r) Y_{\ell m}(\theta, \phi) \\ \delta U &= \sum_{\ell,m} U_{\ell m}(r) Y_{\ell m}(\theta, \phi) \\ U_{tidal} &= \sum_{\ell,m} V_{\ell m}(r) Y_{\ell m}(\theta, \phi) \end{aligned} . \quad (2.73)$$

Note that the coefficients  $f_{\ell m}$  are dimensionless because a factor  $r$  was put in the decomposition of  $\xi^r$ . The perturbation source coincides with the tidal potential  $U_{tidal}$  which was defined in Eq. (2.46). Since only  $\ell \geq 2$  terms appear in its definition, the sums appearing in Eq. (2.73) all begin at  $\ell = 2$ , with  $m$  running from  $-\ell$  to  $\ell$ . Substituting the decompositions for  $\xi^r$ ,  $\delta\rho$  and  $\delta p$  in Eq. (2.69) we obtain

$$\rho_{\ell m} = -r \rho' f_{\ell m} , \quad (2.74)$$

---

<sup>6</sup>This is a consequence of the spherical symmetry of the unperturbed configuration.

and

$$p_{\ell m} = -rp'f_{\ell m} = \frac{\rho Gm}{r}f_{\ell m}, \quad (2.75)$$

where the apex ' stands for the total derivative  $d/dr$ . Note that in Eq. (2.75) we have substituted  $p'$  with Eq. (2.51). To find the expression for  $U_{\ell m}$  we need to substitute the decomposition of  $\delta U$  (Eqns. (2.73)) and Eq. (2.74) into the Poisson equation<sup>7</sup> (Eq. (2.67)) and exploit the fact that the spherical harmonics satisfy the eigenvalue relation in Eq. (2.70). By doing so we obtain that, inside the body, the coefficients  $U_{\ell m}$  must satisfy the differential equation:

$$r^2U''_{\ell m} + 2rU'_{\ell m} - \ell(\ell + 1)U_{\ell m} = -4\pi Gr^2\rho_{\ell m}, \quad (2.76)$$

while outside of the body the coefficients have the expression:

$$U_{\ell m}^{out}(r) = \frac{4\pi G}{2\ell + 1} \frac{I_{\ell m}}{r^{\ell+1}}. \quad (2.77)$$

The coefficients  $I_{\ell m}$  are related to the perturbed body's multipole moments  $I_A^{(L)}$  introduced in Eq. (2.44) and are computed as:

$$I_{\ell m}(t) = \int (\rho + \delta\rho)r^{\ell}Y_{\ell m}^*(\theta, \phi)d^3x, \quad (2.78)$$

where the integral is evaluated over the volume containing the body. On the other hand, the coefficients  $V_{\ell m}$  must satisfy the differential equation:

$$r^2V''_{\ell m} + 2rV'_{\ell m} - \ell(\ell + 1)V_{\ell m} = 0. \quad (2.79)$$

Equation (2.79) is obtained in the same fashion as Eq. (2.76) from the Laplace equation  $\nabla^2 V = 0$  which the tidal potential satisfies inside and outside body  $A$ . The only admissible solution for Eq. (2.79) is:

$$V_{\ell m} = \frac{4\pi}{2\ell + 1}d_{\ell m}r^{\ell}, \quad (2.80)$$

where  $d_{\ell m}$  are called the *moments of the driving potential* and can be computed once the expression for  $U_{tidal}$  is specified.

Now we want to substitute the decompositions of the perturbation quantities and the expressions found for the coefficients appearing in the decompositions into Eq. (2.68). What we get is:

$$p'_{\ell m} = -\frac{Gm}{r^2}\rho_{\ell m} + \rho(U_{\ell m} + V_{\ell m}). \quad (2.81)$$

From Eq. (2.51) we can derive an expression for  $p_{\ell m}$ :

$$p_{\ell m} = \rho(U_{\ell m} + V_{\ell m}), \quad (2.82)$$

which we can differentiate with respect to  $r$  and substitute into Eq. (2.81) obtaining the expression:

$$\frac{Gm}{r^2}\rho_{\ell m} = -\rho'(U_{\ell m} + V_{\ell m}). \quad (2.83)$$

---

<sup>7</sup>Note that here we are thinking of expressing the Laplacian operator in spherical coordinates, i.e.  $\nabla^2 = r^{-2}\partial_r(r^2\partial_r) + r^{-2}[(\sin\theta)^{-1}\partial_\theta \sin\theta\partial_\theta + (\sin\theta)^{-2}\partial_{\phi\phi}]$ .

Finally, substituting Eq. (2.74) and (2.75) into Eq. (2.83) we get:

$$\frac{Gm}{r} f_{\ell m} = U_{\ell m} + V_{\ell m} \quad (2.84)$$

which summarizes the content of Euler's equation for a perturbed equilibrium.

As we have proved, the coefficients  $f_{\ell m}$  represent the real key quantities to compute the other perturbation coefficients  $\rho_{\ell m}$  (Eq. (2.74)),  $p_{\ell m}$  (Eq. (2.75)) and  $U_{\ell m}$  (Eq. (2.84)). Thus, we also expect these coefficients to determine the characteristics of the body's deformation induced by  $U_{tidal}$ . Our main goal, now, will be to compute these coefficients.

**Computing the tidal Love Numbers.** Let us insert the expression for  $U_{\ell m}$  which can be obtained from Eq. (2.84) into Eq. (2.76), taking into account Eq. (2.79) (all of the terms concerning  $V_{\ell m}$  represent a null contribution to the differential equation) and Eq. (2.50). The resulting differential equation, called the *Clairaut's equation*, will be:

$$r^2 f''_{\ell m} + 6\mathcal{D}(rf'_{\ell m} + f_{\ell m}) - \ell(\ell+1)f_{\ell m} = 0 , \quad (2.85)$$

where:

$$\mathcal{D} = \frac{4\pi\rho(r)r^3}{3m(r)} = \frac{\rho(r)}{\bar{\rho}(r)} , \quad (2.86)$$

is a function encoding relevant information on the body's unperturbed configuration. More specifically,  $\mathcal{D}$  is the ratio between the mass density at distance  $r$  from the body's center of mass,  $\rho(r)$ , and the mean mass density of the sphere contained within  $r$ ,  $\bar{\rho}(r) = m(r)/(4\pi/3 \cdot r^3)$ .

We will see briefly that Clairaut's equation can be re-expressed in a more convenient way in order to derive the expression of the  $f_{\ell m}$  and the Love Numbers. Let us see how the deformed body's multipole moments  $I_{\ell m}$  can be linked to the driving potential moments  $d_{\ell m}$  through the coefficients  $f_{\ell m}$ . First, we will evaluate Eq. (2.84) on the body's surface ( $r = R$ ) and then substitute the expressions for  $U_{\ell m}$  and  $V_{\ell m}$  outside the body which were presented in Eq. (2.77) and (2.80). This leads to the equation

$$\frac{GM}{R} f_{\ell m}(R) = \frac{4\pi}{2\ell+1} \left[ \frac{GI_{\ell m}}{R^{\ell+1}} + d_{\ell m} R^\ell \right] . \quad (2.87)$$

Repeating this procedure for the first derivative of Eq. (2.84) we obtain that

$$\frac{GM}{R} [Rf'_{\ell m}(R) - f_{\ell m}(R)] = \frac{4\pi}{2\ell+1} \left[ -(\ell+1) \frac{GI_{\ell m}}{R^{\ell+1}} + d_{\ell m} \ell R^\ell \right] . \quad (2.88)$$

Finally solving these equations for  $d_{\ell m}$  and  $I_{\ell m}$  we obtain:

$$d_{\ell m} = \frac{GM}{4\pi R^{\ell+1}} [Rf'_{\ell m}(R) + \ell f_{\ell m}(R)] , \quad (2.89)$$

and

$$GI_{\ell m} = -\frac{GM}{4\pi} R^\ell [Rf'_{\ell m}(R) - (\ell+1)f_{\ell m}(R)] . \quad (2.90)$$

Now, we want to recast these relations and Eq. (2.85) in a simpler form introducing the function:

$$\eta_\ell = \frac{rf'_{\ell m}}{f_{\ell m}} , \quad (2.91)$$

which is known as *Radau's function*. Note that  $\eta_\ell$  does not depend on  $m$ . This results from the fact that the differential equation in Eq. (2.85), although being parametrized in  $m$ , does not explicitly depend on it. This means that  $f_{\ell m}$  must depend on  $m$  through a multiplicative factor which disappears in the ratio  $f'_{\ell m}/f_{\ell m}$  in Eq. (2.91). Substituting Eq. (2.91) into Eq. (2.85) we get the so-called *Radau's equation*:

$$r\eta'_\ell + \eta_\ell(\eta_\ell - 1) + 6\mathcal{D}(\eta_\ell + 1) - \ell(\ell + 1) = 0 . \quad (2.92)$$

This differential equation can be solved numerically integrating it outward from  $r = 0$  with the initial condition  $\eta_\ell(r = 0) = \ell - 2$ . The latter results from substituting the limit<sup>8</sup>  $\mathcal{D} \rightarrow 1$  into Eq. (2.92) for  $r = 0$ . The solution for  $\eta_\ell$  can be exploited to compute  $d_{\ell m}$  and  $I_{\ell m}$  using Eq. (2.90) and (2.89). Moreover, after having re-expressed these two equations in terms of  $\eta_\ell$ , we can get a very useful relation:

$$GI_{\ell m} = 2k_\ell R^{2\ell+1}d_{\ell m} , \quad (2.93)$$

where  $k_\ell$  are the *gravitational Love numbers* which are defined as

$$k_\ell := \frac{\ell + 1 - \eta_\ell(R)}{2[\ell + \eta_\ell(R)]} . \quad (2.94)$$

In the end, we have found that the gravitational "polarization" of the body, represented by  $I_{\ell m}$ , is proportional to the external potential, represented by  $d_{\ell m}$ , through the Love Numbers  $k_\ell$  which encode the response of the body to the gravitational perturbation of its initial equilibrium configuration.

**Perturbed potential of a binary system.** Finally, we want to obtain the full expression for the total gravitational potential in the binary system composed by body  $A$  and body  $B$ . Note that we are still putting ourselves in the reference frame of  $A$ 's center of mass.

Let us start by recalling that  $U_{tidal}$  can be expressed as in Eq. (2.46) in terms of the tensors  $\mathcal{E}_L$ . Since the  $\mathcal{E}_L$  are STF tensors, we can rewrite:

$$\mathcal{E}_{\langle L \rangle} x^L = \mathcal{E}_{j_1, j_2, \dots, j_\ell} x^{j_1} \cdot x^{j_2} \cdots x^{j_\ell} = \sum_{m=-\ell}^{\ell} \mathcal{E}_{\ell m} r^\ell Y_{\ell m}(\theta, \phi) , \quad (2.95)$$

or, equivalently:

$$\mathcal{E}_{j_1, j_2, \dots, j_\ell} n^{j_1} \cdot n^{j_2} \cdots n^{j_\ell} = \sum_{m=-\ell}^{\ell} \mathcal{E}_{\ell m} Y_{\ell m}(\theta, \phi) , \quad (2.96)$$

where,  $\hat{\mathbf{n}} = (\sin \theta \cos \phi, \sin \theta \sin \phi, \cos \theta)$  is the unitary positional vector. A proof of Eq. (2.96) is given in Box 1.6 of Poisson & Will (2014) where the authors prove that the generic scalar field  $A_{\langle L \rangle} n^L$ , where  $A_{\langle L \rangle}$  is a STF tensor, is solution to the same eigenvalue equation which defines the spherical harmonics  $Y_{\ell m}$  (Eq. (2.70)). Since then  $\mathcal{E}_{\langle L \rangle} n^L$  satisfies Eq. (2.70) and the spherical harmonics form a complete basis, we can rewrite the former as in Eq. (2.96).

Substituting Eq. (2.95) into Eq. (2.46) we get

$$U_{tidal} = - \sum_{\ell=2}^{\infty} \sum_{m=-\ell}^{\ell} \frac{1}{\ell!} \mathcal{E}_{\ell m} r^\ell Y_{\ell m}(\theta, \phi) . \quad (2.97)$$

---

<sup>8</sup>This comes from the fact that  $\rho \rightarrow \bar{\rho}$  for  $r \rightarrow 0$ .

Comparing the equation above with the decomposition for  $U_{tidal}$  in Eq. (2.73), we find that  $V_{\ell m} = \mathcal{E}_{\ell m} r^\ell / \ell!$ . Next, we exploit the expression for the coefficients  $V_{\ell m}$  in Eq. (2.80) to obtain a relation between  $\mathcal{E}_{\ell m}$  and  $d_{\ell m}$ :

$$d_{\ell m} = -\frac{2\ell + 1}{4\pi\ell!} \mathcal{E}_{\ell m} . \quad (2.98)$$

Lastly, inserting Eq. (2.98) into Eq. (2.93) we find that

$$GI_{\ell m} = -\frac{2\ell + 1}{2\pi\ell!} k_\ell R^{2\ell+1} \mathcal{E}_{\ell m} , \quad (2.99)$$

which will come in handy further on. Moving on to the gravitational potential produced by body  $A$ , we know that the potential after the tidal perturbation is given by  $U + \delta U$ . Outside of body  $A$  the unperturbed potential  $U$  is just

$$U = \frac{GM}{r} , \quad (2.100)$$

while the expression for  $\delta U$  can be obtained by inserting Eq. (2.77) into the decomposition in spherical harmonics in Eq. (2.73):

$$\delta U = \sum_{\ell=2}^{\infty} \sum_{m=-\ell}^{\ell} \frac{4\pi G}{2\ell + 1} \frac{I_{\ell m}}{r^{\ell+1}} Y_{\ell m}(\theta, \phi) . \quad (2.101)$$

To find the expression for the total perturbed potential  $\Phi$  acting outside of body  $A$  we shall sum the  $U$  (Eq. 2.100),  $\delta U$  (Eq. (2.101)) and  $U_{tidal}$  (Eq. (2.97)) and exploit Eq. (2.99):

$$\Phi = \frac{GM}{r} - \sum_{\ell=2}^{\infty} \frac{1}{\ell!} \left[ 1 + 2k_\ell (R/r)^{2\ell+1} \right] \cdot \sum_{m=-\ell}^{\ell} \mathcal{E}_{\ell m} r^\ell Y_{\ell m}(\theta, \phi) , \quad (2.102)$$

which can be expressed in a tensorial form by substituting the sum over  $m$  with Eq. (2.95):

$$\Phi = \frac{GM}{r} - \sum_{\ell=2}^{\infty} \frac{1}{\ell!} \left[ 1 + 2k_\ell (R/r)^{2\ell+1} \right] \mathcal{E}_L x^L . \quad (2.103)$$

If we consider only the dominant term in the sum ( $\ell = 2$  term), finally, we get that

$$\Phi = \frac{GM}{r} - \frac{1}{2} \left[ 1 + 2k_2 (R/r)^5 \right] \mathcal{E}_{ij} x_i x_j , \quad (2.104)$$

which is the perturbed potential of the binary system of the two stars A and B.

### 2.4.2 Love Numbers in a Relativistic framework

We will now generalize the Newtonian theory of a tidally deformed binary system to the Relativistic case. The approach used in this Section will be similar to the one of the previous Section as we shall be using a perturbative approach to quantify the effect of the external tidal field. However, in a Relativistic framework, the fundamental quantity which will be affected by the perturbation is the metric. We are, therefore, switching to a geometrical point of view. Note that from this point on we will assume  $G = c = 1$ .

**Equilibrium configuration.** The unperturbed equilibrium configuration is represented by a static and spherically symmetric star which is made of a perfect fluid. As mentioned in 2.2.2, in this configuration the geometry of the space time can be described by the line element

$$ds^2 = g_{\alpha\beta}^{(0)} dx^\alpha dx^\beta = -e^{\nu(r)} dt^2 + e^{\lambda(r)} dr^2 + r^2 (d\theta^2 + \sin^2 \theta d\phi^2) , \quad (2.105)$$

and the stress-energy tensor  $T_{\alpha\beta}$  is defined as

$$T_{\alpha\beta} = (p + \epsilon) u_\alpha u_\beta + p g_{\alpha\beta}^{(0)} , \quad (2.106)$$

where  $u_\alpha$  is the four-velocity field of the fluid,  $p$  is the pressure and  $\epsilon$  is the mass-energy density. The equilibrium configuration is described by the TOV equations (Eq. (2.20)) to which we add a barotropic EoS, i.e.  $\epsilon \equiv \epsilon(p)$ .

**Perturbed configuration in the weak field limit.** Similarly to what we have seen for the Newtonian case, the main quantities describing the perturbation will be the tidal moment STF tensor  $\mathcal{E}_{ij}$  and the quadrupole moment STF tensor, which will now be denoted with  $Q_{ij}$  which are defined, respectively, as

$$\mathcal{E}_{ij} = \frac{\partial^2 U_{tidal}}{\partial x^i \partial x^j} , \quad (2.107)$$

and

$$Q_{ij} = \int d^3 x \rho \left( x_i x_j - \frac{1}{3} r^2 \delta_{ij} \right) . \quad (2.108)$$

In the *weak field limit*<sup>9</sup> this two quantities are proportional to one another, i.e.

$$Q_{ij} = -\lambda \mathcal{E}_{ij} . \quad (2.109)$$

The proportionality constant  $\lambda$  is called *tidal deformability* and can be derived by dimensional analysis<sup>10</sup> as:

$$\lambda = \frac{2}{3} k_2 R^5 , \quad (2.110)$$

where  $2/3$  is a conventional constant factor,  $k_2$  is the  $\ell = 2$ , quadrupolar, dimensionless Love Number and  $R$  is the star radius. Exploiting Eq. (2.110) we can rewrite the perturbed Newtonian potential in Eq. (2.104) as:

$$\Phi = \frac{M}{r} + \frac{3}{2} \frac{Q_{ij}}{r^3} \left( n_i n_j - \frac{1}{3} \delta_{ij} \right) - \frac{1}{2} \mathcal{E}_{ij} x_i x_j , \quad (2.111)$$

where we have also exploited the relations  $n_i = x_i/r$  and  $Q_{ij} x_i x_j = Q_{ij} r^2 (n_i n_j - 1/3 \delta_{ij})$ . The latter holds because  $Q_{ij}$  is trace-less. It can be proven (Ferrari et al., 2020) that in the weak field limit

$$\Phi = -\frac{(1 + g_{00})}{2} , \quad (2.112)$$

---

<sup>9</sup>Assuming the weak field approximation means that the perturbation to the metric is small compared to the unperturbed metric, i.e.  $g_{\mu\nu} = g_{\mu\nu}^{(0)} + h_{\mu\nu}$  and the perturbation  $|h_{\mu\nu}| \ll |g_{\mu\nu}^{(0)}|$ . This assumption is valid when the two bodies in the binary are sufficiently far away from each other.

<sup>10</sup>Note that this constant is of the same kind as the one relating  $I_{\ell m}$  and  $\mathcal{E}_{\ell m}$  in Eq. (2.99).

which can be used to rewrite Eq. (2.111) as

$$-\frac{(1+g_{00})}{2} = \frac{M}{r} + \frac{3}{2} \frac{Q_{ij}}{r^3} \left( n_i n_j - \frac{1}{3} \delta_{ij} \right) + \mathcal{O}\left(\frac{1}{r^3}\right) - \frac{1}{2} \mathcal{E}_{ij} x_i x_j + \mathcal{O}(r^3), \quad (2.113)$$

where we have now specified the order of the next leading terms in the expression of the perturbed potential. The latter can be easily found following the same steps through which we obtained Eq. (2.111). Note that Eq. (2.113) is valid in the star's local asymptotic rest frame (asymptotically mass-centered Cartesian coordinates) at large  $r$ .

Following the approach presented in Thorne & Campolattaro (1967) and Hinderer (2008), our goal now will be to obtain the relativistic expression of  $k_2$  by matching Eq. (2.113) with some asymptotic limit we will derive for the expression of the metric perturbation. First of all, we define the perturbed metric

$$g_{\alpha\beta} = g_{\alpha\beta}^{(0)} + h_{\alpha\beta}, \quad (2.114)$$

where  $g_{\alpha\beta}^{(0)}$  is the background metric for the outer region of a static and spherically-symmetric star defined in Eq. (2.105)), while  $h_{\alpha\beta}$  is the linearized metric perturbation. Note that  $h_{\alpha\beta}$  is a symmetric rank-4 tensor thus it has only 10 independent components which are functions of the coordinates  $(t, r, \theta, \phi)$ . Along with these ten functions we will be interested in studying also the components of the displacement 3-vector  $\xi^j(t, r, \theta, \phi)$  which describes the small-amplitude motion of the fluid elements in the star.

**Decomposition in scalar, vector and tensor spherical harmonics.** As we have seen in 2.4.1, the angular dependence of a perturbation acting on a spherically-symmetric body can be decomposed in terms of special functions called spherical harmonics. Here we want to apply the same strategy for the tensor  $h_{\alpha\beta}$  but with a few clarifications. Firstly, the eigenvalue equation in Eq. (2.70) in General Relativity becomes (Regge & Wheeler, 1957):

$$\gamma^{AB} \nabla_A \nabla_B Y_{\ell m} = -\ell(\ell+1) Y_{\ell m} \quad (2.115)$$

Where  $\gamma^{AB}$  is the metric on the 2-sphere ( $A, B = 1, 2$  and  $x_1 = \theta, x_2 = \phi$ ) defined as

$$\gamma_{AB} = \begin{pmatrix} 1 & 0 \\ 0 & \sin^2 \theta \end{pmatrix}, \quad (2.116)$$

and  $\nabla_A$  is the covariant derivative with respect to the metric. Moreover, in 2.4.1 we have only worked with scalar functions of  $\theta$  and  $\phi$ . When working with  $h_{\alpha\beta}$  the situation becomes more complicated: as mentioned in Regge & Wheeler (1957) under a rotation of the reference frame around its origin the 10 components of  $h_{\alpha\beta}$  transform like 3 scalars ( $h_{00}, h_{01}$  and  $h_{11}$ ), 2 vectors ( $h_{02}, h_{03}$  and  $h_{12}, h_{13}$ ) and one 2-rank tensor when considered as covariant quantities on the 2-sphere.

As we have seen before, scalar angular functions can be decomposed in terms of spherical harmonics  $Y_{\ell m}(\theta, \phi)$  which are said to have a *polar/even parity*. The parity operator  $\mathbb{P}$  corresponds to the angular transformation  $(\theta, \phi) \rightarrow (\pi - \theta, \pi + \phi)$  and if applied to a scalar spherical harmonic  $Y_{\ell m}$  it gives  $(-1)^\ell Y_{\ell m}$ . Thus what we intend when saying that a mathematical object has polar parity means is that under the parity operation  $\mathbb{P}$  it gains a multiplying factor  $(-1)^\ell$ .

Similarly to scalars, vectors and tensors can be decomposed in, respectively, *vector spherical harmonics* and *tensor spherical harmonics*. Vector and tensor harmonics are constructed from scalar harmonics with the purpose of obtaining a covariant object. In the case of vector harmonics, the easiest way to do so is by applying the  $\nabla_A$  to the  $Y_{\ell m}$  functions:

$$\Psi_A^{\ell m} = \text{const} \cdot \nabla_A Y^{\ell m} = \text{const} \cdot \frac{\partial}{\partial x^A} Y^{\ell m} . \quad (2.117)$$

These vector harmonics also have a polar parity and thus we can call them *polar vector harmonics*. However, one can also construct an independent class of vector harmonics as following

$$\Phi_A^{\ell m} = \text{const} \cdot \epsilon_A^B \nabla_B Y^{\ell m} = \text{const} \cdot \epsilon_A^B \frac{\partial}{\partial x^B} Y^{\ell m} , \quad (2.118)$$

where  $\epsilon_{AB}$  is the *Levi-Civita tensor* defined on the 2-sphere

$$\epsilon_{AB} = \begin{pmatrix} 0 & \sin \theta \\ -\sin \theta & 0 \end{pmatrix} . \quad (2.119)$$

Under a parity transformation the vector harmonics  $\Phi_A^{\ell m}$  transform as  $\mathbb{P}(\Phi_A^{\ell m}) = (-1)^{\ell+1} \Phi_A^{\ell m}$  and are therefore said to have an *axial/odd parity*. Thus, we will call these objects *axial vector harmonics*. For rank-2 tensors we can follow a similar procedure, for instance applying the covariant derivative two times or also multiplying the metric  $\gamma_{AB}$  to  $Y_{\ell m}$ . Either way, in this case we will get three classes of tensor harmonics: two having polar parity and one with axial parity (Regge & Wheeler, 1957). We can then imagine to describe the perturbation tensor  $h_{\alpha\beta}$  as the sum of a polar- and axial-parity contribution. Note that we will apply this same decomposition to the angular part of the displacement 3-vector  $\xi^j$ .

**Gauge choice and simplifying assumptions.** For small amplitude motion there is no coupling between the various spherical harmonics and we can study the individual harmonic's contribution to the perturbation separately. Moreover, we can considerably simplify the expression of the thirteen equations governing the components of  $\xi^j$  and  $h_{\alpha\beta}$  by fixing our gauge choice to the Regge-Wheeler gauge. Thorne & Campolattaro (1967) also prove that odd-parity perturbations do not produce any gravitational wave emission. This fact should not be surprising: a pulsation (and the consequent gravitational wave emission) is produced only if the perturbation causes a change in the star's internal pressure,  $p$ , or mass-energy density,  $\epsilon$ . However,  $\epsilon$  and  $p$  are scalar quantities and so they possess an even parity. For this reason, odd-parity perturbations cannot trigger a star pulsation. In the following, we will only study the even-parity terms in the expression of  $h_{\alpha\beta}$ .

Additionally, we will focus our attention on the case of  $\ell = 2$  and  $m = 0$  perturbation (axially-symmetric perturbation).

With these specializations, the tensor  $h_{\alpha\beta}$  can be rewritten as (Hinderer, 2008)

$$h_{\alpha\beta} = \begin{pmatrix} -e^{\nu(r)} H_0(r) & 0 & 0 & 0 \\ 0 & e^{\lambda(r)} H_2(r) & 0 & 0 \\ 0 & 0 & r^2 K(r) & 0 \\ 0 & 0 & 0 & r^2 \sin^2 \theta K(r) \end{pmatrix} P_2(\cos \theta) , \quad (2.120)$$

while the components of  $\xi^i$  become

$$\xi^r = r^{-2} e^{-\lambda/2} W(r) P_2(\cos \theta) \quad ; \quad \xi^\theta = -V(r) r^{-2} \partial_\theta P_2(\cos \theta) \quad ; \quad \xi^\phi = 0 . \quad (2.121)$$

Note that the  $P_\ell(\cos \theta)$  are the *Legendre polynomials*<sup>11</sup>, the functions  $H_0(r)$ ,  $H_2(r)$  and  $K(r)$  are the metric perturbation functions, and  $W(r)$ ,  $V(r)$  are the fluid displacement functions.

Our goal is now to solve the perturbed Einstein equation:

$$\delta G_\beta^\alpha = 8\pi \delta T_\beta^\alpha , \quad (2.122)$$

which links the variation of the pressure and energy-matter distribution ( $\delta T_\beta^\alpha$ ) to the variation of the metric ( $\delta G_\beta^\alpha$ ). The expression of the first-order perturbation of the stress-energy tensor is (Hinderer, 2008):

$$\delta T_\beta^\alpha = \text{diag}(-\delta\epsilon, \delta p, \delta p, \delta p) . \quad (2.123)$$

Note that since the EoS is of the form  $p \equiv p(\epsilon)$  the variation  $\delta\epsilon$  can be rewritten as

$$\delta\epsilon = \left( \frac{dp}{d\epsilon} \right)^{-1} \delta p . \quad (2.124)$$

The expression for the first-order perturbation of the Einstein tensor  $G_{\alpha\beta}$  can be computed from the perturbed metric in Eq.(2.114) knowing that  $h_{\alpha\beta}$  has the expression in Eq. (2.120).

Exploiting Eq. (2.122) and Eq. (2.123) we find that  $\delta G_\theta^\theta - \delta G_\phi^\phi = 8\pi \delta(\delta T_\theta^\theta - \delta T_\phi^\phi) = 0$ . Furthermore, inserting the expression for  $\delta G_\theta^\theta$  and  $\delta G_\phi^\phi$  into this relation we find that  $-H_2 = H_0 \equiv H$ . From  $\delta G_\theta^r = 8\pi \delta T_\theta^r = 0$  we find a relation between  $K'$  and  $H$ , namely  $K'(r) = H'(r) + \nu(r)H(r)$ . Next, we remove all the terms depending on  $\delta p$  in the equations exploiting the relation  $\delta G_\theta^\theta + \delta G_\phi^\phi = 16\pi \delta p$  and by substracting the  $rr$ -component of the Einstein equation to the  $tt$ -component we obtain the following differential equation for  $H$ :

$$H'' + H' \left[ \frac{2}{r} + e^\lambda \left( \frac{2m(r)}{r^2} + 4\pi r(p - \epsilon) \right) \right] + H \left[ -\frac{6e^\lambda}{r^2} + 4\pi e^\lambda \left( 5\epsilon + 9p + \frac{\epsilon + p}{dp/d\epsilon} \right) - \nu'^2 \right] = 0 , \quad (2.125)$$

where the prime denotes  $d/dr$ . To find the expression of  $H$  we first to set the boundary conditions to Eq. (2.125). These can be found by requiring  $H$  to be regular at  $r = 0$  where Eq. (2.125) takes the form<sup>12</sup>

$$H'' + H' \left[ \frac{2}{r} + 4\pi r(p_0 - \epsilon_0) \right] + H \left[ -\frac{6}{r^2} + 4\pi \left( 5\epsilon_0 + 9p_0 + \frac{\epsilon_0 + p_0}{(dp/d\epsilon)_0} \right) \right] = 0 . \quad (2.126)$$

---

<sup>11</sup>These polynomials correspond to the the subset of the spherical harmonics that is left invariant by rotations about the polar axis ( $m = 0$ ).

<sup>12</sup>For  $r \rightarrow 0$ , infact,  $m(r) \rightarrow 4\pi r^3$  (Ferrari et al., 2020). Since  $e^\lambda = (1 - 2m/r)^{-1}$  and  $e^\nu = (1 - 2m/r)$ , this means that  $e^\lambda \rightarrow (1 - 8\pi r^2)^{-1}$  and  $e^\nu \rightarrow (1 - 8\pi r^2)$ . From the latter we obtain  $\nu' = (\log e^\nu)' = e^{-\nu}(e^\nu)' \rightarrow -(1 - 8\pi r^2)r$ . Thus we substitute in Eq. (2.126)  $m \sim 0$ ,  $e^\lambda \sim 1$  and  $\nu' \sim 0$ .

Since we assume  $H$  to be regular near the center we can rewrite it in terms of its Taylor expansion as  $H = a + br + cr^2 + dr^3 + er^4 + \mathcal{O}(r^5)$  and substite it to Eq. (2.126):

$$-\frac{6}{r^2}a - \frac{4}{r}b + (4\pi\alpha_0 b + 6d)r + (14e + 4\pi\alpha_0 c)r^2 + \mathcal{O}(r^3) = 0 , \quad (2.127)$$

where  $\alpha_0$  is a constant factor defined as

$$\alpha_0 = 5\epsilon_0 + 9p_0 + \frac{\epsilon_0 + p_0}{(dp/d\epsilon)_0} . \quad (2.128)$$

Solving individually for the different powers of  $r$  we obtain:

$$\begin{cases} \mathcal{O}(r^{-2}) : & a = 0 \\ \mathcal{O}(r^{-1}) : & b = 0 \\ \mathcal{O}(1) : & \emptyset \\ \mathcal{O}(r) : & 4\pi\alpha_0 b + 6d = 0 \rightarrow d = 0 \\ \mathcal{O}(r^2) : & 14e + 4\pi\alpha_0 c = 0 \rightarrow e = -2\pi/7\alpha_0 c \end{cases} . \quad (2.129)$$

Finally, we can substitute the coefficients into the polynomial and re-express  $H$  as

$$H(r) = a_0 r^2 \left[ 1 - \frac{2\pi}{7} \left( 5\epsilon_0 + 9p_0 + \frac{\epsilon_0 + p_0}{(dp/d\epsilon)_0} \right) r^2 \right] + \mathcal{O}(r^5) , \quad (2.130)$$

where we denoted with  $a_0$  the free coefficient  $c$  which defines a family of solutions for  $H$ . To single out one solution, i.e. fix the value of  $a_0$ , we can exploit the continuity of  $H(r)$  and its derivative across  $r = R$ . Outside the star  $p = \epsilon = 0$  and Eq. (2.125) becomes:

$$H'' + \left[ \frac{2}{r} - \lambda' \right] H' - \left[ \frac{6e^\lambda}{r^2} + \lambda'^2 \right] H = 0 . \quad (2.131)$$

Note that outside the star  $e^\lambda = e^{-\nu} = (1 - 2M/r)^{-1}$  and  $\lambda' = \nu' = 2M/r^2 e^\lambda$ . The quantity  $M = m(R) = 4\pi \int_0^R \epsilon(r) r^2 dr$  is the *total mass-energy* of the star.

Changing variable to  $x = (r/M - 1)$  (Thorne & Campolattaro, 1967) Eq. (2.131) takes the form of the associated Legendre equation with  $\ell = m = 2$ :

$$(x^2 - 1)H'' + 2xH' - \left( 6 + \frac{4}{x^2 - 1} \right) H = 0 . \quad (2.132)$$

The complete solutions to this differential equation is given by a linear combination of the associate Legendre functions of the first and second kind, respectively  $P_\ell^m$  and  $Q_\ell^m$ :

$$H = c_1 Q_2^2(x) + c_2 P_2^2(x) . \quad (2.133)$$

In the limit  $r \gg M$  Eq. (2.133) becomes (Hinderer, 2008):

$$H(r \gg M) = \frac{8}{5}c_1 \left( \frac{r}{M} \right) + \mathcal{O}\left( \left( \frac{M}{r} \right)^4 \right) + 3 \left( \frac{r}{M} \right)^2 + \mathcal{O}\left( \frac{r}{M} \right) , \quad (2.134)$$

where the coefficients  $c_1, c_2$  can now be found by matching Eq. (2.113) with the expression of  $g_{00}$  we can find by exploiting the expression just found for  $H$  far outside

the star. In particular, substituting the expression of  $h_{00}$  (Eq. (2.120)) into Eq. (2.114) we find that

$$g_{00} = g_{00}^{(0)} + h_{00} = -e^\nu [-1 + H(r \gg M)P_2(\cos \theta)] , \quad (2.135)$$

which we can re-express as:

$$-\frac{(1+g_{00})}{2} = \frac{M}{r} + \left(\frac{1}{2} - \frac{M}{r}\right) H(r \gg M)P_2(\cos \theta) \quad (2.136)$$

Next, we substitute Eq. (2.113) and Eq. 2.134 into Eq. (2.136) and obtain

$$\frac{3}{2} \frac{Q_{ij}}{r^3} \left(n_i n_j - \frac{1}{3} \delta_{ij}\right) - \frac{1}{2} \mathcal{E}_{ij} x_i x_j = \left[ \frac{8}{10} \left(\frac{M}{r}\right)^3 c_1 + \frac{3}{2} \left(\frac{r}{M}\right)^2 c_2 \right] P_2(\cos \theta) . \quad (2.137)$$

Similarly to what was done in Eq. (2.95) we now want to express the factors depending on  $Q_{ij}$  and  $\mathcal{E}_{ij}$  in Eq. (2.137) in terms of spherical harmonics. In particular we can say that  $Q_{ij} n^i n^j = \sum_m Q_{\ell m} Y_{\ell m}$  and  $\mathcal{E}_{ij} x_i x_j = \sum_m \mathcal{E}_{\ell m} Y_{\ell m} r^\ell$ , while  $Q_{ij} \delta_{ij} = 0$  because  $Q_{ij}$  is traceless. Moreover, since we are considering only the perturbation with  $\ell = 2, m = 0$  the only terms to consider in the harmonic expansions of  $Q_{ij}$  and  $\mathcal{E}_{ij}$  are  $Q_{20}$  and  $\mathcal{E}_{20}$  which we will call in the following  $Q$  and  $\mathcal{E}$  for simplicity.

Solving, then, Eq. (2.137) we obtain the equation system

$$\begin{cases} \frac{3}{2} Q Y_{20} = \frac{8}{10} M^3 P_2(\cos \theta) c_1 \\ -\frac{1}{2} \mathcal{E} Y_{20} = \frac{3}{2} P_2(\cos \theta) c_2 \end{cases} . \quad (2.138)$$

Finally, we find the expression for the coefficients  $c_1$  and  $c_2$  noting that  $P_2(\cos \theta) = Y_{20}$ :

$$\begin{cases} c_1 = \frac{15}{8} \frac{Q}{M^3} = \frac{15}{8} \lambda \frac{\mathcal{E}}{M^3} \\ c_2 = -\frac{1}{3} M^2 \mathcal{E} \end{cases} , \quad (2.139)$$

where we have exploited the fact that  $Q$  and  $\mathcal{E}$  also satisfy Eq. (2.109). Note that now  $\lambda$  denotes the star deformability defined in (2.110).

We can now solve for  $\lambda$  using the expression of  $H(r)$  and its derivative  $H'(r)$  on the star surface ( $r = R$ ) which can be found from Eq. (2.131) and Eq.(2.139). Finally, using Eq. (2.110) we obtain the relativistic expression of the tidal Love Number  $k_2$ :

$$\begin{aligned} k_2 = & \frac{8\mathcal{C}^5}{5} (1 - 2\mathcal{C})^2 [2 + 2\mathcal{C}(y - 1) - y] \left\{ 2\mathcal{C}[6 - 3y + 3\mathcal{C}(5y - 8)] \right. \\ & + 4\mathcal{C}^3[13 - 11y + \mathcal{C}(3y - 2) + 2\mathcal{C}^2(1 + y)] \\ & \left. + 3(1 - 2\mathcal{C})^2[2 - y + 2\mathcal{C}(y - 1)] \log(1 - 2\mathcal{C}) \right\}^{-1} , \quad (2.140) \end{aligned}$$

where  $\mathcal{C} = M/R$  is called the *compactness* of the star while  $y$  is defined as:

$$y = \frac{RH'(R)}{H(R)} , \quad (2.141)$$

and can be computed by integrating Eq. 2.125 in the region  $0 < r < R$ .

From the Love Number we can define a convenient quantity called *dimensionless tidal deformability*

$$\Lambda = \frac{\lambda}{M^5} = \frac{2}{3}k_2 \left(\frac{M}{R}\right)^{-5} = \frac{2}{3}k_2 C^{-5}. \quad (2.142)$$

Note that, in the following, we will use the terms "tidal deformability" and "dimensionless tidal deformability" interchangeably. This is the parameter which we are going to be interested in studying in the next Chapters and through which we can access the information on the properties of the NS EoS from GW observations.

# Chapter 3

## Neutron star mergers

The collision of two NSs stars belongs to the most violent events in the Universe and produces a wide variety of observables, from GW and neutrino signatures up to electromagnetic signals. The coexistence of these different information channels makes binary neutron star mergers the perfect tool to study the behaviour of matter at supranuclear densities.

In this Chapter we will first describe the evolutionary phases of a NS-NS merger (Section 3.1), secondly we will comment on the properties of its GW emission (Section 3.2) and finally we will review the theoretical models used to describe one of the electromagnetic counterparts of NS-NS merger known as kilonova (Section 3.3).

### 3.1 System evolution

#### 3.1.1 Formation, inspiral and merger

The formation of compact binary systems is a broad and debated topic in Astrophysics. Indeed, many different evolutionary paths can lead to the formation of such systems. In general NS-NS binaries can be divided into two categories depending on their formation channel: *primordial binaries* or *dynamical binaries* (Mapelli, 2017). The former are the result of the evolution of a pre-existent massive binary ( $M_1, M_2 \gtrsim 8\text{-}10 M_\odot$ ) which undergo the supernova phase on different times to eventually produce a NS-NS binary. The latter is formed dynamically through close gravitational interactions between individual NSs captured by their mutual gravitational pull into a close system. This formation channel is relevant in very dense and old stellar environment such as globular clusters. The description of the steps that lead to the formation of the NS-NS binaries is far more complex than the one depicted and beyond the scope of this work. The interested reader can refer to Faber & Rasio (2012) and Mapelli (2017).

After the NS-NS system is formed, the latter will start losing energy due to GW emission, causing the two compact objects to reduce their orbital separation and inspiral towards one another. The GW luminosity of this emission progressively increases leading the system to accelerate its coalescence until the two stars approach a distance comparable to their size. At this point finite-size effects such as tidal interactions become relevant, and may lead part of the NSs material to be disrupted from the surface and expelled mainly over the equatorial plane of the system. When the stars eventually come into contact the merger starts.

### 3.1.2 Post-merger evolution and fate of the remnant

Unlike binary black hole (BH) mergers which can only result in the formation of a more massive BH, NS-NS mergers can produce different post-merger scenarios and remnants (see Fig. 3.1), leading to the formation of a BH, a stable NS or a meta-stable NS, i.e. a NS whose collapse is sustained for a limited amount of time by its rapid rotation. This last case can be divided into two sub-regimes: if the NS can be supported against collapse by uniform rotation the star is called a *supramassive neutron star (SMNS)* while if the star is so massive that it can only be supported by differential rotation, it is called a *hypermassive neutron star (HMNS)*. The latter collapses when the NS core has acquired uniform rotation, around  $\mathcal{O}(100\text{ms})$  after the coalescence.

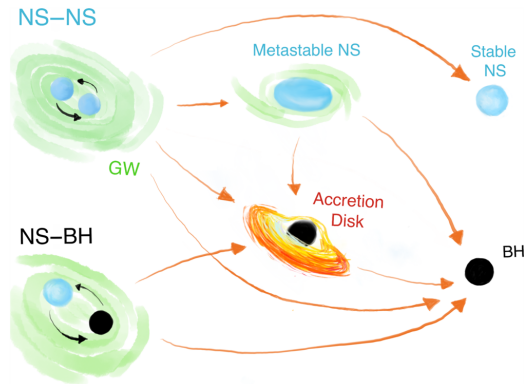


**Figure 3.1.** Artistic representation of the different kinds of post-merger scenarios which can take place for BH-NS and NS-NS coalescences (Ascenzi et al., 2021).

During and after the merger of NS-NS systems part of the NSs material is expelled and becomes unbound through a wide variety of channels. As already mentioned, right before the merger tidal forces can cause the partial disruption of the NSs launching material at mildly relativistic velocities on the orbital plane of the system. Mass outflows can also be produced through various mechanisms acting on the newly formed accretion disk (e.g. neutrino irradiation, nuclear recombination and magnetohydrodynamic viscosity). Finally, further ejection of matter on a broad angular scale is produced by the shocks taking place at the contact interface between the two stars.

Two types of electromagnetic emission are mainly powered within these ejecta. The first one is produced by a relativistic jet of matter (purple component in Fig. 3.2) launched by the remnant through physical processes which are yet to be completely understood. This jet drills through a dense circum-burst medium, previously expelled by the merger (blue component in Fig. 3.2) which gets heated and moved aside by the passage of the jet, forming an hot structure called cocoon (Ascenzi et al., 2021) (yellow component in Fig. 3.2). When this jets starts dissipating its kinetic energy (generally at a distance of  $\sim 10^{13} - 10^{16}$  cm) it powers an intense  $\gamma$  emission which is commonly referred to as *gamma-ray burst (GRB) prompt emission*. Later on, the jet decelerates shocking the interstellar medium (in light blue in Fig. 3.2), powering a fading synchrotron emission from X-ray to radio called *GRB afterglow*.

The other main component of matter released in the coalescence (blue and red components in Fig. 3.2) is a quasi-isotropic component rich of free neutrons and neutron-rich nuclei which composed of a superposition of various outflows. This region represents an ideal site for the *r-process nucleosynthesis* of heavy elements.

The products of the  $r$ -process nucleosynthesis are unstable and their radioactive decay heats up the material itself powering a transient thermal emission from the ejecta known as *kilonova* which we will discuss in more detail in Section 3.3. The features of the kilonova emission are very sensitive to the properties of the progenitor stars, such as their masses and EoS (Metzger, 2020). In Section 5.3 we will implement a numerical pipeline that retrieves the masses and tidal deformabilities from the photometric data of the kilonova AT2017gfo following the work done in Breschi et al. (2021).

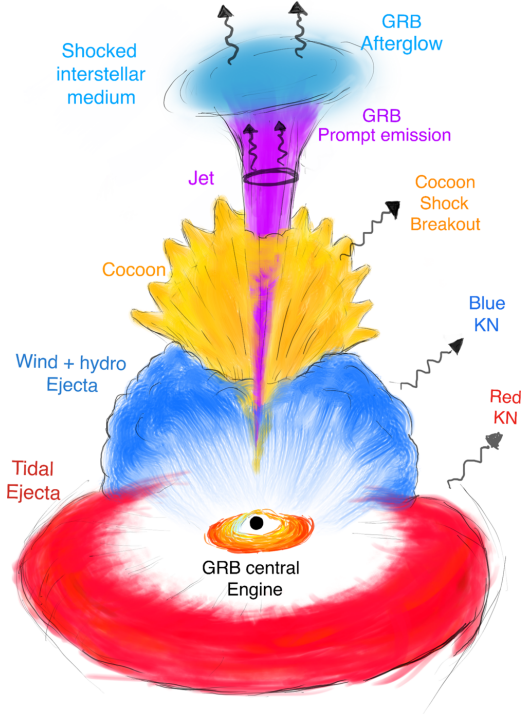


**Figure 3.2.** Overview of the structure of the ejecta launched during a NS-NS merger (Ascenzi et al., 2021).

## 3.2 Gravitational wave emission

As mentioned in Section 3.1, compact binary systems are expected to lose energy through the emission of gravitational waves. The typical GW signal produced by a NS-NS coalescence is presented in Figure 3.4 and it can be divided into:

- the *inspiral signal*: the signal produced when the two stars are so distant that they can be treated as point-like masses;
- the *merger signal*: the signal produced when the stars come into contact and merge to produce a single compact object. In this phase matter and finite size effects become extremely relevant in the case of NS-NS mergers;
- the *ringdown or post-merger signal*: the signal produced by the damped oscillations of the remnant through which it relaxes to a stationary configuration.

In the following we will comment on the properties of each signal individually, focusing our attention on the late-inspiral signal which starts presenting the imprint

of finite-size effects, such as the coupling between tidal interactions and the GW emission, while being also potentially detectable by current GW interferometers.

### 3.2.1 Inspiral emission and tidal imprint

Let us call  $l$  the orbital distance between the neutron stars in the binary, while denoting with  $l_{ISCO} = 6GM/c^2$  the *innermost stable circular orbit*<sup>1</sup>. The latter represents the innermost stable circular orbit for matter which surrounds a compact object. In our case  $l_{ISCO}$  is computed from the total mass of the binary ( $M = m_1 + m_2$ ) and denotes the characteristic orbital distance at which finite-size effect become non-negligible. As long as the two objects are far away from each other, i.e.  $l \gg l_{ISCO}$ , and the weak field interaction is valid, the signal is well described by the quadrupole formula. The frequency of the GW signal increases with time as:

$$\nu_{GW}(t) = \frac{5^{3/8}}{8\pi} \left( \frac{c^3}{G\mathcal{M}} \right)^{5/8} \frac{1}{(t_c - t)^{3/8}}, \quad (3.1)$$

where  $t_c$  represents a typical timescale of the coalescence time of the binary,

$$t_c = \frac{5}{256} \frac{c^5}{G^3} \frac{l_0^4}{\mu M^2}, \quad (3.2)$$

while  $\mathcal{M} = \mu^{3/5} M^{2/5}$  is a combination of the binary reduced mass ( $\mu$ ) and total mass to which all the inspiral signal properties directly depend, also known as *chirp mass*. The time evolution of GW signal's amplitude in the inspiral phase is described by the following equation:

$$h_0(t) = \frac{4\pi^{2/3} G^{5/3} \mathcal{M}^{5/3}}{rc^4} \nu_{GW}^{2/3}(t). \quad (3.3)$$

As consequence of the increase in the GW wave's frequency and amplitude, the signal in the inspiral phase is often called the *chirp* of the GW wave, referring to its similarity to the chirp of a singing bird.

The inspiral is followed by the *late inspiral*, in which  $l \gtrsim l_{isco}$  and the quadrupole formula must be considered as the lowest order of a *post-Newtonian (PN) expansion* (Blanchet, 2014) of the equations of motion in the parameter  $x = v/c$ , with  $v$  being the characteristic orbital speed of the objects in the binary. These PN corrections affect the evolution of the phase of the GW signal which in the early-inspiral phase is determined by:

$$\phi_{GW}(t) = -\frac{1}{16} \left( \frac{c^3}{G} \right)^{5/3} (\pi \mathcal{M} \nu_{GW}(t))^{-5/3} + \text{const.} \quad (3.4)$$

The first correction to the phase is of order  $\mathcal{O}(x)$  and proportional to the mass ratio  $q = m_1/m_2$ , while spin corrections enter at  $\mathcal{O}(x^{1.5})$  and  $\mathcal{O}(x^2)$  order. If the two objects are NSs, tidal interactions also modify the GW phase in Eq. (3.4), entering at  $\mathcal{O}(x^5)$  and  $\mathcal{O}(x^6)$  PN orders as leading contributions. These corrections

---

<sup>1</sup>In this case we are using the expression of the ISCO for a non-rotating compact object.

are proportional, respectively, to the *binary dimensionless tidal deformability* (3.5) and the *tidal asymmetry parameter* (3.6):

$$\tilde{\Lambda} = \frac{16}{13} \frac{(m_1 + 12m_2)m_1^4\Lambda_1 + (m_2 + 12m_1)m_2^4\Lambda_2}{(m_1 + m_2)^5}, \quad (3.5)$$

$$\begin{aligned} \delta\tilde{\Lambda} = & \frac{1}{2} \left[ \sqrt{1 - 4\eta} \left( 1 - \frac{13272}{1319}\eta + \frac{8944}{1319}\eta^2 \right) (\Lambda_1 + \Lambda_2) \right. \\ & \left. + \left( 1 - \frac{15910}{1319}\eta + \frac{32850}{1319}\eta^2 + \frac{3380}{1219}\eta^3 \right) (\Lambda_1 - \Lambda_2) \right]. \end{aligned} \quad (3.6)$$

Note that in Eq.(3.6) the parameter  $\eta$  refers to a symmetric combination of the binary stellar masses, also known as *symmetric mass ratio*, which is computed as:

$$\eta = \frac{m_1 m_2}{M^2} \quad (3.7)$$

Overall, the effect of tidal interactions on the on NS-NS system is to enhance the gravitational wave emission of the binary and thus accelerate the coalescence. This effect is shown in Fig. 3.3 where mock GW signals of NS-NS binaries having different  $\tilde{\Lambda}$  are compared ([Chatzioannou, 2020](#)).

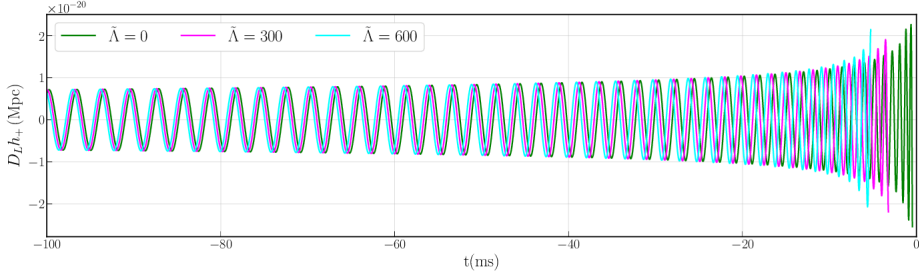


**Figure 3.3.** Rescaled GW signal amplitude for NS-NS systems with different dimensionless tidal deformability ([Chatzioannou, 2020](#)).

Both  $\eta$  and  $\tilde{\Lambda}$  are parameters that depend on the NS EoS and thus will be the quantities of interests for the parameter estimation analysis campaign carried in Chapter 5. Note, however, that a large signal to noise ratio is needed to retrieve the PN tidal correction from the GW detector noise and that the effect of tidal interactions become as more significant as the stars approach the next evolutionary phase of the coalescence, the *merger*, to which current GW detectors are less sensitive (see 3.2.2 for more details). Nevertheless, the tidal correction in  $\tilde{\Lambda}$  is indeed measurable thanks to the fact that the dimensionless tidal deformabilities  $\Lambda_1$  and  $\Lambda_2$  are large for realistic EoSs ([Chatzioannou, 2020](#)). This is not also the case for the correction in  $\delta\tilde{\Lambda}$  which is more problematic to retrieve from GW signals as we will observe in 5.1.2.

### 3.2.2 Merger and post-merger emission

In the merger phase, the GW signal of the binary is strongly affected by strong non-linear effects, partially taken into account in the PN approach. The correct GW signal can only be obtained by solving the complete non-linear Einstein equations

along with the equations of general relativistic hydrodynamics (GRHD). This is usually done in Numerical Relativity simulations (NR) which, however, are computationally expensive, especially when a large number of templates is needed, in order to build template banks of GW signals.

Similarly to the merger, the post-merger dynamics and the corresponding GW spectrum is also affected by a jungle of physical processes (thermal effects, turbulences, neutrino emissions, etc.). However, it emerged from Numerical Relativity simulations that, for most EoSs and NS masses, a hypermassive NS is created and sustained for a time of  $\mathcal{O}(10 - 100)$  ms by its rotation. Moreover, simulations make a robust empirical prediction that during this time the star emits gravitational waves preferably at a characteristic frequency of 1500-4000 Hz, also known as *f-mode*, which is beyond the frequency sensitivity range of current GW detectors.

Although remaining unobserved, the post-merger signal represents an extremely interesting target for next generation detectors, like the Einstein Telescope, since it can probe different regimes of temperature, density and EoS as the hot remnant star will have a higher central density with respect to its progenitors.

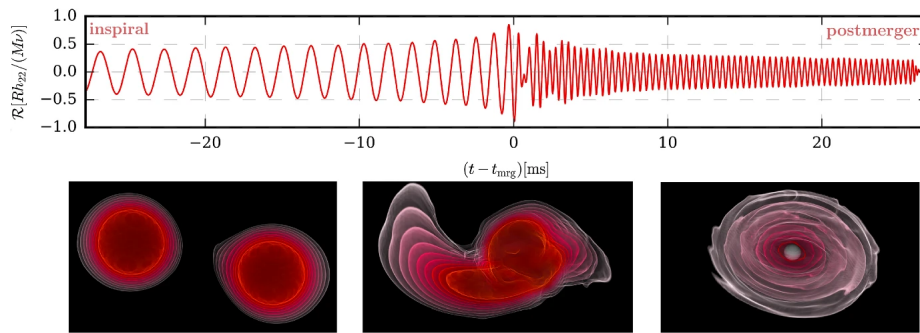


**Figure 3.4.** Representative example of the GW signal emitted by a coalescing NS-NS binary obtained from a NR simulation. Top panel: GW signal emitted during the last orbits before the merger (late-inspiral phase) and during the postmerger phase of the NS-NS coalescence. Bottom panel: Rest-mass density evolution for the inspiral (first panel), the merger (second panel) and the postmerger phase after the formation of the black hole (third panel) (Dietrich et al., 2021).

**Basic concepts of GW detection.** In the following we review the simple model on which modern GW interferometers are based as well as introduce some useful quantities concerning the detection of GWs which we will use in Chapter 5.

The fundamental working principles of the optical configurations behind current GW detectors are build on the *Michelson interferometer*, schematically shown in Fig. 3.5.

This device is composed of two orthogonal arms each having, at one end, a mirror. Light is injected at the other end of one of the two arms, gets splitted at the center of the interferometer by a beam splitter, and directed onto the mirrors. The beams go back and forth along the arms, and when they reach the detector they produce an interference pattern which depends on the delay between their arrivals. In its unperturbed configuration the two arms of the Michelson interferometer have the same length so that the two beams arrive at the detector at the same time. If some

physical process introduces a delay between the beams, for instance changing the length of the two arms, it is detected by the presence of a different interference pattern. Modern interferometers are more sophisticated than this simple model but are based on the same concept: if a GW passes through the instrument it perturbs the length of the two arms introducing a delay between the light beams and, thus, producing an interference pattern.

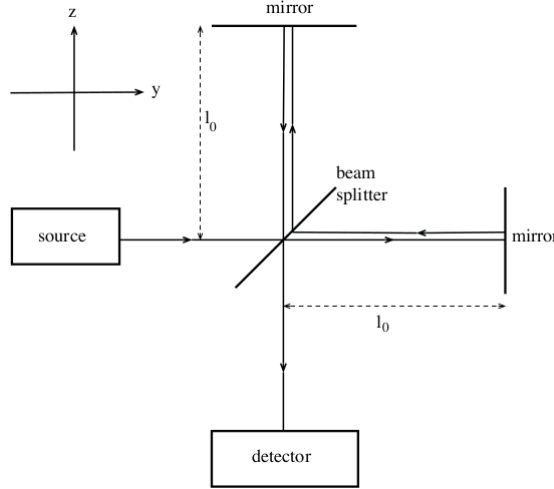


**Figure 3.5.** Schematic view of a Michelson interferometer (Ferrari et al., 2020).

The magnitude of this perturbation is extremely small, with an order of magnitude of one part on  $10^3$  of the size of a proton, such that GW signals detected by LIGO and Virgo are essentially drowned in the noise of the interferometer and require sophisticate data-analysis tools to be identified and correctly interpreted. We can describe the signal in the interferometer as

$$s(t) = h(t, \vec{\theta}) + n(t) , \quad (3.8)$$

where  $h$  is the actual GW signal (which depends on the system parameters  $\vec{\theta}$ ) and  $n$  is the noise of the interferometer which we assume to be stationary Gaussian. To assess if a given perturbation in the instrument is caused by the passage of a GW we can, then, compare the intensity of the signal to the noise background of the detector through the *signal-to-noise-ratio (SNR)*, defined as

$$\text{SNR} = (h|h)^{\frac{1}{2}} = \left( 4 \int_0^\infty \frac{|\tilde{h}(f)|^2}{S_n(f)} df \right)^{\frac{1}{2}} , \quad (3.9)$$

where  $\tilde{h}(f)$  is the Fourier transform of the signal, while  $S_n(f)$  is the *power spectral density (PSD)* of the interferometer and describes the power of the detector noise in the frequency domain. Note that the internal product  $(\cdot | \cdot)$  between two signals  $h(t), g(t)$  is defined as

$$(h|g) = 2 \int_0^\infty \frac{\tilde{h}(f)^* \tilde{g}(f) + \tilde{g}(f)^* \tilde{h}(f)}{S_n(f)} df . \quad (3.10)$$

### 3.3 Kilonovae

In Section 3.1 we introduced the various mechanisms which contribute to unbind part of the material of two NSs during the last phases of a NS-NS coalescence. These ejecta are characterized by a high density of free neutrons and neutron-rich nuclei representing the perfect environment for *r*-processes, rapid and sequential neutron captures on heavy nuclei seeds. The nuclei synthesised by *r*-processes promptly undergo radioactive decay powering a quasi-isotropic emission in the radio, infrared, optical and UV bands called *kilonova*. This transient was firstly observed, concurrently to the GW signal emitted by GW170817, in 2017 about  $\sim 11$  h after the merger. This kilonova is commonly known as AT2017gfo and represents a unique source of information on the physical processes triggered by the coalescence of NS-NS binaries.

In this Section we provide an overview of the theoretical background behind kilonovae also mentioning the general ingredients of a kilonova multicomponent model which we will need for the analysis conducted in Section 5.2.

#### 3.3.1 Toy model

Let us introduce a kilonova toy model based on the simple model discussed in Tanaka (2016). This toy model depends on three basic assumptions:

1. the ejecta is composed of a single spherical component;
2. the ejecta is homogenous;
3. the ejecta expands at constant velocity, (homologous expansion).

These assumptions are rather simplistic but result being very useful to easily obtain the dependence of the luminosity and of its peak, on some of the physical properties of the ejecta such as its mass, velocity and opacity. Let us start by estimating the *optical depth* of the ejecta  $\tau$ :

$$\tau(t) = \rho(t)kR(t) , \quad (3.11)$$

where  $\rho$ ,  $k$  and  $R$  are respectively the mass density, the opacity and radius of the ejecta. Since the latter is assumed to be spherical and homogeneous, the density can be computed as

$$\rho = \frac{3M_{ej}}{4\pi R(t)^3} , \quad (3.12)$$

while from the homologous expansion hypothesis we derive that  $R(t) = v_{ej} \cdot t$ . Substituting these two relations into Eq. (3.11) we obtain:

$$\tau(t) = \frac{3M_{ej}k}{4\pi v_{ej}^2 t^2} . \quad (3.13)$$

The *diffusion time*, i.e. the timescale photons need to escape the ejecta, is proportional to  $\tau$  and can be derived as

$$t_{\text{diff}} = \frac{R}{c}\tau . \quad (3.14)$$

Depending on the value of  $t_{\text{diff}}$  with respect to the dynamical timescale of the expansion, photons might be trapped inside the ejecta ( $t_{\text{diff}} \gg t$ ) or be able escape

efficiently ( $t_{\text{diff}} \ll t$ ). The luminosity peak of the kilonova is obtained when the timescale of expansion is comparable the diffusion timescale. This last statement is known as Arnett's law (Arnett, 1982), given by:

$$t_{\text{diff}}(t_{\text{peak}}) = t_{\text{peak}} . \quad (3.15)$$

Using Eqns. (3.11), (3.14) and (3.15) we obtain the expression of the kilonova peak luminosity time:

$$t_{\text{peak}} = \left( \frac{3kM_{ej}}{4\pi cv_{ej}} \right)^{0.5} \simeq 8.7 \text{ days} \left( \frac{M_{ej}}{0.01M_{\odot}} \right)^{1/2} \left( \frac{v_{ej}}{0.1c} \right)^{-0.5} \left( \frac{k}{10\text{cm}^2\text{g}^{-1}} \right)^{0.5} . \quad (3.16)$$

On the right hand side of Eq. (3.16) we have recast  $t_{\text{peak}}$  in terms of the mass, velocity and opacity of the kilonova ejecta normalized to some typical scales.

To estimate the peak luminosity let us note that the luminosity of the radioactive decays in the ejecta at a generic time can be evaluated as:

$$L(t) = M_{ej}\dot{\epsilon}_n(t) , \quad (3.17)$$

where  $\dot{\epsilon}_n$  is the radioactive heating rate per mass unit which evolves in time following the power law (Tanaka, 2016):

$$\dot{\epsilon}_n(t) \simeq 2 \cdot 10^{10} \text{erg/s} \cdot (t/1 \text{ day})^{-1.3} . \quad (3.18)$$

Since just a part of this energy is deposited in the ejecta<sup>2</sup> we shall express the deposition luminosity as:

$$L_{\text{dep}} = \epsilon_{\text{dep}} M_{ej}\dot{\epsilon}_n(t) \quad (3.19)$$

with the energy deposition fraction,  $\epsilon_{\text{dep}}$ , approximately equal to 0.5 (Tanaka, 2016). By substituting Eq. (3.18) and Eq. (3.16) into Eq. (3.19) we obtain that:

$$L_{\text{peak}} = \epsilon_{\text{dep}} M_{ej}\dot{\epsilon}_n(t_{\text{peak}}) \simeq 1.3 \cdot 10^{40} \text{erg/s} \left( \frac{\epsilon_{\text{dep}}}{0.5} \right)^{0.5} \left( \frac{M_{ej}}{0.01M_{\odot}} \right)^{0.35} \left( \frac{v_{ej}}{0.1c} \right)^{0.65} \left( \frac{k}{10\text{cm}^2\text{g}^{-1}} \right)^{-0.65} . \quad (3.20)$$

From Eq. (3.16) and (3.20) we observe that the overall evolution of the kilonova luminosity is dictated by the mass, velocity and opacity of the ejecta.

### 3.3.2 The role of opacity: blue and red kilonova

As seen in Section 3.3.1, opacity plays a leading role in determining the luminosity evolution and the spectral features of the kilonova. In particular, a very opaque ejecta produces a transient which is less bright and evolves on longer time scales than a low opaque ejecta. The opacity of a kilonova is predominantly determined by the presence of lanthanides and actanides which are ideal to absorb and re-emit a wide variety of photons thanks to their complex electronic structure. Most of lanthanides and actanides are synthesised in the ejecta by  $r$ -processes, i.e. rapid sequential captures of free neutrons on heavy nuclei seeds. These processes are rapid in the sense that neutron captures happen on faster timescales than  $\beta$  decays and fission reactions.

---

<sup>2</sup>For instance the neutrinos produced by  $\beta$ -decays do not contribute to the energy deposited into the ejecta.

As already mentioned in Section 3.1, *r*-processes are triggered in environments with large densities of free neutrons and heavy nuclei seeds, therefore, the efficiency of the lanthanides and actanides production can be expressed in terms of the *electron fraction* of the ejected matter:

$$Y_e = \frac{n_p}{n_n + n_p}, \quad (3.21)$$

where  $n_p$  and  $n_n$  are the proton and neutron number densities. The lower is  $Y_e$ , the more neutron rich is the environment. A typical threshold for lanthanides production is set to  $Y_e \approx 0.25$ : above this threshold the synthesis is efficient, below it the production is considered to be inhibited. Another useful parameter used to describe the opacity of the ejecta is the *lanthanide fraction*  $X_{\text{lan}} = M_{\text{lan}}/M_{\text{ej}}$  which gives the ratio between the mass of the lanthanides in the ejecta and the mass of the ejecta itself. In Figure 3.6 we can observe the effect of opacity on the kilonova emission in delaying the peak of the kilonova and shifting it to redder bands, i.e. bigger wavelengths.

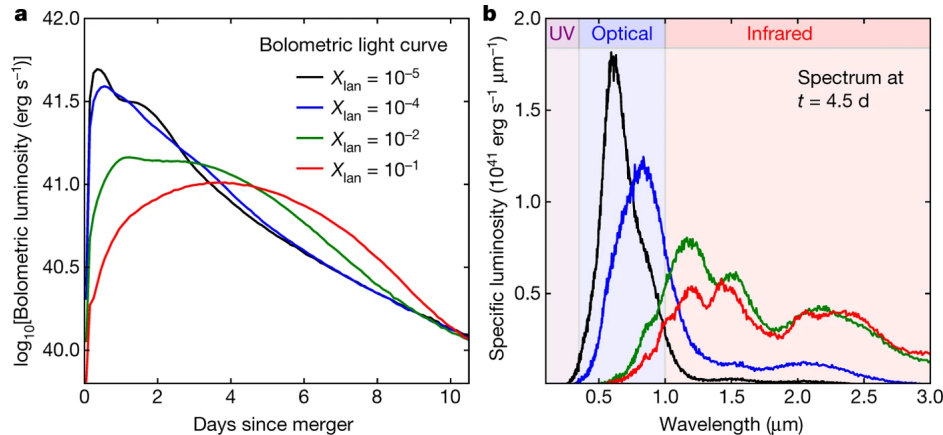


**Figure 3.6.** Comparison between model ejecta with same mass and velocity but different lanthanides fraction. In **a.** are presented the models bolometric lightcurves which show a slower evolution for higher values of  $X_{\text{lan}}$ /opacity. In **b.** are presented the different spectra obtained 4.5 days after the merger. The ejecta with higher  $X_{\text{lan}}$  obscures the optical bands and shift the emission primarily to the infrared (Kasen et al., 2017).

As we shall discuss in 3.3.3, the structure of NS mergers' ejecta is thought to be much more complex than the one depicted in the toy model in 3.3.1 and components with different masses, velocities and  $Y_e/X_{\text{lan}}$  (opacity) contribute to the final kilonova. In general, the kilonova emission is considered to be composed of two sub-emissions: a fast *blue kilonova*, produced by lanthanide-poor/less opaque ejecta, and a slow *red kilonova*, produced by lanthanide-rich/very opaque ejecta. This distinction was also suggested by the spectral evolution of the kilonova AT2017gfo (Kasen et al., 2017) which was firstly observed in the optical band fading rapidly within days while remaining bright in the infrared band for nearly two weeks (Abbott et al., 2017a).

### 3.3.3 Multi-component model

Although the toy model described in 3.3.1 is very useful to understand the main dependencies of the kilonova's features on the properties of the ejected matter, it is too simple to depict the evolution of the kilonova AT2017gfo. This was already

observed in 3.3.2, where we introduced two sub-emissions which contribute to the final kilonova and have to be produced by environments with different chemical compositions. Additionally, hydrodynamical simulations of NS-NS mergers also suggest that several ejection mechanisms occur at different times of the merger producing ejecta components with different mass, velocity and electron fraction. Indeed, some of the NSs matter is released dynamically within milliseconds of the merger (*dynamical ejecta*). Two main mechanisms contribute to this ejecta (Metzger, 2020). First, material at the contact interface between the stars is squeezed out and subsequently expelled by the quasi-radial pulsations of the remnant on a broad angular scale (especially near the polar region). These ejecta have a higher  $Y_e$  because the shocks to which they are subjected induce pair-productions and consequently lead to the capture of positrons by neutrons (Ascenzi et al., 2021). Secondly, some of the material is disrupted from the NSs by their mutual tidal interactions and spread mostly in the equatorial region through angular momentum transport by hydrodynamical processes.

Additional matter is ejected after the dynamical timescale and continuing for up to  $\sim 10$  s after the merger. Indeed, all NS-NS mergers and BH-NS mergers in which the NS is disrupted outside the BH horizon lead to the creation of an accretion disk around the remnant object. Several physical processes can induce the ejection of some of the disk mass producing the so-called *disk outflow ejecta*. For instance, in NS-NS mergers which result in a supramassive/hypermassive NS, the ejection happens while the remnant is still a relevant source of neutrinos. The neutrino irradiation can unbind part of the material of the accretion disk (*neutrino-driven wind ejecta*) and drive the wind outflow's  $Y_e$  to larger values. In addition to neutrinos, viscous torques of dynamical and magnetic origin can also unbind matter from the accretion disk (*viscous ejecta*) (Metzger, 2020).

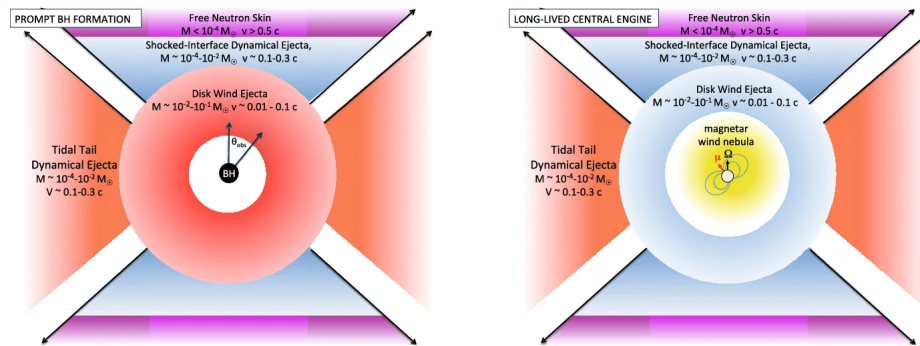


**Figure 3.7.** Overview of the different ejecta components characterizing BH-NS mergers and NS-NS mergers (Metzger, 2020). In both scenarios, the dynamical ejecta in the equatorial plane is highly neutron-rich ( $Y_e \lesssim 0.1$ ) and contributes to the red kilonova emission. Mass ejected dynamically in the polar directions may be sufficiently neutron-poor ( $Y_e \gtrsim 0.3$ ) to inhibit lanthanide production and power blue kilonova emission. The innermost ejecta layers originate from accretion disk outflows. When the merger results in the prompt formation of a BH, the disk wind ejecta is mainly neutron-rich, powering the red kilonova emission. If the remnant is instead a NS long-lived relative to the disk lifetime, then neutrino emission can increase  $Y_e$  sufficiently to suppress lanthanide production and result in blue disk wind emission.

The relative importance of all these components and the processes depends on many factors such as the merger remnant nature (NS/BH) and mass (Figure 3.7) and the EoS. In the next Sections we will see how these information on the system properties can be retrieved from the kilonova focusing on the link between the

features of the emission and of the ejecta, and the EoS of the NS progenitors.

# Chapter 4

## Bayesian inference

Before focusing on the analysis of actual and mock data for the GW and the kilonova signals produced by NS-NS mergers, we must introduce the statistical tools needed to extract relevant information from the data. In particular, we will review the theory behind Bayesian inference and parameter estimation in Section 4.1 and 4.2 while in Section 4.3 we will describe the basic principles of Monte Carlo Markov Chains (MCMC) methods. The latter represent a class of algorithms broadly used to efficiently evaluate the probability distribution of large sets of parameters. In Section 4.4 we will define a category of MCMC samplers, the affine invariant MCMC, whose application to the case of NS-NS mergers is then presented in Section 4.5.

### 4.1 Bayes theorem

Bayes inference provides a powerful approach, widely used in a large variety of scientific branches, to analyze and interpret experimental results. It allows to assess the validity of a certain model or hypothesis for a specific set data, a common problem in science where, given the outcome of an experiment, it is desirable to understand its causes and possibly test different hypothesis against each other. Bayes theorem is mathematically translated by the following relation:

$$P(H|d) = \frac{\mathcal{L}(d|H)P(H)}{P(d)}, \quad (4.1)$$

where its ingredients are:

- the *likelihood*,  $\mathcal{L}(d|H)$ : this is the probability of the data  $d$  being produced under the assumption of the hypothesis  $H$ .
- the *prior*,  $P(H)$ : this represents the prior knowledge we might have on the hypothesis  $H$  being true.
- the *evidence*,  $P(d)$ : this is commonly considered as a normalization factor such that  $\int p(H|d)dH = 1$ , however evaluating this quantity becomes crucial in model selection applications.
- the *posterior*,  $P(H|d)$ : this is the probability of the hypothesis  $H$  being true given we measured the data  $d$ .

## 4.2 Parameter estimation

In parameter estimation the hypothesis is represented by a set of parameters,  $\theta$ , that describe the model we assume to have produced our data,  $d$ . The goal of parameter estimation is, therefore, to infer the value of the most likely set of parameters compatible with the observation. In this framework the Bayes theorem can be expressed as:

$$P(\theta|d) = \frac{\mathcal{L}(d|\theta)P(\theta)}{P(d)} = \frac{\mathcal{L}(d|\theta)P(\theta)}{\int_{\Theta} P(\theta) \cdot \mathcal{L}(d|\theta)d\theta}. \quad (4.2)$$

Since we are now interested in evaluating the relative posterior probabilities of different sets of parameters we can ignore the evidence which is the same for sets of parameters describing the same model. Then the posterior probability can be simply rewritten as:

$$P(\theta|d) \propto \mathcal{L}(d|\theta)P(\theta). \quad (4.3)$$

For instance, in the case of GW analysis, the data  $d$  is given by the strain extracted from interferometers, while the parameters  $\theta$  represent the physical quantities describing the compact binary system and its position in the sky (e.g. masses, spins, etc.).

In general, one is interested in getting the posterior of a subset of all the parameters. To obtain the posterior of a single parameter  $\theta_i$  we have to *marginalize* over the other quantities (the so-called *nuisance parameters*) as following:

$$P(\theta_i|d) = \int_{\Theta} P(\theta|d) \cdot d\theta_1 \dots d\theta_{i-1} d\theta_{i+1} \dots d\theta_n. \quad (4.4)$$

Statistical indicators, such as the expected value  $E[f]$  of a certain quantity  $f$  which is function of the parameters  $\theta$ , can then be computed by integrals over the marginalized posterior, namely:

$$E[f(\theta)] = \int_{\Theta} P(\theta|d) f(\theta) d\theta. \quad (4.5)$$

**Prior.** As we have already mentioned, the prior represents the *a priori* knowledge one has over the quantity studied. Commonly, if no *a priori* knowledge is available for a certain parameter  $\theta_i$  then the prior is chosen to be a uniform distribution over a reasonable range of values for  $\theta_i$ . In this case the prior takes the form:

$$P(\theta_i) = \begin{cases} \frac{1}{\theta_i^{(M)} - \theta_i^{(m)}} & \text{if } \theta_i \in [\theta_i^{(m)}, \theta_i^{(M)}] \\ 0 & \text{else} \end{cases} \quad (4.6)$$

where  $\theta_i^{(M)}, \theta_i^{(m)}$  are, respectively, the maximum and the minimum value accepted for  $\theta_i$ .

**Likelihood.** The most common and easy way to describe the likelihood is by defining it to be a Gaussian distribution<sup>1</sup>. Note that defining a likelihood function

---

<sup>1</sup>This is, for instance, a good starting point for strain noise in GW detectors since the superposition of random noise processes tends to produce a nearly Gaussian distribution. However, if one wants to include non-Gaussian sources of noise (e.g. glitches) the likelihood distribution must be redefined accordingly (Thrane & Talbot, 2019).

implicitly assumes a noise model (Thrane & Talbot, 2019). If one also assumes the data points  $x_i$  of the set  $d$  to be statistically independent, the likelihood takes the form:

$$\mathcal{L}(d|\theta) \propto \prod_{i=1}^N \exp\left(-\frac{(x_i - \mu_i(\theta))^2}{2\sigma_i^2}\right), \quad (4.7)$$

where  $\mu_i(\theta)$  is the expected value for  $x_i$  given the chosen model's parameters  $\theta$ ,  $\sigma_i$  is the noise standard deviation, and  $N$  is the total number of data points in  $d$ . Equation (4.7) is equivalent to:

$$\mathcal{L}(d|\theta) \propto \exp(-\chi^2), \quad (4.8)$$

where the *chi-squared* function  $\chi^2$  is defined as:

$$\chi^2 \equiv \chi_i^2(\vec{x}, \vec{\mu}(\theta), \vec{\sigma}) = \sum_{i=1}^N -\frac{(x_i - \mu_i(\theta))^2}{2\sigma_i^2} \quad (4.9)$$

### 4.3 Monte Carlo Markov Chains

Our goal in the next Sections will be to infer the posterior distribution of parameters describing NS-NS mergers and nucleon interactions inside the star in a Bayesian framework. The posteriors will be computed exploiting Eq. (4.3) using specific sampling algorithms called Monte Carlo Markov Chains (MCMC). The need to use suited numerical strategies to produce the posterior distributions will become clear with a simple example inspired by Thrane & Talbot (2019).

**An intuitive inference example.** Imagine we want to compute the posteriors of some parameters describing a BH-BH merger. For sake of simplicity, let us assume our model depends on 2 parameters only, for example  $M_{chirp}$  and  $d_L$ , and assign for each parameter 10 bins. We can think of the parameter space as a grid 10x10 with each parameter on a different side of the grid. For each square in the grid we would need to evaluate the likelihood<sup>2</sup> and compute the posterior using Eq. (4.3). This would take  $10^2$  operations: the chosen strategy is computationally expensive but still viable. However, what happens if the parameters become 15? We would need to compute  $10^{15}$  operations and our procedure would become computationally prohibitive. In this sense, we can say that our calculations suffer the *curse of dimensionality*.

A solution to this problem is represented by *stochastic samplers*. These samplers are very convenient, for instance, to compute the expected value of a function of the parameter set  $\theta$ . Indeed, if the samples are drawn independently from each other, then the *law of large numbers* tells us that the approximation

$$E[f] = \int_{\theta} P(\theta|d)f(\theta)d\theta \approx \frac{1}{N} \sum_{i=1}^N f(\theta_i) \quad (4.10)$$

is as more valid as larger is the number of samples  $N$ . Moreover, we can imagine the sampled posterior in a multidimensional space as a spreadsheet, the columns

---

<sup>2</sup>Here we are assuming the prior function to be uniform, i.e. constant over the grid.

of which are represented by parameters in  $\theta$ . This has the advantage that if one is interested in computing the marginalized posterior of a subset of the parameters then they can simply "select" the corresponding columns in the spreadsheet (Thrane & Talbot, 2019).

**Markov chains.** Although randomness has its own advantages, we do not want our algorithm to sample in a completely random way. For instance, we would prefer our algorithm to explore the regions of the posterior at high probability rather than the ones at low probability. To do so, we might allow the algorithm to keep track of its previous positions in the parameter space.

Formally speaking, a sequence of events in which the probability for a given event to happen only depends on the previous event is called a *Markov chain* or Markov process. This property can also be expressed as (Sharma, 2017):

$$\text{Prob}(X(t_{n+1})|X(t_1), X(t_2), \dots, X(t_n)) = \text{Prob}(X(t_{n+1})|X(t_n)) , \quad (4.11)$$

with  $X(t_1), \dots, X(t_n)$  sequence of random variables. Furthermore, if the probability of transitioning from a certain state to another is also independent of the number of steps done, the chain is called a *homogeneous chain*. Such a chain is defined by specifying the transitioning probability from one state to another. To summarize, the probability of moving from one state  $X(t_n)$  to another  $X(t_{n+1})$  does not depend on  $t_n$  and it can be defined as:

$$\mathcal{P}_{ij} = \mathcal{P}(X(t_{n+1}) = x_i | X(t_n) = x_j) = \text{Prob}(X(t_{n+1}) = x_i | X(t_n) = x_j) , \quad (4.12)$$

where  $\mathcal{P}_{ij}$  is called the *transition matrix*. In general, the probability of the chain being in a state  $X(t_n) = x_i$  depends both on the time step and on the initial condition  $X(t_0) = x_0$  from which the chain has evolved. This does not happen only if a time-homogeneous Markov chain has an *asymptotic stationary distribution*, meaning that there exist a probability distribution  $\pi$  independent of  $t_n$  and  $X_0$  such that:

$$\lim_{t_n \rightarrow \infty} |\mathcal{P}^{(t_n)}(X(t_n) = x_i | X(t_0) = x_0) - \pi(x_i)| = 0 , \quad (4.13)$$

where  $\mathcal{P}^{(t_n)}(X(t_n) | X(t_0) = x_0)$  means that the chain starts at the initial state is  $X(t_0) = x_0$  and then is evolved applying  $t_n$ -times the transition matrix/operator  $\mathcal{P}(\cdot | \cdot)$  such that the larger  $t_n$ , the more the final distribution will approach the stationary distribution  $\pi$ . The time-homogeneous Markov chain converges to an asymptotic stationary distribution only if it is:

- *irreducible*: it can go from any state  $x_i$  to any other state  $x_j$  in a finite number of steps;
- *positive recurrent*: if the initial state is  $X(t_0) = x_0$  is sampled from  $\pi$  then all the following states will be sampled from  $\pi$ ;
- *aperiodic*: it is impossible for the chain to oscillate periodically between two states.

In general, the probability of sampling the state  $x_i$  at the time  $t_{n+1}$  is given by:

$$\text{Prob}(X(t_{n+1}) = x_i) = \sum_j \mathcal{P}_{ij} \cdot \text{Prob}(X(t_n) = x_j) . \quad (4.14)$$

If the Markov chain has an asymptotic stationary distribution  $\pi$  Eq. (4.14) becomes:

$$\pi_i = \sum_{j \neq i} \mathcal{P}_{ij} \cdot \pi_j , \quad (4.15)$$

where  $\pi_i = \pi(x_i)$ . From this relation we can derive a fundamental equation describing Markovian processes (Angelini, 2022). First, let us note that  $\sum_i \text{Prob}(X(t_{n+1}) = x_i) = \sum_i \pi_i = 1$  (normalization condition). If we sum Eq. (4.15) over  $i$  then we get:

$$1 = \sum_j \pi_j \sum_i \mathcal{P}_{ij} , \quad (4.16)$$

which is satisfied if also  $\sum_i \mathcal{P}_{ij} = 1$ . Exploiting this property of  $\mathcal{P}_{ij}$ , we can say that  $\pi_i = \sum_j \mathcal{P}_{ji} \pi_j$ . Finally, substituting into Eq. (4.15) we can get the relation:

$$\mathcal{P}_{ji} \pi_i = \mathcal{P}_{ij} \pi_j , \quad (4.17)$$

which is called the *condition of detailed balance*. If a Markov chain has a stationary distribution which satisfies Eq. (4.17) then the chain is said to be *reversible*. Infact, the condition of detailed balance basically states that the probability of the present state to be  $x_i$  having a previous state  $x_j$  (i.e.  $\mathcal{P}_{ji} \pi_i$ ) is equal to the probability of the time-reversed process (i.e.  $\mathcal{P}_{ij} \pi_j$ ). The condition of detailed balance represents a sufficient condition for the convergence of the Markov Chain to a stationary distribution and thus is an extremely powerful tool to define the transition matrix  $\mathcal{P}_{ij}$ .

*Monte Carlo Markov chains* are a class of methods for sampling a posterior using Markov chains whose stationary distribution is the desired distribution, in our case the parameter posteriors. The convergence to the stationary distribution is guaranteed by the fact that they are designed to satisfy the condition of detailed balance.

### 4.3.1 Metropolis-Hastings algorithm

One way to satisfy Eq. (4.17) is by choosing the following transition matrix:

$$\mathcal{P}_{ij} = \min \left( 1, \frac{\pi_i}{\pi_j} \right) . \quad (4.18)$$

This choice of  $\mathcal{P}_{ij}$  means that the chain certainly moves from the state  $x_j$  to the state  $x_i$  if the probability of  $x_i$  is higher than the one of the previous state ( $\pi_j/\pi_i < 1$ ). If not, the transition probability is as low as less likely the state is with respect to the previous one and the transition is not accepted if the probability of  $x_i$  is null ( $\pi_i = 0$ ). Equation (4.18) can be modified in order to take into account some a-priori knowledge we might have on the choice of the move:

$$\mathcal{P}_{ij} = u_{ij} \cdot \min \left( 1, \frac{\pi_i}{\pi_j} \right) . \quad (4.19)$$

The symmetric  $u_{ij} = u(x_i, x_j)$  matrix describes the probability of proposing the move  $i \rightarrow j$  and as such is also called *proposal distribution*. In the same way, we can define a matrix called  $a_{ij} = \min(1, \pi_i/\pi_j)$  which represents the *acceptance rate* of the proposed move. The transition matrix in Eq. (4.19) defines the so-called *Metropolis-Hastings (MH) algorithm* (Metropolis et al. (1953); Hastings (1970)) which is described schematically below:

```

initiate  $X_0$ 
for  $j = 1, 2, \dots, N$ :
    sample  $X_j$  from  $u(\cdot, X_{j-1})$ 
    sample a normally distributed variable  $U$ 
    if  $U < \mathcal{P}_{ij}$  accept the move
    otherwise reject the move:  $X_j = X_{j-1}$ 

```

**Weak points of MH and solutions.** This kind of algorithm is the foundation of modern sampling algorithms using MCMCs. However, new samplers stemmed to address the limitations of the MH algorithm. Some of the issues of MH arise from the questions:

1. At what point are the samples representative of the desired distribution?
2. How do we efficiently sample multimodal distributions?
3. How should the scale of the chain's step-size be chosen?

The first issue is linked to the fact that the MCMC samples a distribution which converges to the stationary distribution only after a fair amount of steps. Thus the first draws of the MCMC which are not representative of the desired distribution should be discarded. This is commonly called the *burn-in* process.

The second issue refers to the fact that for multimodal target distributions we must define a strategy to distinguish between local convergence (local maxima of the posteriors) and absolute convergence (absolute maximum). Furthermore, this issue becomes increasingly troublesome as more the local peaks resemble the absolute one and when the peaks are very high compared to their surroundings. This commonly leads MH algorithms to stall on one local peak rather than exploring other regions of the parameter space. One thorough strategy is represented by the *flattening* of the posterior. Instead of the posterior  $P(\theta|d)$  let us sample:

$$P_T(\theta|d) = e^{\frac{1}{T} \ln P(\theta|d)}, \quad (4.20)$$

where  $T > 1$  is often called *temperature* in analogy to thermodynamic systems. The larger is  $T$  the less significant the difference between the peaks and their surrounding. This allows the chain to explore more easily different peaks of the distribution. This idea inspired the *parallel tempering algorithm* (Geyer, 1991) where different chains are ran in parallel at different temperatures and can communicate between one another in such a way that the condition of detailed balance is still satisfied.

The last issue can be understood by making some intuitive examples. Assume the MCMC starts at some random point in the parameter space. There is no reason to believe that this initial position is in the proximity of the peak of the distribution, thus it is desirable for the next chain step to be large enough to move closer to points of higher probability. However, having reached the proximity of the distribution peak after a certain number of iterations it would be inefficient to fix the step size to the initial one. Infact, if the step size is not representative of the width of the peak of the target distribution then it will be increasingly difficult to find points of higher probability, i.e. the MH algorithm will continuously refuse the proposed steps and the chain will stall. Let us make another example considering the following 2-D

distributions (Miller, 2018):

$$P_A(\theta_1, \theta_2) = \frac{1}{2\pi} e^{-\theta_1^2/2} e^{-\theta_2^2/2} ; \quad P_B(\theta_1, \theta_2) = \frac{1}{2\pi} e^{-(\theta_1-\theta_2)^2/2} e^{-(\theta_1+\theta_2)^2/2}. \quad (4.21)$$

The contours of these target distribution for  $e^{-1/2}$  times the maximum probability density are presented in Figure 4.1. Imagine the MCMC reached these portions of the parameter space and now we wish to decrease the step size<sup>3</sup> to explore more efficiently the peak of the distributions. We might decide to shorten the step size equally in the  $\theta_1$ - and  $\theta_2$ -direction. This strategy works to sample  $P_B$ 's peak but it is not efficient for  $P_A$ . Complications arise due to the geometry of the contour for  $P_A$  which is very *anisotropic* compared to the circular contour obtained for  $P_B$ . Following this strategy for  $P_B$ , the step size should be shrunk down to some fraction of the minor axis of the tilted ellipse and this would result in much slower convergence of the MCMC. We shall discuss in the next Section a revised version of the MH algorithm introduced by Goodman and Weare (Goodman & Weare, 2010) which solves this issue by taking into account in a clever way the shape of the distribution.

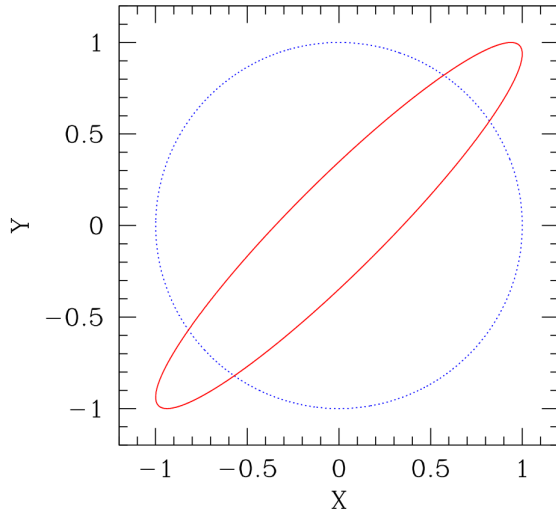


**Figure 4.1.** Contours of the probability distributions in Eq. (4.21) for  $P(\theta_1, \theta_2) = e^{1/2}$  times the maximum probability density (Miller, 2018).

## 4.4 Affine invariant MCMC sampling

The sampling method suggested in Goodman & Weare (2010) is an *affine invariant ensemble sampler*. Ensemble samplers are samplers for which a certain number of chains are initiated at different positions in the parameter space and then evolved in parallel. The chains that constitute the ensemble are usually called *walkers*. The affine invariance property implies that the performance of the method is independent of the aspect ratio in highly anisotropic distributions. An affine transformation is a map between  $\mathbb{R}^n$  and  $\mathbb{R}^n$  of the form  $Y = A \cdot X + b$ . If  $X$  has probability distribution  $\pi(X)$  then  $Y$  has a probability distribution:

$$\pi(Y)_{A,b} = A \cdot \pi(X) + b \propto \pi(X). \quad (4.22)$$

---

<sup>3</sup>For simplicity we are considering an initial step which has the same size in the  $\theta_1$ -direction and the  $\theta_2$ -direction.

Let us consider a very anisotropic distribution, similar to  $P_B$  presented in Eq. 4.21:

$$\pi(\theta_1, \theta_2) \propto e^{-(\theta_1 - \theta_2)^2/2\epsilon} e^{-(\theta_1 + \theta_2)^2/2}, \quad (4.23)$$

where the parameter  $\epsilon$  determines the aspect ratio of the elliptic contours of the distribution. In the regime  $\epsilon \ll 1$ , the ellipses become more and more stretched and the treatment of the chain step size gets very problematic for standard MCMC algorithms. However, if one introduces the affine transformation:

$$\phi_1 = (\theta_1 - \theta_2)/\sqrt{\epsilon} \quad , \quad \phi_2 = \theta_1 + \theta_2 \quad , \quad (4.24)$$

the distribution in Eq. (4.23) takes a much simpler form:

$$\pi(\phi_1, \phi_2) \propto e^{-\phi_1^2/2} e^{-\phi_2^2/2} \quad , \quad (4.25)$$

which is a well scaled distribution that does not require detailed customization.

The idea behind affine invariant samplers is to update the position of each walker in the parameter space based on an affine invariant transformation which is constructed using the current positions of the other walkers<sup>4</sup>. Let us analyse in more detail the updating procedure of the ensemble. Imagine we have  $L$  walkers denoted with  $\vec{\mathbf{X}}(t) = [X_1(t), X_2(t), \dots, X_L(t)]$ . One step of the ensemble, one overall update, consists of one cycle over the  $L$  walkers:

```
for k = 1, 2, .., L:  
    update X_k(t) → X_k(t + 1)
```

The position of a generic walker  $X_k(t)$  is updated exploiting the information on the position of the remaining  $L - 1$  walkers, i.e. the so-called *complementary ensemble*:

$$\vec{\mathbf{X}}_{[k]}(t) = \{X_1(t + 1), X_2(t + 1), \dots, X_{k-1}(t + 1), X_{k+1}(t), \dots, X_L(t)\} \quad . \quad (4.26)$$

The simplest update algorithm recommended in Goodman & Weare (2010) is the *stretch move*. In the stretch move the position of a walker  $X_k(t)$  is updated based on the position of one randomly-picked walker  $X_j$  belonging to  $\vec{\mathbf{X}}_{[k]}(t)$  (i.e.  $j \neq k$ ). More specifically, the proposal is of the form:

$$X_k(t) \rightarrow Y = X_j + Z \cdot (X_k(t) - X_j) \quad , \quad (4.27)$$

with  $Z$  being a scaling variable the distribution of which is often chosen to be:

$$g(Z) \propto \begin{cases} \frac{1}{Z} & \text{if } Z \in \left[\frac{1}{a}, a\right] \\ 0 & \text{otherwise.} \end{cases} \quad , \quad (4.28)$$

where  $a > 1$  can be adjusted to improve the MCMC performance. A common choice is  $a = 1/2$ . Assuming the parameter space has  $n$  parameters, the appropriate acceptance rate for this move is:

$$a_{jk} = \min \left[ 1, Z^{n-1} \frac{P(Y|X_j, X_k(t))}{P(X_k(t))} \right] \quad . \quad (4.29)$$

---

<sup>4</sup>This is of course different from the example presented at the beginning of the Section where the expression of the target distribution was supposed to be known a-priori.

The update operation  $X_k(t) \rightarrow X_K(t+1)$  is structured as following:

```

for  $k = 1, 2, \dots, L$ :
  choose  $X_j \in \vec{\mathbf{X}}_{[k]}(t)$  at random
  generate  $Y = X_j + Z(X_k(t) - X_j)$ 
  accept, set  $X_k(t+1) = Y$ , with probability (4.29)
  otherwise reject, set  $X_k(t+1) = X_k(t)$ 

```

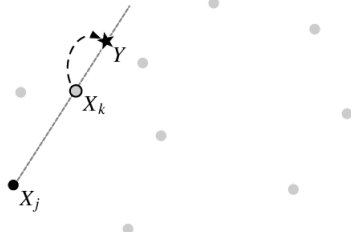


**Figure 4.2.** Simple representation of a stretch move. The gray dots represent the walkers not participating in the move. The proposal is generated by stretching along the straight line connecting  $X_j$  to  $X_k$  (Goodman & Weare, 2010).

In the next Section we will review the Fortran implementation of Goodman & Weare (2010) algorithm which we will use in Chapter 5 to perform the parameter estimation on the NS-NS mergers GW and kilonova signals.

## 4.5 Our case of study: retrieving nucleon interactions

In Section 2.3 we have introduced the NS EoS properties and described the theoretical model employed in Sabatucci et al. (2022) to describe nuclear dynamics within NSs. The latter is defined by a non-relativistic nuclear many-body hamiltonian (Eq. 2.31) which is modified by introducing a free parameter called  $\alpha$  that defines the amplitude of three-nucleon repulsive interactions. These interactions are hardly constrained above saturation density and largely determines the NS EoS stiffness. Therefore, we are now interested in defining a method through which  $\alpha$  can be retrieved from the GW and kilonova signals of NS-NS mergers, in particular from the binary symmetric mass ratio,  $\eta$ , and tidal deformability,  $\tilde{\Lambda}$  (see Section 3.2). The posterior of  $\eta$  and  $\tilde{\Lambda}$  will be recovered from the signals following the methods described in Section 5.1 (GW data) and 5.2 (kilonova data). For our purpose now, we assume to have already obtained them from the data.

### 4.5.1 Inference framework

As explained in Sabatucci et al. (2022), Bayes theorem can be exploited in such a way as to link the posterior of parameters describing the stellar interior to the posterior of the average macroscopic quantities characterizing the stars, such as the masses and the tidal deformabilities. In our case, the interior parameters are the two stars central pressures,  $p_c^{(1)}$  and  $p_c^{(2)}$ , and the three-nucleon repulsive potential amplitude,  $\alpha$ . These parameters completely determine the EoS of the stars as well as their macroscopic properties. Denoting with  $\theta$  the set of the interior parameters

and with  $O$  the observed astrophysical data set, we can rewrite:

$$P(\theta|O) \propto P_0(\theta) \cdot \mathcal{L}(O|D(\theta)) , \quad (4.30)$$

where  $D(\theta)$  is the set of NS observables that can be inferred from the data. In our case,  $O$  corresponds either to GW strain data modeled on the properties of GW170817/GW190425 or on the data of AT2017gfo, while  $D(\theta)$  correspond to the chirp mass  $\mathcal{M}_{chirp}$ , the symmetric mass ratio  $\eta$  and the binary tidal deformability  $\tilde{\Lambda}$ . Thus, the likelihood in Eq. (4.30) can be rewritten as  $\mathcal{L}(O|\eta, \tilde{\Lambda}, \mathcal{M}_{chirp})$ . The latter can be evaluated from the joint posterior  $P(\mathcal{M}_{chirp}, \eta, \tilde{\Lambda}|d)$  exploiting again Bayes theorem. This calculation can be simplified beforehand by exploiting the accuracy to which the chirp mass is inferred from GW signals and fixing it to its median value<sup>5</sup>. This reduces the parameter space speeding up the likelihood evaluation and allowing us to compute the mass of the secondary NS directly from the mass of the primary object, i.e.  $m_2 = m_2(\mathcal{M}_{chirp}, m_1)$ .

Taking all the previous considerations into account, Eq. (4.30) becomes:

$$P(\alpha, p_c^{(1)}|O) \propto P_0(\alpha, p_c^{(1)}, p_c^{(2)}) \cdot \mathcal{L}(O|\eta, \tilde{\Lambda}, \mathcal{M}_{chirp} = \mathcal{M}^*) , \quad (4.31)$$

where  $\mathcal{M}^*$  is the estimated median value of  $\mathcal{M}_{chirp}$  and the likelihood function is evaluated as in Eq. (4.32). The latter can be further simplified by replacing the conditional posterior  $P(\eta, \tilde{\Lambda}|O, \mathcal{M}_{chirp} = \mathcal{M}^*)$  with the marginalized posterior  $P(\eta, \tilde{\Lambda}|O)$ . This can be done with good accuracy as shown in [Raaijmakers et al. \(2021\)](#), such that:

$$\mathcal{L}(O|\eta, \tilde{\Lambda}, \mathcal{M}_{chirp} = \mathcal{M}^*) = \frac{P(\eta, \tilde{\Lambda}|O)}{P_0(\eta, \tilde{\Lambda})} . \quad (4.32)$$

Since the priors on  $\tilde{\Lambda}$  and  $\eta$  were always chosen to be uniform we can re-express Eq. (4.32) in a logarithmic form as:

$$\log \mathcal{L}(O|\eta, \tilde{\Lambda}, \mathcal{M}_{chirp} = \mathcal{M}^*) = \log P(\eta, \tilde{\Lambda}|O) + C , \quad (4.33)$$

where  $C = \log P_0(\eta, \tilde{\Lambda})$  is the constant factor which we ignore in the sampling procedure.

### 4.5.2 Sampling procedure

The posterior  $P(\alpha, p_c^{(1)}|O)$  is evaluated from the posterior  $P(\eta, \tilde{\Lambda}|O)$  through a Fortran code which implements the *emcee* sampler ([Foreman-Mackey et al., 2013](#)) with stretch move. Emcee is, infact, the implementation of the affine invariant MCMC sampler of [Goodman & Weare \(2010\)](#).

For our calculations the number of walkers ran in the sampling has been fixed to 20 while the number of walker steps to  $2 \cdot 10^6$ , of which  $1 \cdot 10^6$  steps are discarded as burn-in. Note that, throughout the code, the masses and tidal deformabilities of the stars are computed from  $\alpha$  and the stellar central pressures without directly integrating the TOV equations (Eq. 2.20). This is achieved exploiting a set of input files which contain the values of  $\alpha$  and  $p_c$  along with the values of the respective equilibrium mass ( $m$ ) and tidal deformability ( $\Lambda$ ). The latter were computed in

---

<sup>5</sup>We generalize to the case of the kilonova emission assuming  $\mathcal{M}_{chirp}$  to have been evaluated from its GW counterpart.

previous studies by integrating the TOV equations over a grid 4000x4000 couples  $(\alpha, p_c)$ , with  $\alpha \in [0.7, 2]$  and  $\log_{10}(p_c) \in [-5, -2.5]$ . The values of  $m$  and  $\Lambda$  and the respective  $(\alpha, p_c)$  tuples are read and interpolated in the code so that at the relations  $m(\alpha, p_c)$  and  $\Lambda(\alpha, p_c)$  are obtained.

The sampling procedure for each walker can be broken down into the following steps:

1. A sample  $(\bar{\alpha}, \bar{p}_c^{(1)})$  is drawn from the priors. More specifically,  $\alpha$  is uniformly sampled in the range  $[0.7, 2]$  while the central pressure of each star is uniformly sampled in the logarithmic space between<sup>6</sup>  $\log_{10} p_c^{\min}(\alpha) \approx 34.78$  and  $\log_{10} p_c^{\max}(\alpha)$ , where  $p_c^{\max}$  is the central pressure of the heaviest stellar configuration expected for a fixed EoS, i.e a fixed value of  $\alpha$  .
2. The mass of the first star is computed exploiting the interpolated relations  $m(\alpha, p_c)$ , i.e.  $m_1 = m(\bar{\alpha}, \bar{p}_c^{(1)})$ . The mass of the second mass is then computed from the primary mass and the chirp mass (which is provided as an input parameter);
3. The central pressure of the second star,  $\bar{p}_{c,(2)}$  is found through a Newton-Raphson method algorithm as the zero of the function:  $f = m(\bar{\alpha}, p_c) - m_2$ .
4. The star tidal deformabilities are computed exploiting the interpolated relation  $\Lambda(\alpha, p_c)$ , i.e.  $\Lambda_1 = \Lambda(\bar{\alpha}, \bar{p}_c^{(1)})$  and  $\Lambda_2 = \Lambda(\bar{\alpha}, \bar{p}_c^{(2)})$  ;
5. Having  $m_1, m_2, \Lambda_1$  and  $\Lambda_2$ , the symmetric mass ratio and the binary tidal deformability are computed as in Eq. (3.7) and Eq. (3.5);
6. The log-likelihood is computed as in Eq. (4.33). Note that the joint posterior  $P(\eta, \tilde{\Lambda}|O)$  is obtained before the sampling starts by interpolating the discrete sampled posteriors of  $\tilde{\Lambda}$  and  $\eta$  provided as input files to the code;
7. The log-posterior of  $(\bar{\alpha}, \bar{p}_c^{(1)})$  is evaluated from the logarithmic expression of Eq. (4.30), then the position of the walker is updated through the *emcee* sampler with a stretch move (see Section 4.4).

**Addendum: computing the tidal deformability.** In the following we briefly review the structure of a code in Fortran obtained by exploiting some of the functions used for the MCMC sampling procedure described in 4.5.2 which allows us to compute the tidal deformability of a NS,  $\Lambda$ , knowing its mass and  $\alpha$  . This code will be used to produce mock GW and kilonova signals in 5.1.2 and in 5.2.3. In particular the code:

1. Computes the star central pressures through a Newton-Raphson method applied to the function  $f = m(\alpha, p_{c,(i)}) - m_i$ , where  $i = 1, 2$  is the star index and  $\alpha, m_1$  and  $m_2$  are given as input parameters;
2. Computes the tidal deformabilities using the interpolated relation  $\Lambda(\alpha, p_c)$ .

---

<sup>6</sup>Note that  $p_c$  here is expressed in dyne/cm<sup>2</sup>.

## Chapter 5

# Multimessenger analysis of neutron star mergers

In this Chapter we shall assess the capability of *multiples messenger* observations of NS-NS binaries to constrain the microphysical parameters underlying the neutron star EoS. More specifically, we will focus on the gravitational wave and electromagnetic signatures of NS-NS mergers. However, GWs and photons represent only a subset of the different astrophysical emissions known. The complete list of messengers is composed of:

- neutrinos ( $\nu, \bar{\nu}$ )
- photons ( $\gamma$ )
- gravitational waves (GW)
- cosmic rays (CR)

The branch of physics that studies astrophysical objects by combining information carried by different messengers is called *Multimessenger Astrophysics*. The joint analysis of these messengers is extremely instructive since the information carried by any one of them is qualitatively different, as well as complementary to each other, allowing for a better characterization of the source properties.

At the end of the Chapter we will exploit this approach building a numerical pipeline which combines the data coming from the inspiral emission of NS-NS coalescences with the one associated to the kilonova. The ultimate goal of such framework is to produce the posterior distribution of the amplitude of three-nucleon repulsive interactions within the stellar cores, which largely determines the stiffness of NS EoS.

The Chapter is structured as follows: in Section 5.1 we will present the analysis conducted on mock inspiral signals modeled on the properties of GW170817 and GW190425, in Section 5.2 we will follow a similar approach, inspired by the work of [Breschi et al. \(2021\)](#), studying the data of the kilonova AT2017gfo and, finally in Section 5.3 we will combine the analysis of the real strain data of GW170817 with the one of AT2017gfo in order to obtain a multimessenger measurement of the amplitude of three-nucleon repulsive interactions, also exploring possible generalization to mock signals of the two type of emissions considered.

## 5.1 GW170817 and GW190425

The discovery of GW170817 represented the first GW detection of a binary neutron star system, also marking the beginning of the multimessenger era. The event was, indeed, followed by the observation of two different electromagnetic counterparts. The first one, detected by the Fermi and INTEGRAL gamma-ray telescopes approximately 1.7s after the merger, was a short gamma-ray burst (GRB), thereafter called GRB170817A (Abbott et al., 2017b). The second signal was an unprecedented electromagnetic transient discovered  $\sim 11$ h after the merger, the kilonova AT2017gfo (Abbott et al., 2017a).

The second NS-NS coalescence, GW190425, was somewhat a more unlucky detection. At the time of the observation only LIGO Livingston and Virgo were operational. The signal had an SNR (Eq. 3.9) of 12.9 in LIGO Livingston and a SNR of only 2.5 in Virgo (Abbott et al., 2020), below the noise threshold, making GW190425 arguably a single-detector event. Since GW localization relies predominantly on measuring the time delay between different observatories, the sky map for this event was very wide ( $\sim 8300 \text{ deg}^2$ ). For comparison, GW170817 had a SNR of 18.8, 26.4, and 2.0 respectively for LIGO Livingston, LIGO Hanford and Virgo and its reconstructed sky localization from the three GW detections spanned an area of  $\sim 28 \text{ deg}^2$  (Abbott et al., 2017a). Furthermore, the NS-NS system that produced GW190425 was approximately 4 times<sup>1</sup> more distant from Earth than the one that originated GW170817 making it far less loud in the interferometers. Finally, no matching electromagnetic counterpart was observed in coincidence with the GW trigger.

In the following we will first study mock signals of the two events exploiting Fortran and Python codes tailored to recover the injected value of the three-body nucleon amplitude  $\alpha$  in order to assess the accuracy to which this parameter can be retrieved by current GW detectors at design sensitivity and by third generation interferometers. As discussed above, to this aim we will inject signals with the same properties of GW170817 and GW190425, and specific values of  $\alpha$  (i.e. specific EoS) within the noise spectral densities of LIGO/Virgo and ET. Then, in Section 5.3 we will conduct a similar study on  $\alpha$ , focusing on real data, i.e. on the observed strain of GW170817. We will exploit a pre-existing analysis developed in Maselli et al. (2021) and Sabatucci et al. (2022) for the GW inspiral signal, and combine it with the original results carried out in this work exploiting the kilonova data of AT2017gfo (Section 5.2), discussing the properties of the multimessenger distribution of  $\alpha$ .

### 5.1.1 Code overview

The goal of our analysis is to retrieve the joint posterior distribution of the binary dimensionless tidal deformability,  $\tilde{\Lambda}$ , and of symmetric mass ratio,  $\eta$ . Both of them depend on the stellar EoS and will be used afterwards to obtain the distribution of the amplitude that quantifies the strength of the three-nucleon repulsive interactions,  $\alpha$ , which is a free parameter in the nuclear model described in 2.3.2. To perform the parameter estimation analysis on the mock signals, a numerical pipeline was defined and implemented following the scheme in Fig. 5.1. The pipeline exploits both pre-existing codes in Fortran for the implementation of Monte Carlo Markov Chains (see Section 4.5 for more details), as well as newly written Python codes

<sup>1</sup>The distance constrain for GW190425 is  $159^{+69}_{-71}$  Mpc (Abbott et al., 2020) while for GW170817 is  $40^{+8}_{-14}$  Mpc (Abbott et al., 2017a)

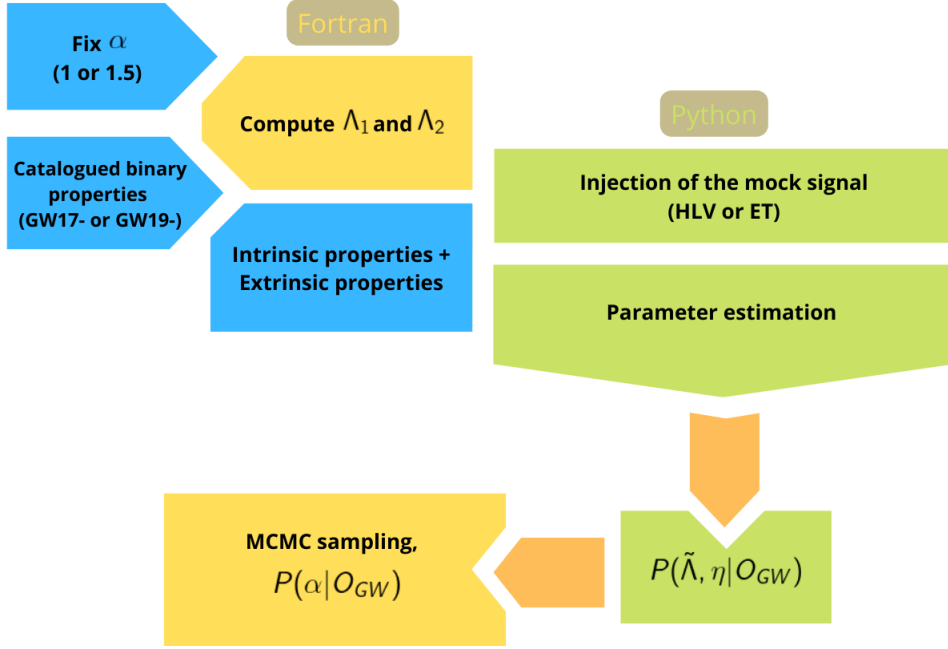


**Figure 5.1.** Flow chart of the numerical pipeline defined to hierarchically infer the amplitude of three-nucleon forces from the simulated detection of inspiral GW signals emitted by NS-NS mergers.

which perform the injection and analysis of the mock GW signals in `bilby`. The latter is a Python library used in GW astronomy to perform data analysis and inference following a Bayesian approach (Ashton et al., 2019).

As shown in the blue boxes in Fig. 5.1, the pipeline starts by fixing the value of  $\alpha$  and extracting the binary fundamental parameters from LIGO-Virgo Gravitational Wave Open Science Center (GWOSC) event catalogue (available at this [link](#)). These parameters will constitute the set of *injection parameters* of the mock GW signal, i.e the quantities defining the waveform. The injection parameters can be divided into two categories:

- *intrinsic parameters*: the properties of the NS-NS binary which are independent on the observer position. They are the stellar masses ( $m_1, m_2$ ), dimensionless spins ( $\chi_1, \chi_2$ ) and tidal deformabilities ( $\Lambda_1, \Lambda_2$ ).
- *extrinsic parameters*: the quantities that refer to the position of the source in the sky with respect to the observer, the time at which the event took place and the response function of the detectors. They are the source luminosity distance ( $d_L$ ), its angular coordinates ( $ra$  and  $dec$ ), the inclination of the binary ( $\theta_{jn}$ ) with respect to the line of sight, the geocentric time of the coalescence, the polarization angle ( $\psi$ ) and the phase of the GW at a reference frequency<sup>2</sup> of 50 Hz ( $\phi$ ).

<sup>2</sup>Indeed, some parameters of the binary are defined in `bilby` at a reference frequency which must be specified beforehand [Ashton et al. (2019); Romero-Shaw et al. (2020)] and which is generally fixed to 50 Hz.

The values of the injection parameters for the two events are presented in Table 5.2 and Table 5.3.

**GW170817 injection parameters.** In the case of GW170817, the source angular position was fixed to be the one of the identified host galaxy NGC4993 (Abbott et al., 2017a), while the masses, spins, luminosity distance and inclination angle were retrieved<sup>3</sup> from Table II in Abbott et al. (2019). The value of the phase was arbitrarily fixed to 1.3 rad. Indeed,  $\phi$  injected value is irrelevant for our analysis as we choose to marginalize over this parameter. Since it was not possible to find the credible intervals of  $\psi$  in literature, its value was fixed by matching the SNR obtained by a benchmark injection of GW170817 in `bilby` (see Appendix A), to the actual SNR reported in Abbott et al. (2019). Note that the PSDs used for the benchmark injection were the one of LIGO-Virgo interferometers in the O2 run available at [link](#). For a polarization angle of  $\psi = 2.659$  rad, the SNR of the mock signal in the interferometers is of 19.5 for LIGO Hanford, 26.1 for LIGO Livingston and 3 for Virgo, very close to the values of SNRs (18.8, 26.4, 2.0) determined by the LIGO-Virgo collaboration itself. To correct for the small deviation from the target SNRs, the luminosity distance of the event has been rescaled as:

$$d'_L = d_L / R , \quad (5.1)$$

where  $R$  is the ratio between the total SNR<sup>4</sup> of the real detection (32.4) and the total SNR of the benchmark simulation (32.78). By applying this rescaling we have, indeed, exploited the fact that the total SNR approximately scales as the inverse of the luminosity distance.

**GW190425 injection parameters.** In the case of GW190425, the values of each injected parameter corresponded to the medians of the low-spin posteriors available for the event on Zenodo ([link](#)).

**Tidal deformabilities.** For both events the injected values of the NSs tidal deformabilities  $\Lambda_1$  and  $\Lambda_2$  were computed in the Fortran code described in 4.5.2 fixing the stellar masses to correspond to their injected values, and the microphysical parameter  $\alpha$  to be either 1 or 1.5 (yellow box on the top-right side of Fig. 5.1). Note that as  $\alpha$  increases, the EoS becomes stiffer (see Fig. 2.5). The two values of  $\alpha$  have been chosen to span a large range of stellar compactness, which is the main quantity characterizing the tidal deformabilities, and to study how it affects the multimessenger analysis we performed.

**Waveform model.** The injection parameters represent the input parameters of our *waveform approximant*, i.e. the method that produces a simulated GW signal from the properties of the binary. Different approximants are available depending on the physical effects taken into account (e.g. spin precession, tidal effects). The approximant we have used is Taylor F2 which determine the Fourier transform of the strain with the stationary phase approximation. To produce the mock signals, other additional parameters are needed: the signal minimum frequency, the duration and the sampling frequency. The former was fixed to 30 Hz while the duration of

---

<sup>3</sup>Note that the masses of the stars have been taken as the mean of the credible intervals obtained in Abbott et al. (2019), while the injected spins have been fixed to zero.

<sup>4</sup>The total SNR of the interferometer network is computed as the root sum square of the individual interferometers' SNRs.

the mock signal was fixed to be 64s, of which 2s past the geocentric time (i.e. after the merger). Finally, the sampling frequency was chosen to be equal to 4098 Hz.

**Detectors.** Next, the mock signals of GW170817 and GW190425 were injected in either one of two different detector configurations, always assuming no instrumental noise<sup>5</sup>. The first interferometer configuration studied consisted of a network of LIGO Hanford, LIGO Livingston and Virgo (HLV network) with expected sensitivity curves for the O4 run, which is planned to start in March 2023. The second configuration consisted only of the Einstein Telescope (ET), a 3rd-generation interferometer to be online by mid-2030s. Note that the minimum frequency detectable by the two configurations was fixed to correspond to the minimum frequency of the mock signal. The *amplitude spectral density (ASD)*<sup>6</sup> curves of these interferometers are available, respectively, at this [link](#) (HLV network) and this [link](#) (ET), and are displayed in Fig. 5.2.

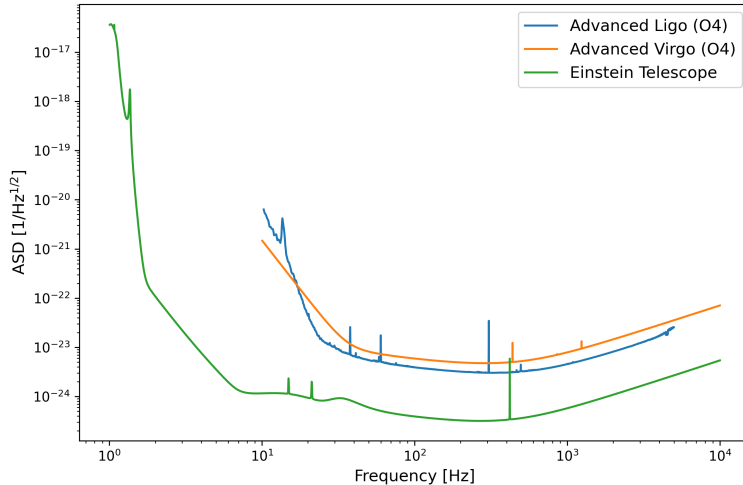


**Figure 5.2.** Expected power spectral densities for Advanced LIGO and Advanced Virgo (O4 run) and the Einstein Telescope.

**Parameter estimation in `bilby`.** After the injection, a subset of the binary parameter posteriors are recovered in `bilby` using `dynesty` (Speagle, 2020), a dynamic nested sampling algorithm, setting the number of live points to 1000. As mentioned in Chapter 4, in a Bayesian framework the posterior of a parameter is evaluated as the ratio between the data’s likelihood, given that parameter, and its prior. Therefore, to obtain the posteriors of the binary parameters one needs to first define the likelihood and prior functions. The likelihood function is evaluated using the `GravitationalWaveTransient` class, whose documentation is available at this [link](#). The priors of the inferred binary parameters were all chosen to be uniform between physically reasonable bounds (see Table 5.1) with the exception of the angular parameters ( $ra$  and  $dec$ ), the inclination of the binary ( $\theta_{jn}$ ) and the polarization angle ( $\psi$ ). The latter were fixed to their injected values, assuming

<sup>5</sup>This assumption, although not being truthful to real GW detections, significantly reduces the computational time related to the parameter estimation.

<sup>6</sup>The ASD is computed as the square-root of the power spectral density (PSD).

for both GW events to have been able to pinpoint the host galaxy thanks to an electromagnetic counterpart. Though this is reasonable for GW170817, the same assumption is less accurate for GW190425. Nevertheless, this assumption significantly reduces the parameter space allowing to cut down the sampling time. Note also that the stellar tidal deformabilities  $\Lambda_1$  and  $\Lambda_2$  were constrained to belong to the interval  $(0, 3000)$ .

The binary parameters retrieved from the injected signal were the chirp mass in the detector-frame<sup>7</sup> ( $\mathcal{M}_{chirp}$ ), the stars dimensionless spins ( $\chi_1$  and  $\chi_2$ ), the symmetric mass ratio ( $\eta$ ), the tidal deformability of the binary ( $\tilde{\Lambda}$ ) and the tidal parameter ( $\delta\tilde{\Lambda}$ ). To further decrease the computational time we decided to marginalize over the luminosity distance, the time and the phase.

	Prior bounds	Units
$\eta$	(0.18, 0.3)	-
$\mathcal{M}_{chirp}$	(1.0, 1.6)	$M_{\odot}$
$\tilde{\Lambda}$	(0, 3000)	-
$\delta\tilde{\Lambda}$	(-1000, 1000)	-
$\chi_1$	(-0.05, 0.05)	-
$\chi_2$	(-0.05, 0.05)	-
$d_L$	(20,400)*	Mpc

**Table 5.1.** Uniform prior bounds for the sampled parameters. The bounds taken for the luminosity distance are marked with \* because the prior function is uniform in comoving volume and source frame time (documentation at the [link](#)).

**Recovering  $\alpha$  posterior.** Our next step was to extract the samples for  $\tilde{\Lambda}$  and  $\eta$  from the output `.json` file in which `bilby` stores all the sampled posteriors. These samples constitute the input files of the Fortran code described in 4.5.2 which implements MCMC sampling on the  $\tilde{\Lambda}$  and  $\eta$  joined posterior to compute the posterior of the parameter  $\alpha$ .

The resulting posteriors obtained for  $\alpha$  for different injection values, different events and detectors are all analysed and discussed in 5.1.3.

**Goal of the analysis.** The goal of the analysis was to compare the performance of current (HLV network) and next-generation (ET) interferometers in recovering the properties of nuclear matter in the NS from the different GW signals. We were particularly interested in determining the improvements introduced by the ET interferometer which is expected to be significantly more sensitive than HLV interferometers (see Fig. 5.2). Although in this work we are limiting ourselves to the study of the inspiral signal, ET is also expected to be more sensitive to frequencies between  $10^3 - 10^4$  Hz, and, therefore, to potentially capture the merger and post-merger GW signals of NS-NS coalescences, opening a window to the study of the last evolutionary phases of the binary and allowing for a better characterization of the tidal effects which become significantly stronger in the late stages of the coalescence (Chatzioannou, 2020).

<sup>7</sup>Ground-based GW detectors actually measure a redshifted (detector-frame) chirp mass which is linked to the real binary chirp mass by the relation  $\mathcal{M}_{chirp}^{det} = (1 + z)\mathcal{M}_{chirp}$ . In the following we will simply refer to the detector-frame chirp mass as  $\mathcal{M}_{chirp}$ .

### 5.1.2 Mock signals parameter estimation

In the following we will describe the results obtained for the parameter estimation analysis conducted on the mock signals of GW170817 and GW190425. For each source we first present the outcome of the Bayesian GW analysis which provides the posterior distributions of the NS-NS binary parameters, focusing afterward on the constraints that can be inferred on the three-nucleon amplitude  $\alpha$ .

**GW170817 mock signal.** The posteriors obtained for GW170817 mock signals are shown in the corner plots in Figs. 5.3 - 5.4 for  $\alpha = 1$  and in Figs. 5.5 - 5.6 for  $\alpha = 1.5$ . Diagonal (off-diagonal) panels show the marginalised (joint 2D) distributions. Note that we also show the samples drawn for the additional parameter  $t_j$ , which refers to a time shift used to produce the time marginalization (Romero-Shaw et al., 2020). The values of the mock signal injected parameters are listed in Tables 5.2 - 5.3 while the reconstructed medians and 68% credible intervals for a subset of the sampled posteriors are shown in Table 5.5 and Table 5.6. As discussed in 2.3.2, since larger values of  $\alpha$  correspond to stiffer EoSs (see Figure 2.5), the injected values of the stellar tidal deformabilities are larger for  $\alpha = 1.5$  than  $\alpha = 1$  (see Table 5.4). However, no significant difference was observed in the performance of the parameter estimation between the two cases.

The SNR of the GW170817 mock signals in LIGO Hanford, LIGO Livingston, LIGO Virgo and ET were, respectively, of 60.58, 50.95, 13.36 and 430.9.

Let us first describe the results obtained for the injections in the HLV network. Among the binary parameters, the chirp mass results to be the one which was the best measured with an uncertainty  $\sim 0.005\%$  at 68% credible interval. This is expected as the chirp mass is the leading quantity which characterizes the evolution of the GW phase (see Section 3.2). On the other hand, the dimensionless spins of the two stars were recovered from the signal with noticeably larger uncertainties being very degenerate between one another. Indeed, the spins do not actually enter the PN expansion individually but as a mass-weighted combination (Cutler & Flanagan, 1994) called *effective spin*<sup>8</sup>

$$\chi_{\text{eff}} = \frac{m_1 \chi_{1z} + m_2 \chi_{2z}}{m_1 + m_2}, \quad (5.3)$$

where  $\chi_{1z}$  and  $\chi_{2z}$  are the spins projections on the axis of the binary angular momentum. This did not represent an issue for our analyses because we were primarily interested in recovering the posteriors of the binary tidal deformability and symmetric mass ratio.

The symmetric mass ratio was the second best measured parameter, with an accuracy of  $\sim 2\%$  at 68 % credible interval (Table 5.5). It presents a partially degenerate behaviour with the spins and the chirp mass since all of them contribute to the 1.5 PN correction to the phase (Cutler & Flanagan, 1994).

As mentioned in 3.2.1, matter effects enter the PN expansion for NS-NS mergers at 5PN ( $\tilde{\Lambda}$  contribute) and 6PN ( $\delta\tilde{\Lambda}$  contribute). Therefore, the tidal parameters represented the most difficult to be recovered from the signal among the binary

<sup>8</sup>Usually  $\chi_{\text{eff}}$  is sampled along with a combination of the spin components perpendicular to the direction of the angular momentum which accounts for precession effects of the binary (Hotokezaka et al., 2013):

$$\chi_p = \max \left( \chi_{\perp,1}, \frac{3+4q}{4+3q} q \chi_{\perp,2} \right). \quad (5.2)$$

parameters. For the mock injections in the HLV network  $\tilde{\Lambda}$  was constrained with an uncertainty of  $\sim 10\%$  at 68 % level while  $\delta\tilde{\Lambda}$  's final posterior was mainly dominated by its prior.

Conversely, the injections in ET showed a noticeable improvement in the parameter estimation of the chirp mass and the binary tidal deformability. The constraints on  $\mathcal{M}_{chirp}$  improved of a factor of  $\sim 2$  when the mock signal was detected by ET (Table 5.5) although still presenting the degeneracy with the spins and the symmetric mass ratio. The measurement of the tidal deformability  $\tilde{\Lambda}$  also improved of a factor  $\sim 2\text{-}3$  assuming the signal was observed by ET. Such enhancement is crucial to accurately recover the the parameter  $\alpha$  , as we will discuss in Sec. 5.1.3.

Similarly to HLV, however, ET failed to set meaningful bounds on  $\delta\tilde{\Lambda}$ . This results is expected given  $\delta\tilde{\Lambda}$  provides a subdominant contribution to the GW phase, entering within its PN expansion as a 6PN correction.

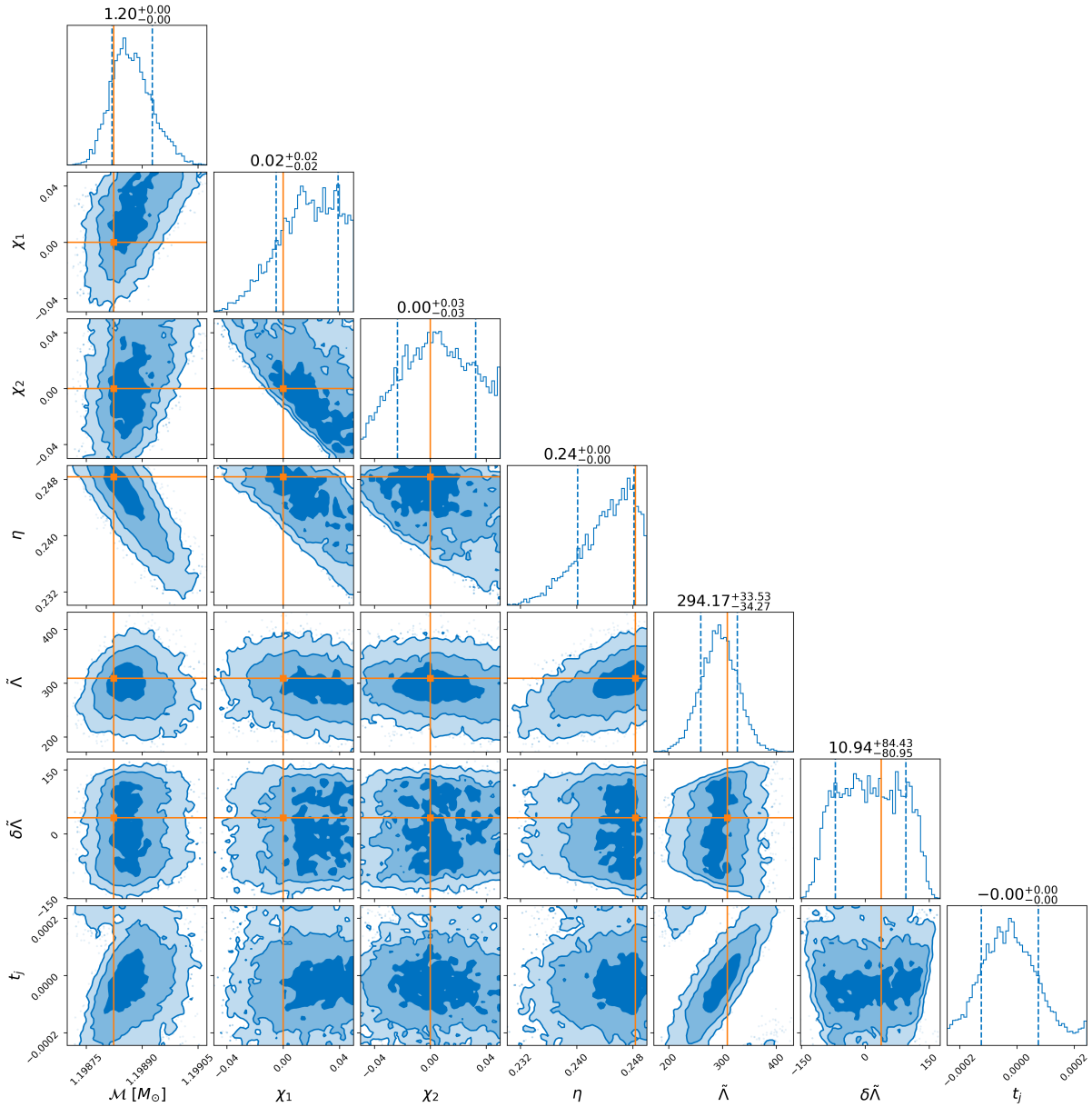


**Figure 5.3.** Corner plot showing the posterior distributions of the sampled binary parameters for GW170817 mock signal observed by the HLV network. We assume  $\alpha = 1$  for the stellar EOS. Solid orange lines correspond to the injected values.

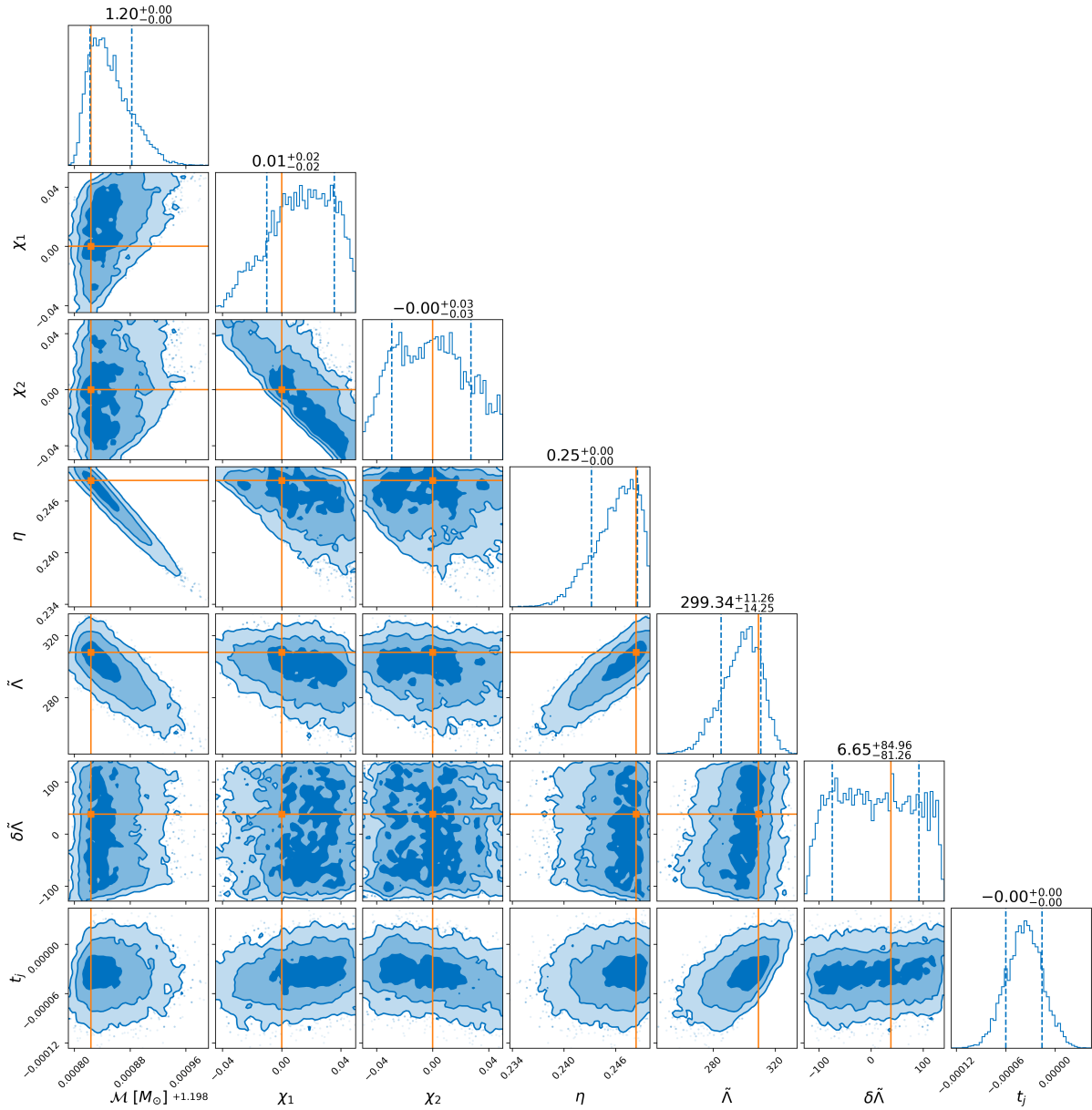


**Figure 5.4.** Same as Fig. 5.3 but for mock signals observed by the Einstein Telescope.

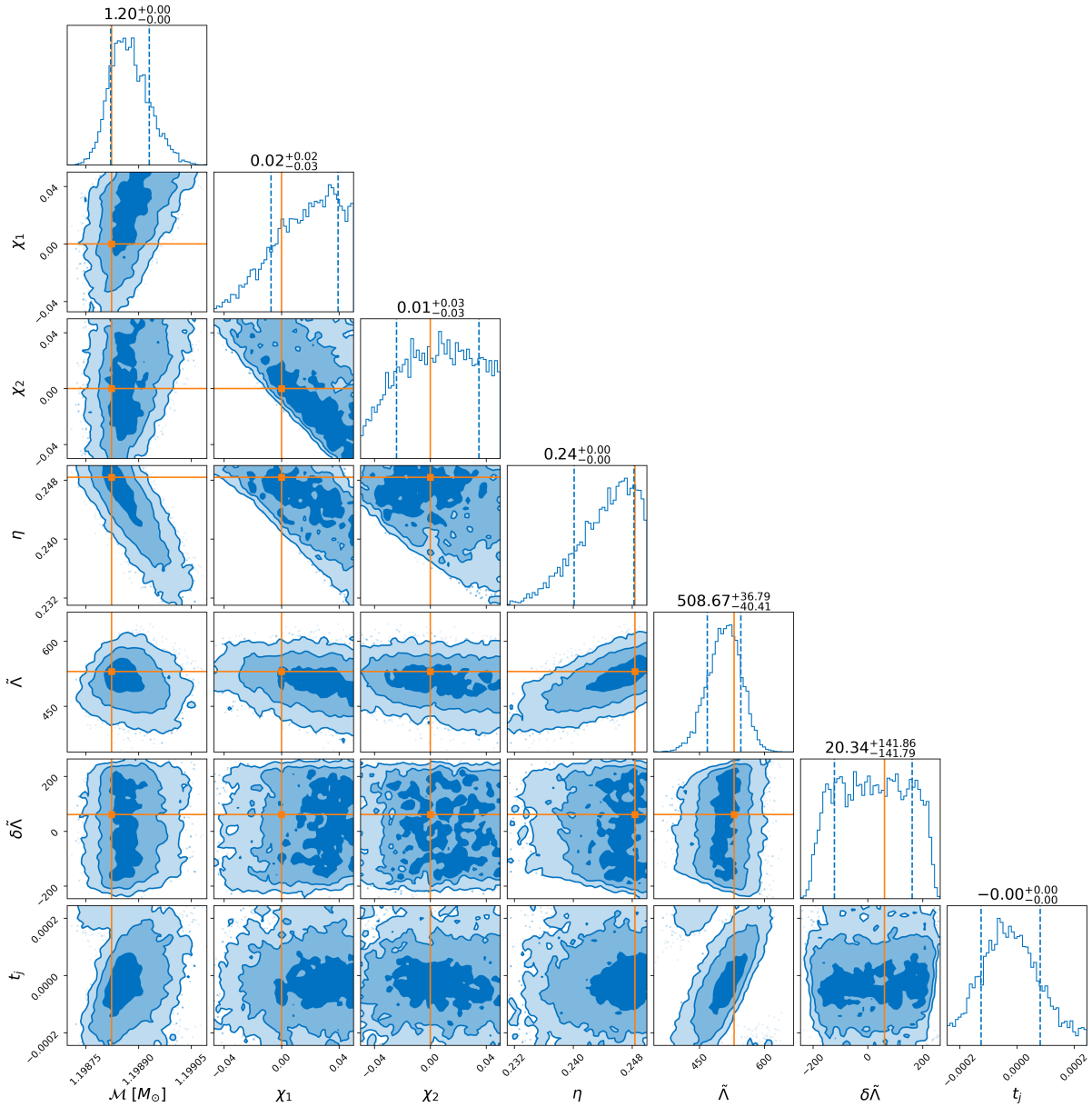


**Figure 5.5.** Corner plot showing the posterior distributions of the sampled binary parameters for GW170817 mock signal observed by the HLV network. We assume  $\alpha = 1.5$  for the stellar EOS. Solid orange lines correspond to the injected values.

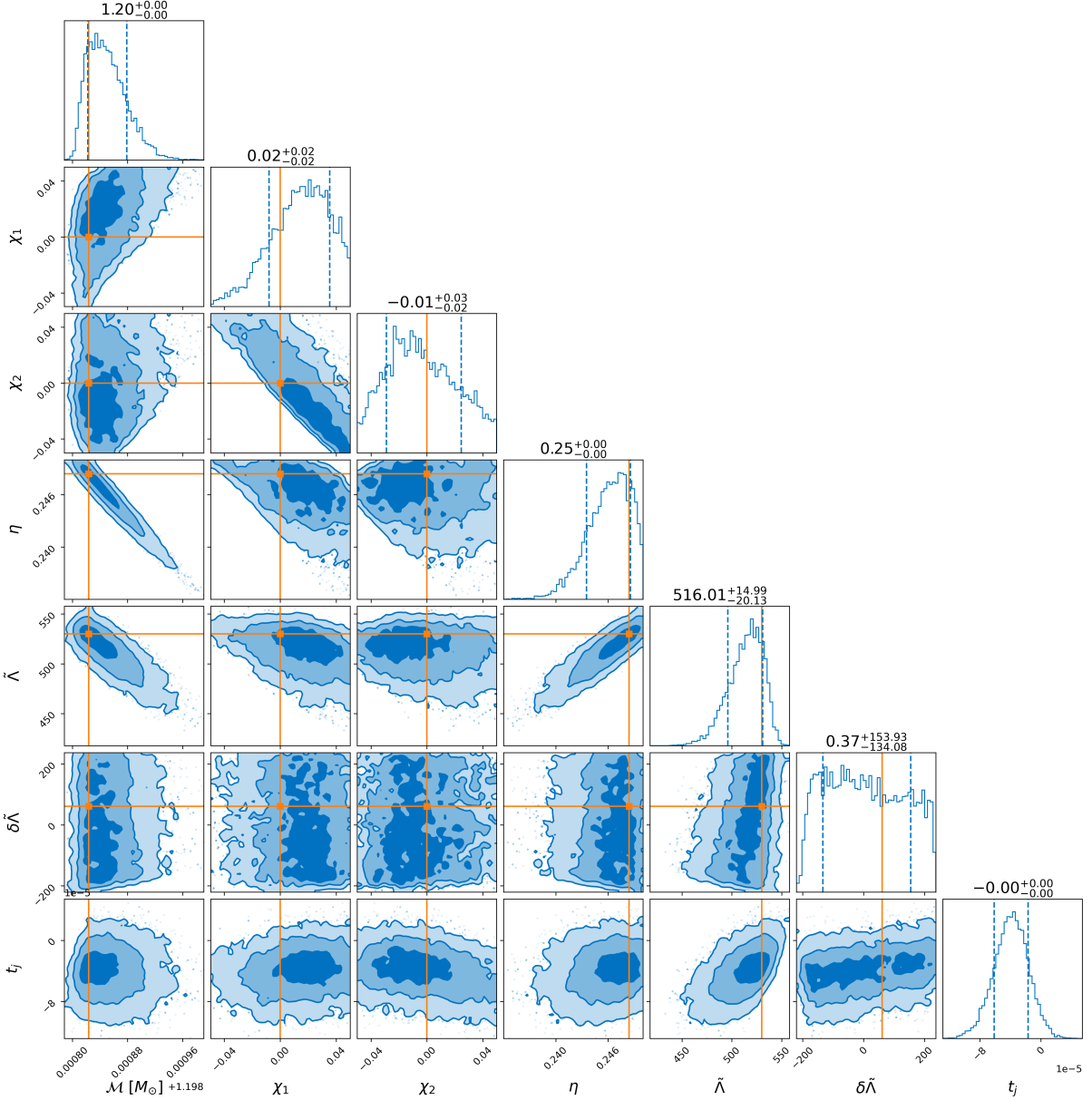


**Figure 5.6.** Same as Fig. 5.5 but for mock signals observed by the Einstein Telescope.

**GW190425 mock signal.** The corner plots obtained for mock signals of the second event GW190425 are shown in Fig. 5.7 and 5.8 for  $\alpha = 1$ , and in Fig. 5.9 and 5.10 for  $\alpha = 1.5$ . The values of the injected parameters are listed in Tables 5.2 - 5.3 while medians and 68% credible interval of the inferred distributions are summarised in Tables 5.5 and Table 5.6. The degeneracies between the binary parameters described in the last paragraph also apply to the case of GW190825. However, both numerical values and corner plots show that the measurements of the binary parameters for GW190425 are less accurate than those obtained for GW170817. This is somehow expected as the injected signals are significantly less loud in this case due to the source luminosity distance, which is four times larger than GW170817.

The SNR of the signals in LIGO Hanford, LIGO Livingston, LIGO Virgo and ET were, respectively, of 7.73, 9.08, 5.28 and 125.3.

When the mock signals are injected in the HLV network the uncertainty on the chirp mass is  $\sim 5$  times larger than the one estimated for GW170817, while the binary tidal deformability and  $\delta\tilde{\Lambda}$  are basically unconstrained.

This picture changes dramatically with the introduction of ET. Indeed, the uncertainty on the chirp mass decreases of a factor 5, from 0.002 % to 0.0004 % at 68% credible interval while the uncertainty on  $\tilde{\Lambda}$  decreases up to the 17 % at 68 % credible interval for both  $\alpha = 1$  and  $\alpha = 1.5$  injection (see Table 5.5 and 5.6). In 5.1.3 we will see how these improvements affect the estimate of  $\alpha$ . As for GW170817's case,  $\delta\tilde{\Lambda}$  is still highly degenerate with most of the other binary parameters, and leads to the loosest constraints overall.

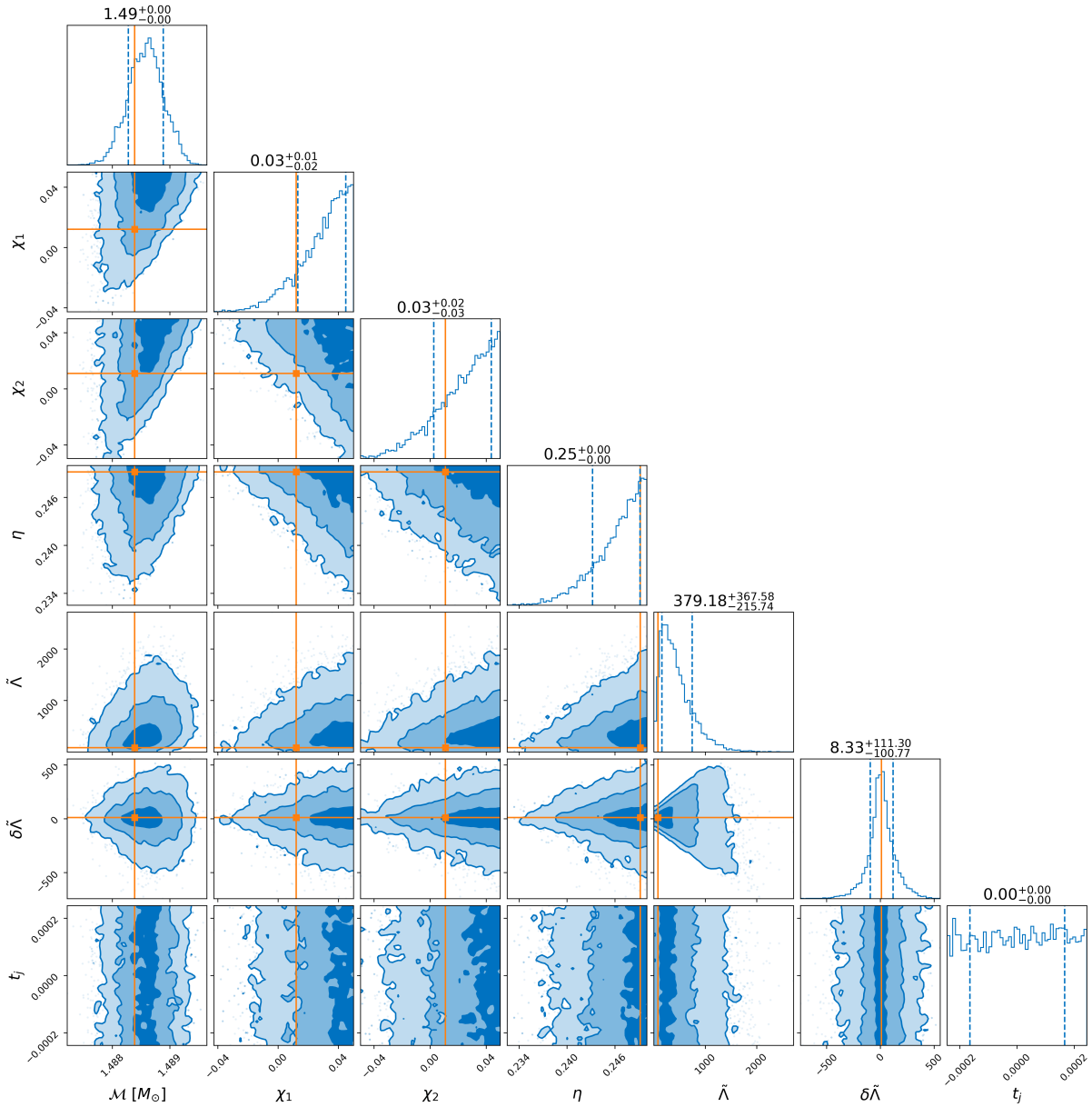


**Figure 5.7.** Corner plot showing the posterior distributions of the sampled binary parameters for GW190425 mock signal observed by the HLV network. We assume  $\alpha = 1$  for the stellar EOS. Solid orange lines correspond to the injected values.

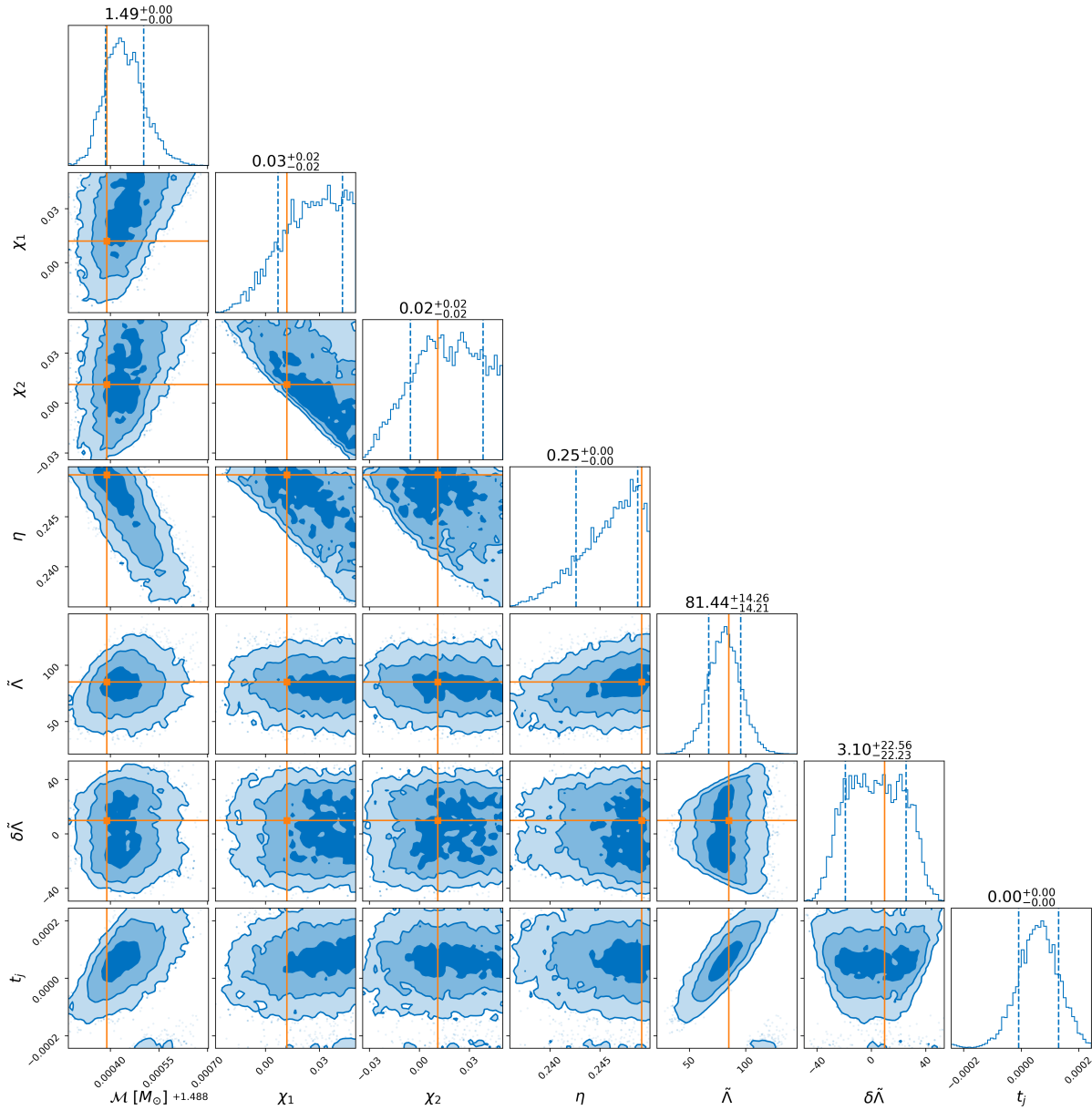


**Figure 5.8.** Same as Fig. 5.7 but for mock signals observed by the Einstein Telescope.

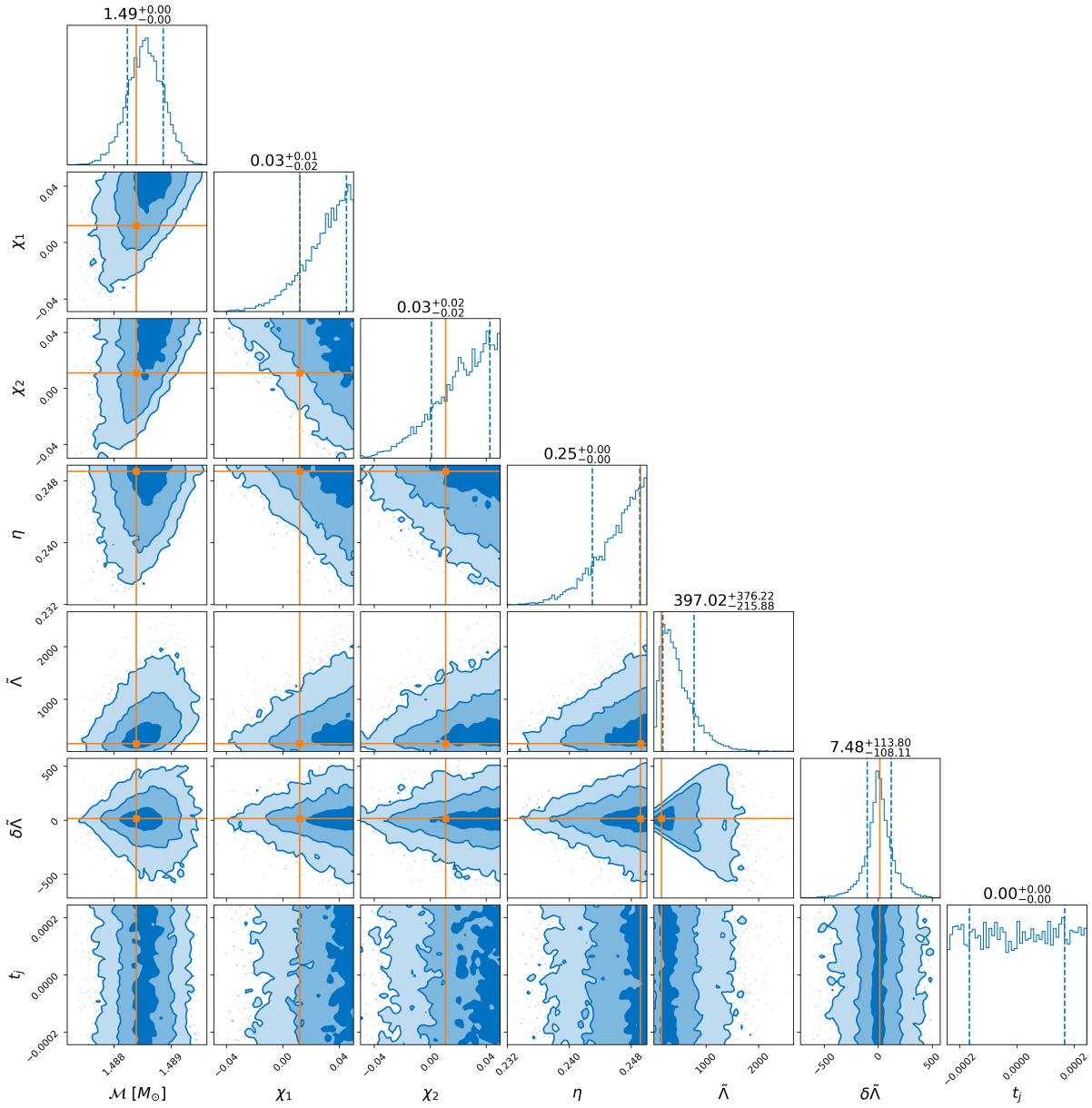


**Figure 5.9.** Corner plot showing the posterior distributions of the sampled binary parameters for GW190425 mock signal observed by the HLV network. We assume  $\alpha = 1.5$  for the stellar EOS. Solid orange lines correspond to the injected values.

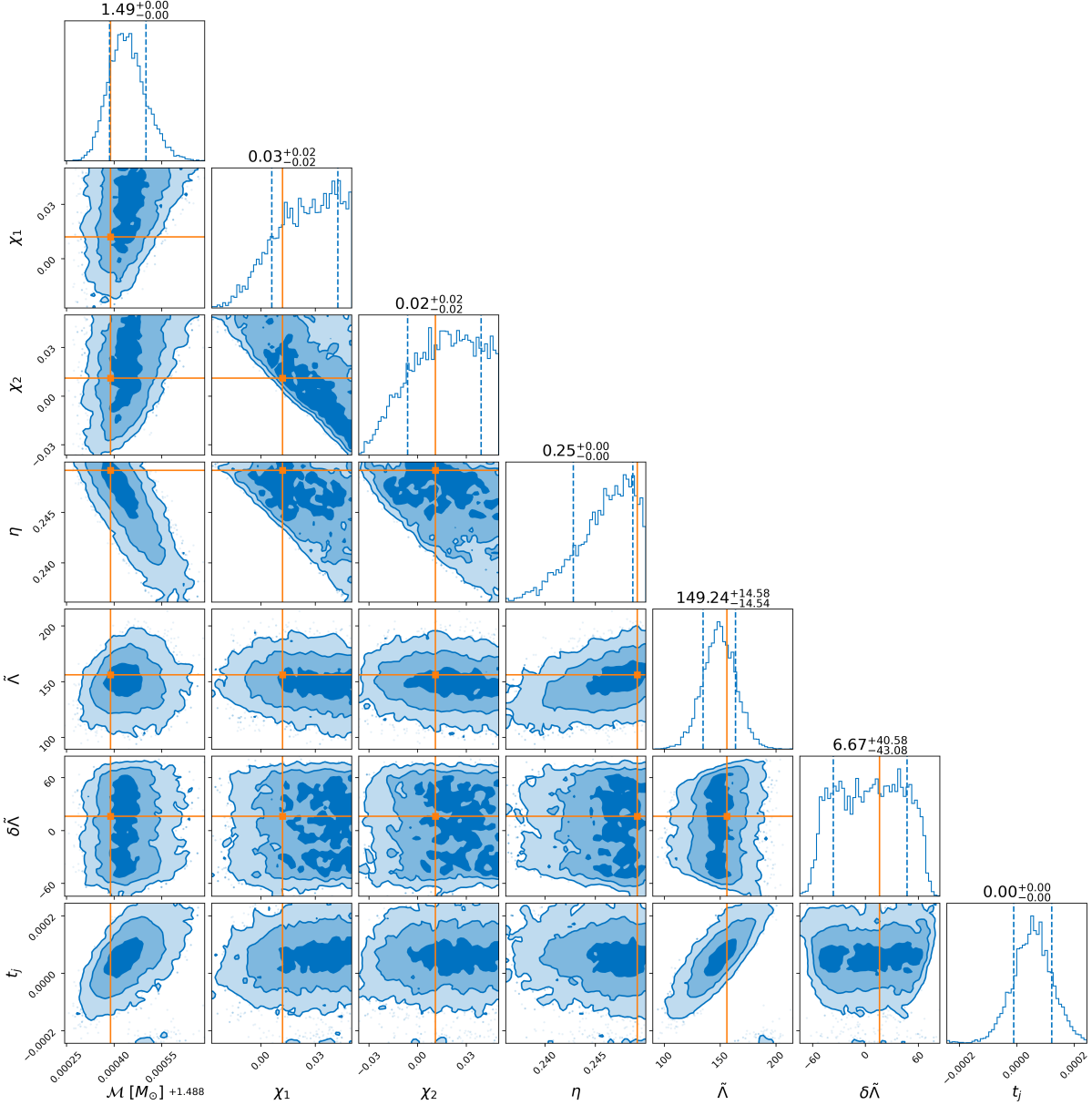


**Figure 5.10.** Same as Fig. 5.9 but for mock signals observed by the Einstein Telescope.

	$m_{1,s} [M_\odot]$	$m_{2,s} [M_\odot]$	$\chi_1$	$\chi_2$	$d_L [\text{Mpc}]$
GW170817	1.48	1.26	0.00	0.00	40
GW190425	1.75	1.56	0.012	0.011	159.5

**Table 5.2.** Injected values of the mass of the stars in the source reference frame ( $m_{1,s}, m_{2,s}$ ), the dimensionless spins ( $\chi_1, \chi_2$ ) and the luminosity distance of the source ( $d_L$ ).

	$\theta_{jn}$ [rad]	ra [rad]	dec [rad]	geoc. time	$\psi$ [rad]	$\phi$ [rad]
GW170817	2.56	3.445	-0.4082	1187008882.43	2.659	1.300
GW190425	1.041	3.681	-0.08228	1240215503.027	1.601	3.106

**Table 5.3.** Injected values for the angular parameters, the geocentric time of the two events, the polarization angle ( $\psi$ ) and the phase of the GW at 50 Hz ( $\phi$ ). Note that the angular parameters are the inclination of the binary ( $\theta_{jn}$ ), the right ascension (ra) and declination (dec) of the source in the sky.

$\alpha = 1$	$\Lambda_1$	$\Lambda_2$	$\tilde{\Lambda}$	$\delta\tilde{\Lambda}$	$\eta$
GW170817	183	505	309	37.28	0.248
GW190425	54	128	85	9.73	0.249
$\alpha = 1.5$	$\Lambda_1$	$\Lambda_2$	$\tilde{\Lambda}$	$\delta\tilde{\Lambda}$	$\eta$
GW170817	321	854	530	60.14	0.248
GW190425	103	229	156	15.88	0.249

**Table 5.4.** Values of the stars tidal deformabilities ( $\Lambda_1$  and  $\Lambda_2$ ), the tidal parameters ( $\tilde{\Lambda}$  and  $\delta\tilde{\Lambda}$ ) and the symmetric mass ratio ( $\eta$ ) for each injection. Note that  $\Lambda_1$  and  $\Lambda_2$  were computed numerically in Fortran from  $m_1$  and  $m_2$  having fixed  $\alpha$  to either 1 or 1.5.

$\alpha = 1$	interf.	$\mathcal{M}_{chirp}$ [ $M_\odot$ ]	$\eta$	$\tilde{\Lambda}$	$\delta\tilde{\Lambda}$	SNR
GW17-	HLV	$1.19887^{+0.00006}_{-0.00005}$	$0.245^{+0.003}_{-0.005}$	$294^{+33}_{-34}$	$11^{+84}_{-80}$	80.3
	ET	$1.19885^{+0.00003}_{-0.00002}$	$0.247^{+0.002}_{-0.003}$	$299^{+11}_{-14}$	$6^{+85}_{-81}$	430.9
GW19-	HLV	$1.4885^{+0.0003}_{-0.0003}$	$0.247^{+0.002}_{-0.004}$	$379^{+368}_{-216}$	$8^{+111}_{-101}$	13.0
	ET	$1.48844^{+0.00006}_{-0.00005}$	$0.246^{+0.002}_{-0.004}$	$81^{+14}_{-14}$	$3^{+22}_{-22}$	125.3

**Table 5.5.** 68% credible intervals around the median values obtained for the chirp mass in the detector reference frame ( $\mathcal{M}_{chirp}$ ) in solar masses, the symmetric mass ratio ( $\eta$ ) and the tidal parameters ( $\tilde{\Lambda}$  and  $\delta\tilde{\Lambda}$ ). The last column shows the total SNR of the event in the interferometers. The medians refer to different events and/or detectors. Note that GW17- and GW19- respectively stand for GW170817 and GW190425.

$\alpha = 1.5$	interf.	$\mathcal{M}_{chirp}$ [ $M_{\odot}$ ]	$\eta$	$\tilde{\Lambda}$	$\delta\tilde{\Lambda}$	SNR
GW17-	HLV	$1.19887^{+0.00006}_{-0.00005}$	$0.245^{+0.003}_{-0.005}$	$509^{+37}_{-40}$	$20^{+141}_{-141}$	80.3
	ET	$1.19885^{+0.00003}_{-0.00002}$	$0.246^{+0.002}_{-0.003}$	$516^{+15}_{-20}$	$0.4^{+153.9}_{-134.1}$	430.9
GW19-	HLV	$1.4885^{+0.00003}_{-0.00003}$	$0.247^{+0.002}_{-0.004}$	$397^{+376}_{-216}$	$7^{+114}_{-108}$	13.0
	ET	$1.48844^{+0.00006}_{-0.00005}$	$0.246^{+0.002}_{-0.003}$	$149^{+15}_{-14}$	$7^{+40}_{-43}$	125.3

**Table 5.6.** 68% credible intervals around the median values obtained for the chirp mass in the detector reference frame ( $\mathcal{M}_{chirp,d}$ ) in solar masses, the symmetric mass ratio ( $\eta$ ) and the tidal parameters ( $\tilde{\Lambda}$  and  $\delta\tilde{\Lambda}$ ). The last column shows the total SNR of the event in the interferometers. The medians refer to different events and/or detectors. Note that GW17- and GW19- respectively stand for GW170817 and GW190425.

### 5.1.3 Retrieving $\alpha$

Having obtained the sampled posteriors of the binary parameters we move to recovering the distribution of  $\alpha$ . This is done by following the procedure presented in Section 4.5 in which the posterior distribution of  $\alpha$  is obtained from the joint distribution of the binary tidal deformability  $\tilde{\Lambda}$  and the symmetric mass ratio  $\eta$ . The latter are extracted from `bilby` output `.json` file which contains the samples of the various parameters posteriors.

The inferred marginal posteriors are shown in Figs. 5.11 and 5.12 for the HLV network and ET, respectively. Furthermore, in Fig. 5.13 and in Fig. 5.14 we show the 2D contour plots of the posterior distributions of  $\alpha$  and  $\log_{10} p_c$ , for the injections of GW170817 and GW190425 mock signals. Note that the (logarithm of the) central pressure  $p_c$  is expressed in dyne/cm<sup>2</sup>. It is interesting to notice that the posteriors of  $p_c$  present a double peak in correspondence of the injected central pressures of the primary NS (red star) and secondary star (orange star). This is related to the fact that we are sampling  $\tilde{\Lambda}$  alongside the symmetric mass ratio  $\eta$  which, conversely to the mass ratio  $q$ , is completely symmetric under an exchange of the two stellar masses.

As expected from the results obtained in 5.1.2, the detections of GW170817 put, overall, the most accurate constraints on the injected value of  $\alpha$ . More specifically, the values of  $\alpha$  recovered from the injections in the HLV network present an uncertainty at the 68% credible interval of  $\sim 10\%$  which decreases up to a  $\sim 3\text{-}4\%$  when injected in ET (Table 5.7). Even more interestingly, while injections of GW190824 in the HLV network fail to accurately constrain the value of  $\alpha$ , when the mock signals are injected in ET we are able to recover  $\alpha$  with an uncertainty of  $\sim 10\%$  at 68% credible interval.

These results, along with the ones obtained in 5.1.2, highlight the significant impact of third generation interferometers in constraining finite-size effects such as tidal corrections to the GW phase, and their accuracy in recovering nuclear properties of matter inside NSs linked to the still uncertain NS EoS.

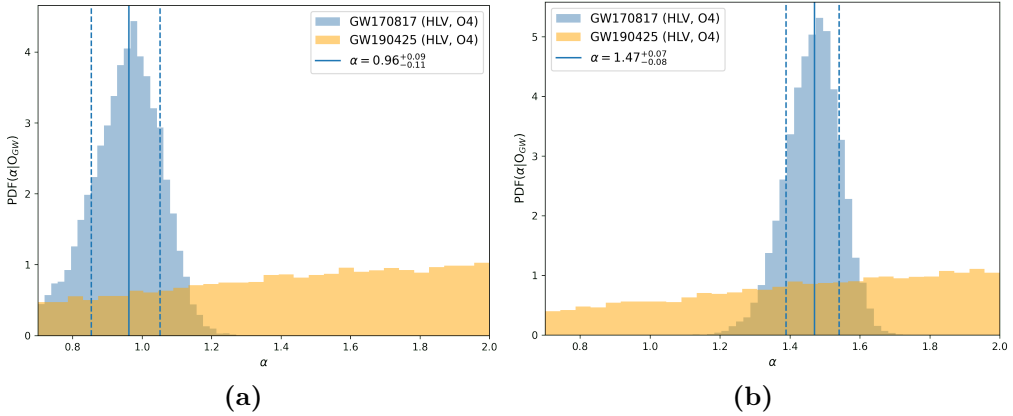


**Figure 5.11.** Posterior distributions retrieved for  $\alpha$ . Note that Figure 5.11a and Figure 5.11b refer, respectively, to the injection of GW170817 and GW190425 signals in the HLV network.

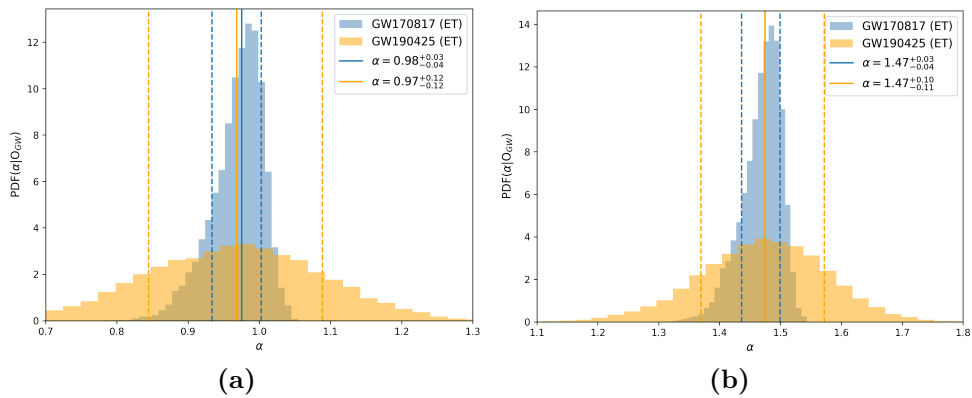


**Figure 5.12.** Same as Fig. 5.11 but for signals injected in the Einstein Telescope noise stream.

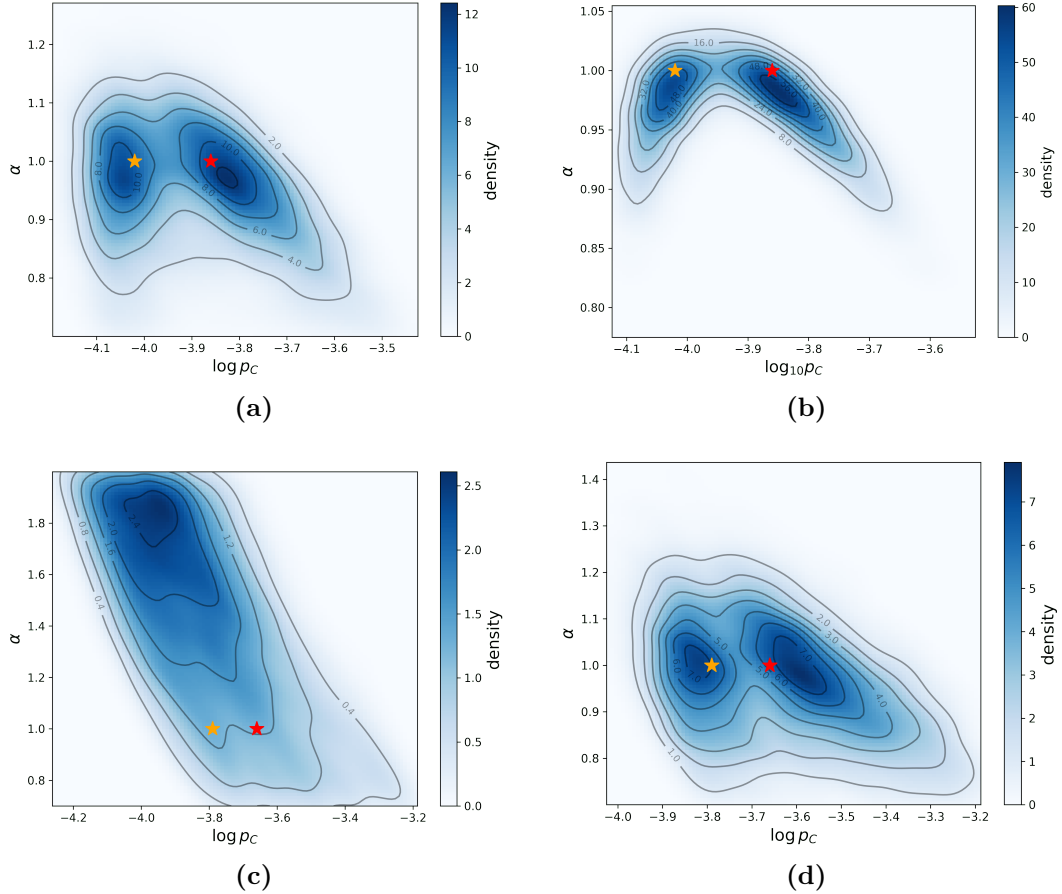


**Figure 5.13.** Contour plots of the 2D posteriors of  $\alpha$  and  $p_c$  for different observations and/or detectors assuming an injected value  $\alpha = 1$ . The top row panels present the 2D distributions obtained for injection of GW170817 in the HLV network (left panel) and in ET (right panel) while the bottom row panels the injections of GW190425 in the same order. The red and orange stars denote, respectively the injected values of  $\alpha$  and  $\log_{10} p_c$  for the primary and the secondary star in the binary.

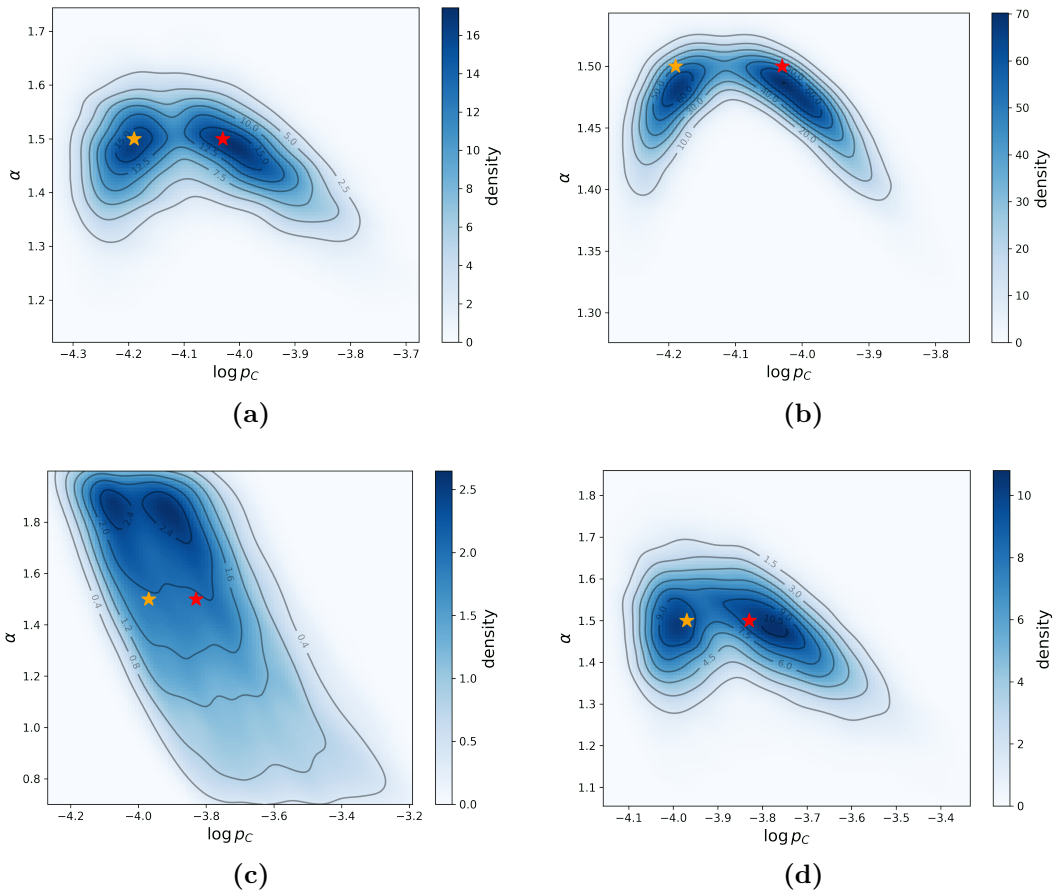


**Figure 5.14.** Same as Fig. 5.13 but assuming NS binaries with  $\alpha = 1.5$ .

$\alpha = 1$	interf.	median
GW170817	HLV	$0.98^{+0.09}_{-0.11}$
	ET	$0.98^{+0.03}_{-0.04}$
GW190425	HLV	-
	ET	$0.97^{+0.12}_{-0.12}$
$\alpha = 1.5$	interf.	median
GW170817	HLV	$1.47^{+0.07}_{-0.08}$
	ET	$1.47^{+0.03}_{-0.04}$
GW190425	HLV	-
	ET	$1.47^{+0.10}_{-0.11}$

**Table 5.7.** 68 % credible intervals around the medians obtained from the  $\alpha$  posteriors in Fig. 5.11 and Fig. 5.12.

## 5.2 AT2017gfo

As previously mentioned, GW170817 represented a unique event for multimesenger astronomy since it was followed not only by a short-gamma ray burst but also by a quasi-isotropic electromagnetic transient which was never been observed at the time, a kilonova (AT2017gfo). This transient was firstly detected in the optical band by the Swope telescope on August 17 at 23:33 UTC, about 10.87 h after the GW trigger (Abbott et al., 2017a). Over the course of a couple of days, the kilonova showed a rapid dimming of its initial UV–blue emission and an unusual brightening of the near-infrared emission. After roughly a week, the redder optical and near-infrared bands began to fade as well (Abbott et al., 2017a). In Fig. 5.15 is presented the evolution of the kilonova luminosity over a period of 30 days in the UV-optical-infrared (UVOIR) bands.

As seen in Section 3.3, the kilonova is powered by the radioactive decay of neutron rich matter expelled during and after the merger by a variety of mechanisms which produce ejecta with different masses, velocities and compositions. These fundamental properties of the ejecta are, ultimately, dependent on the properties of the progenitor NSs such as their mass, tidal deformability and EoS. For this reason, many studies are now conducted to assess the relation between kilonovae features and the binary properties and implement efficient inference strategies to retrieve the latter from the signal and combine it with the information coming from GWs (i.g. Radice et al. (2018), Raaijmakers et al. (2021), Pang et al. (2021)).

In this Section we will follow the analysis of Breschi et al. (2021) and derive the posterior distribution of the binary tidal deformability ( $\tilde{\Lambda}$ ) and mass ratio ( $q$ ) from the distribution of the dynamical ejecta mass ( $m_{ej}^D$ ) and velocity ( $v_{ej}^D$ ), the latter being inferred in Breschi et al. (2021) by fitting the photometric data of AT2017gfo with an anisotropic multicomponent ejecta model. Next, following the procedure described in Section 4.5, we will obtain the posterior distribution of  $\alpha$  from the joint posterior of  $\tilde{\Lambda}$  and  $\eta$ .

The numerical pipeline used to perform the analysis is described in 5.2.1. The former is first applied to the case of AT2017gfo in 5.2.2, then a possible generalization to mock kilonova signals is explored in 5.2.3.

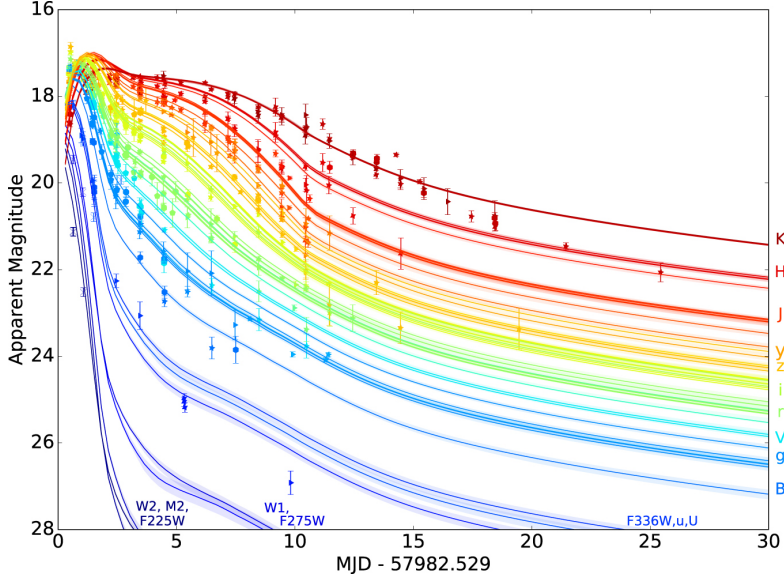


**Figure 5.15.** UVOIR luminosity time-evolution of AT2017gfo presented in Villar et al. (2017). Solid lines represent the predictions of the highest likelihood three-component model for each filter, while shaded regions represent the  $1\sigma$  uncertainty ranges.

### 5.2.1 Code overview

The structure of the numerical pipeline implemented to estimate  $\alpha$  from the photometric data of AT2017gfo is displayed in Fig. 5.17.

The starting point of the pipeline (blue box in Fig. 5.17) is represented by the  $m_{ej}^D$  and  $v_{ej}^D$  posterior distributions obtained by Breschi et al. (2021) from the fit of AT2017gfo photometric data with an anisotropic 3-component model<sup>9</sup> (Fig. 5.16). The components considered by Breschi et al. (2021) in their model are a dynamical ejecta, a viscous ejecta and neutrino wind ejecta which we briefly reviewed in 3.3.3. For simplicity, we will assume  $m_{ej}^D$  and  $v_{ej}^D$  posteriors to be normal distributions around the means reported in Table 3 of Breschi et al. (2021) with standard deviations obtained from the mean of 90 % credible intervals also reported in Table 3.

**Resampling.** We follow the resampling procedure described in Breschi et al. (2021) (green boxes in Fig. 5.17): first a tuple  $(q, \tilde{\Lambda})$  is drawn from their priors, secondly the tuple is mapped into  $(m_{ej}^{ej}, v_{ej}^{ej})$  exploiting the NR fitted formula derived by Nedora et al. (2021):

$$P_2(q, \tilde{\Lambda}) = b_0 + b_1 q + b_2 \tilde{\Lambda} + b_3 q^2 + b_4 q \tilde{\Lambda} + b_5 \tilde{\Lambda}^2 , \quad (5.4)$$

<sup>9</sup>In the first part of the paper the authors prove that this model provides the larger evidence among the others tested which either presented less components and/or an isotropic geometry.

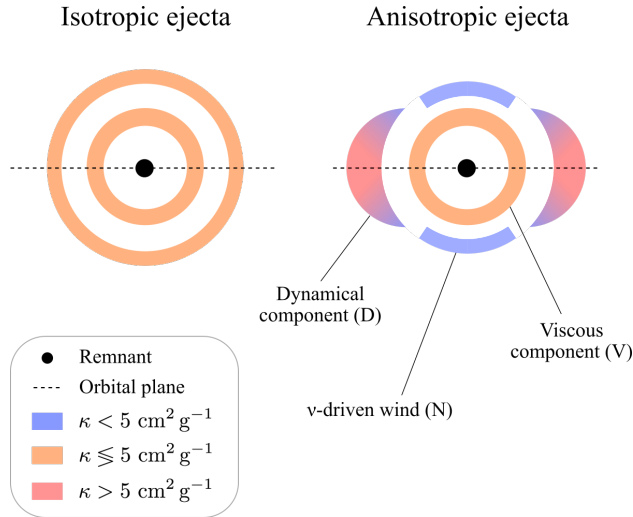


**Figure 5.16.** Profiles of the various ejecta models analysed in Breschi et al. (2021) from an azimuthal perspective and for a fixed moment of time.

with the coefficients of the polynomial being listed in Table 5.8. Lastly the log-posterior of  $(q, \tilde{\Lambda})$  is evaluated as:

$$\log \mathcal{P}(q, \tilde{\Lambda} | d_{ATgfo}) = \frac{1}{2} \left[ \frac{(m_{ej}^D - \tilde{m}_{ej}^D)^2}{\sigma_m^2} + \frac{(v_{ej}^D - \tilde{v}_{ej}^D)^2}{\sigma_v^2} + \frac{a_1^2}{\sigma_a^2} + \frac{a_2^2}{\sigma_a^2} \right] + C . \quad (5.5)$$

Note that  $\tilde{m}_{ej}^D$ ,  $\tilde{v}_{ej}^D$  and  $\sigma_m$ ,  $\sigma_v$  in Eq. (5.5) are the means and standard deviations of the dynamical ejecta mass and velocity posterior distributions.

**Calibration parameters.** To take into account the non-negligible uncertainties related to the NR fit, two calibration factors are introduced (Breschi et al., 2021) such that:

$$\log_{10} m_{ej}^D = (1 + a_1) \log_{10} m_{ej,\text{fit}}^D ; \quad v_{ej}^D = (1 + a_2) v_{ej,\text{fit}}^D . \quad (5.6)$$

The calibration parameters are sampled along with the other parameters assuming they are described by gaussian priors with vanishing means and standard deviations  $\sigma_a = 0.2$  (relative uncertainties of the NR fit). These priors also contribute to the final posterior of  $(q, \tilde{\Lambda})$  (see Eq. (5.5)).

**Sampler.** The sampling of the parameter space was performed in Python using the `emcee` sampler (Foreman-Mackey et al., 2013). The number of walkers was fixed to 50 while the number of steps-per-walker has been fixed to be 800000 steps, 200000 of which are discarded as burn-in.

**Obtaining  $\alpha$  posterior.** At the end of the sampling procedure we obtain the posterior samples of  $q$ ,  $\tilde{\Lambda}$ ,  $a_1$  and  $a_2$ . From the mass ratio samples we can get the samples of the symmetric mass ratio  $\eta$  exploiting the relation:

$$\eta = \frac{q}{(1+q)^2} . \quad (5.7)$$

Next, having the posterior samples of  $\tilde{\Lambda}$  and  $\eta$ , we can follow the same procedure described in 4.5 and produce the posterior distribution of the 3-nucleon repulsive strength,  $\alpha$ .

**Goal of the analysis.** In this Section our goal was to explore the constraints posed by the kilonova emission on the nuclear properties of NSs and define a generalization of the pipeline defined for the injection campaign in Section 5.1. Furthermore, this analysis sets the stage for the multimessenger data-analysis strategy we have developed in Section 5.3 where the results obtained from the inspiral signals are combined with the ones obtained from the kilonova emission.

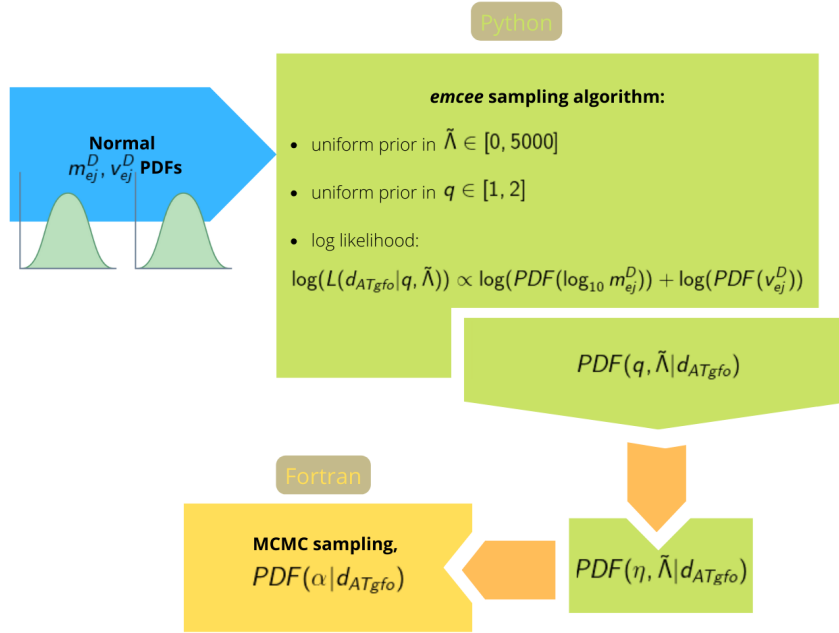


**Figure 5.17.** Flow chart of the numerical pipeline defined to hierarchically infer the amplitude of 3-nucleon forces from from the photometric data of AT2017gfo.

	$\log_{10} m_{ej}^D$	$v_{ej}^D$ [c]
b <sub>0</sub>	1.04	0.720
b <sub>1</sub>	-3.31	-0.204
b <sub>2</sub>	$-6.89 \cdot 10^{-3}$	$-1.20 \cdot 10^{-3}$
b <sub>3</sub>	0.4194	$-4.05 \cdot 10^{-2}$
b <sub>4</sub>	$5.09 \cdot 10^{-3}$	$3.92 \cdot 10^{-4}$
b <sub>5</sub>	$5.83 \cdot 10^{-7}$	$5.20 \cdot 10^{-7}$

**Table 5.8.** Coefficients of the polynomial fit in Eq. (5.4) (Nedora et al., 2021).

### 5.2.2 Real data

We first repeated the analysis in [Breschi et al. \(2021\)](#) to assess the effect of the approximations introduced and produce the posterior of  $\alpha$ . Similarly to [Breschi et al. \(2021\)](#) the obtained posterior for  $\tilde{\Lambda}$  is characterized by two modes approximately at 300 and 1000 (see Fig. 5.18a). Note that the presence of these double peaks is to be attributed to the quadratic nature of the fitted formula of [Nedora et al. \(2021\)](#). The position of the modes was evaluated by fitting the posterior samples of  $\tilde{\Lambda}$  in Python as a sum of two gaussian distributions. The values obtained for the modes and the standard deviations are respectively  $\tilde{\Lambda}_1 = 299^{+152}_{-152}$  and  $\tilde{\Lambda}_2 = 996^{+124}_{-124}$ . The median of the distribution is  $\tilde{\Lambda} = 931^{+170}_{-615}$  (68 % credible interval), compatible with the result obtained by [Breschi et al. \(2021\)](#) of  $\tilde{\Lambda} = 900^{+310}_{-780}$ . Furthermore, the mass ratio is constrained to be  $< 1.56$  at the 90% credible interval similar to [Breschi et al. \(2021\)](#) ( $q < 1.54$  at the 90% level), while the median of the distribution is  $q = 1.32^{+0.16}_{-0.20}$  (68 % credible interval).

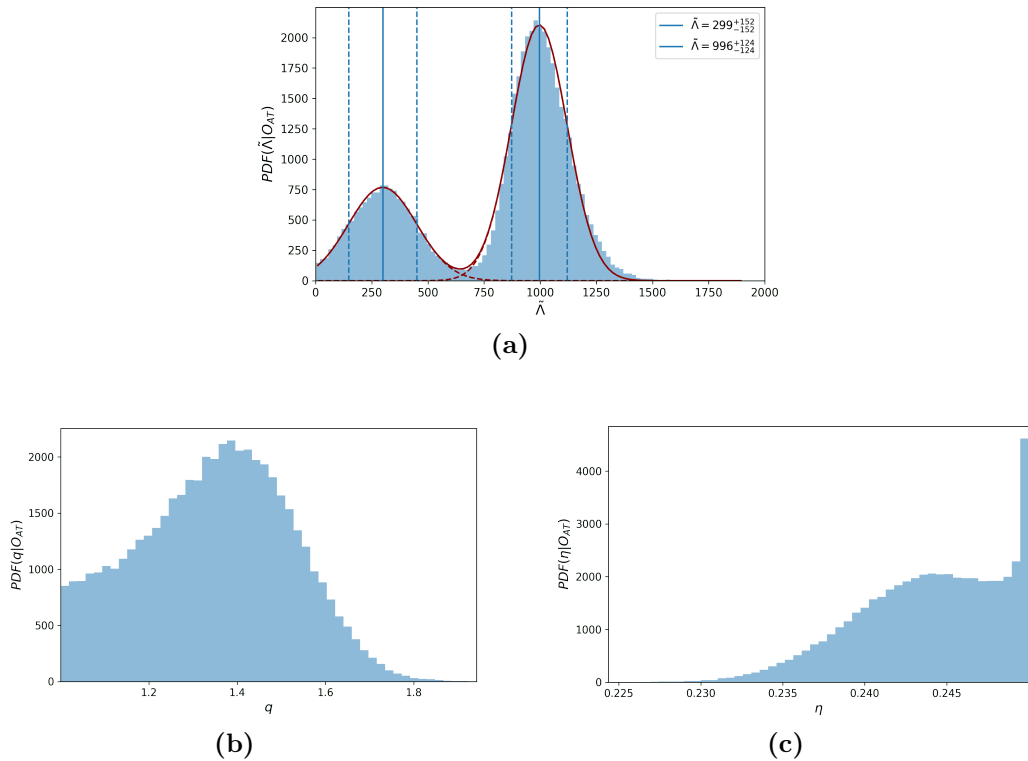


Figure 5.18

**Figure 5.19.** Posterior distributions (not normalized) of the binary tidal deformability  $\tilde{\Lambda}$ , the mass ratio  $q$  and the symmetric mass ratio  $\eta$  obtained from the distributions of  $m_{ej}^D$  and  $v_{ej}^D$  for the case of AT2017gfo. The samples obtained for  $\tilde{\Lambda}$  can be accurately fitted with a double gaussian (red curve in the top panel). Furthermore, the blue vertical lines in Fig. 5.18a denote the modes of the fitted double gaussian (solid line) and the  $\pm 1\sigma$  region (dashed).

From the mass ratio samples we obtain the samples for the symmetric mass ratio exploiting Eq. 5.7 (Fig. 5.18c). Next, following the procedure outlined in Section 4.5,

we get the distribution of  $\alpha$ . The latter is displayed in Fig. 5.20. The distribution presents a median value of  $\alpha = 1.14^{+0.32}_{-0.26}$  (uncertainty of  $\sim 30\%$  at 68 % credible interval). Note that our baseline model, which is obtained for  $\alpha = 1$  (see 2.3.2), is compatible within the 68% credible interval with the median of the distribution. On the other hand, more stiff scenarios (as the one explored for the mock GW analysis, i.e.  $\alpha = 1.5$ ) result slightly outside of the 68% interval and, thus, are less probable. As a matter of fact, the obtained distribution tends to exclude the larger values of  $\alpha$ , being  $\alpha \lesssim 1.57$  at 90% level.

In Section 5.3 we will see how these results, combined to the distribution recovered from GW170817 strain data, contribute to a multimessenger estimate of the  $\alpha$ .

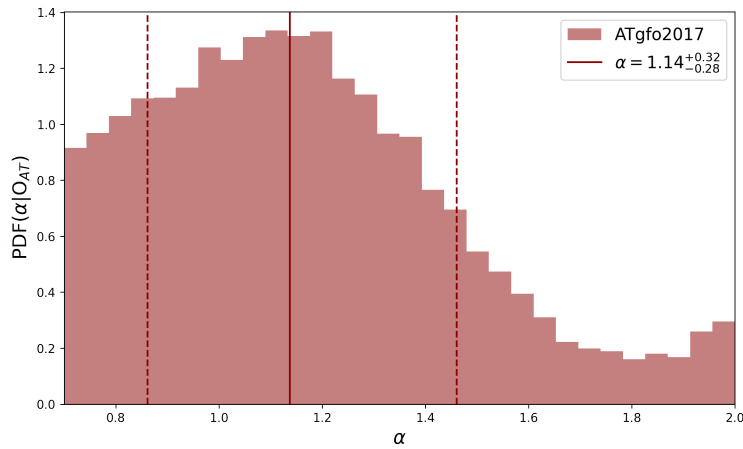


**Figure 5.20.** Posterior distribution of  $\alpha$  obtained from the analysis of AT2017gfo's photometric data. The vertical red lines denote the position of the median (solid) and the 68 % interval.

### 5.2.3 Mock data

In the following we produce a similar analysis to the one in 5.2.2 but we fix the value of  $\alpha$  a-priori to assess to which accuracy the parameter is retrieved. More specifically we study the case of NS mergers with the masses and tidal deformabilities used in Section 5.1 for GW170817 and GW190425 mock signals.

From  $m_1, m_2, \Lambda_1, \Lambda_2$  we compute the mass ratio  $q$  and binary tidal deformability  $\tilde{\Lambda}$  and, subsequently, the expected  $\log_{10}m_{ej}^D$  and  $v_{ej}^D$  exploiting Eq. (5.4), i.e. assuming the mock NS-NS mergers to have produced a kilonova emission. In this sense, the values obtained for  $m_{ej}^D = 10^{\log_{10}m_{ej}^D}$  and  $v_{ej}^D$  are considered to be the means of the normal posterior distributions which would have been produced through an hypothetical fit of the kilonovae photometric data such as in Breschi et al. (2021). The standard deviations of the mass and velocity normal distributions are chosen to be, respectively, the 5% and 1% of the means, roughly in the same proportion as the medians of  $m_{ej}^D$  and  $v_{ej}^D$  and their uncertainties chosen in 5.2.2.

The analysis is conducted for the two events fixing either  $\alpha = 1$  or  $\alpha = 1.5$ . The resulting posteriors are displayed in Fig. 5.21 while the medians and 68% credible intervals are presented in Table 5.9.

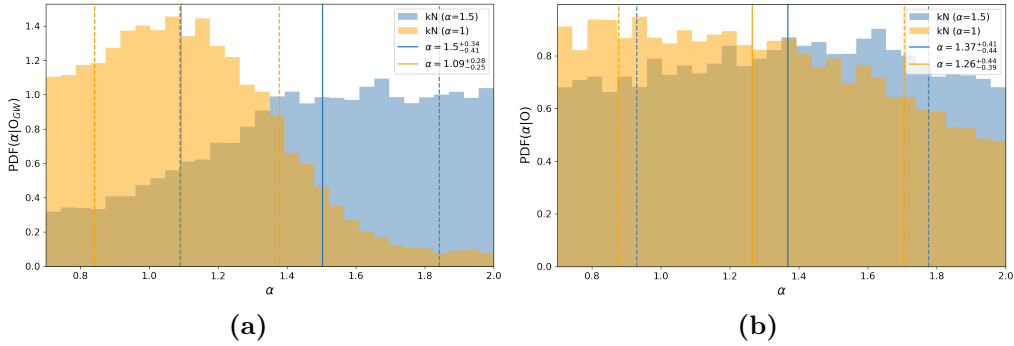


**Figure 5.21.** Posterior distributions of  $\alpha$  obtained for kilonova mock signals of GW170817 (Fig. 5.21a) and GW190425 (Fig. 5.21b). The histograms in yellow refer to the injections  $\alpha = 1$ , while the blue histograms refer to the injections  $\alpha = 1.5$ . The vertical lines denote the position of the medians (solid) and the 68% credible intervals (dashed)

Comparing the posteriors obtained for GW170817 and GW190425 we can observe that there is a significant worsening in the accuracy to which we retrieve  $\alpha$  for the second event. This could be explained by the fact that the fitted formula in Nedora et al. (2021) (Eq. (5.4)) was obtained studying mergers with fixed detector-frame chirp mass  $\mathcal{M}_{\text{chirp}} = 1.188 M_{\odot}$ , i.e. the estimated chirp mass of the event GW170817, implying that the formula might not apply to the case of GW190425. Moreover, there is a noticeable difference between the injection  $\alpha = 1$  and  $\alpha = 1.5$  for the case of GW170817 simulated kilonovae. Indeed, the posterior obtained for the  $\alpha = 1.5$  injection (blue histogram in Fig. 5.21a), rather than showing a peak, presents a flat ending for  $\alpha \gtrsim 1.4$ . We think this is justified by the fact that the spurious peak, i.e. the peak that does not correspond to the injected value of  $\tilde{\Lambda}$ , is very close to the other peak for  $\alpha = 1.5$  (see Fig. 5.22a, right panel). Therefore, the samples from both peaks populate similar ranges of values around the injected value ( $\alpha = 1.5$ ). In particular, the peak corresponding to larger tidal deformabilities, contribute to the values of  $\alpha$  around the upper bound of the prior, i.e.  $\alpha = 2$ .

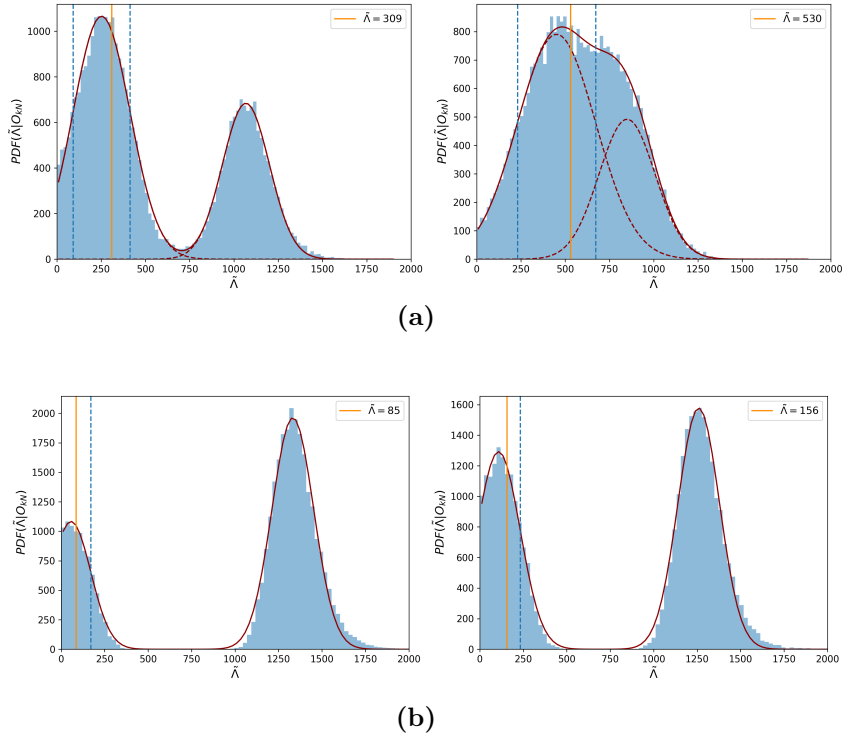


**Figure 5.22.** Posterior distributions (not normalized) of  $\tilde{\Lambda}$  obtained for kilonova mock signals of GW170817 (Fig. 5.22a) and GW190425 (Fig. 5.22b). The histograms on the left side refer to the injections  $\alpha = 1$ , while the ones on the right side refer to the injections  $\alpha = 1.5$ . The positions of  $\tilde{\Lambda}$ 's injected value is denoted by the orange vertical lines while in red are shown the double gaussians fitted to the samples. Finally, the dashed blue lines denote the  $\pm 1\sigma$  regions of the first peak of the fitted double gaussian.

	median
$\alpha = 1$	
GW17- kN	$1.09^{+0.24}_{-0.25}$
GW19- kN	$1.26^{+0.44}_{-0.39}$
$\alpha = 1.5$	median
GW17- kN	$1.50^{+0.34}_{-0.41}$
GW19- kN	$1.37^{+0.41}_{-0.44}$

**Table 5.9.** 68% credible intervals around the median values of the  $\alpha$ 's posteriors obtained for GW170817 mock kilonova (GW17- kN) and GW190425 mock kilonova (GW19- kN).

### 5.3 Multimessenger analysis of GW170817 and AT2017gfo

For the final part of the analysis we combine the estimated distributions of  $\eta$  and  $\tilde{\Lambda}$  retrieved from the photometric data of AT2017gfo and from the GW strain

data of GW170817 to obtain a multimessenger estimate of  $\alpha$ . This is achieved, in the same fashion as Section 5.2, first for real data and then for mock signals. The code used to obtain  $\alpha$  distribution is the one described in Section 4.5 where the total log-likelihood expression is modified to take into account both the contribution of the kilonova and the GW data:

$$\log(\mathcal{L}(d_{AT17}, d_{GW17} | \tilde{\Lambda}, \eta)) = \log(\mathcal{L}(d_{AT17} | \tilde{\Lambda}, \eta)) + \log(\mathcal{L}(d_{GW17} | \tilde{\Lambda}, \eta)), \quad (5.8)$$

where  $\log(\mathcal{L}(d_{AT17} | \tilde{\Lambda}, \eta))$  and  $\log(\mathcal{L}(d_{GW17} | \tilde{\Lambda}, \eta))$  are the likelihood of the kilonova data and the GW strain data given  $\tilde{\Lambda}$  and  $\eta$ .

### 5.3.1 Real data

**Note on the likelihood evaluation.** The likelihood used for GW170817 strain data correspond to the one used in [Sabatucci et al. \(2022\)](#), which is obtained as

$$\mathcal{L}(d_{GW17} | \tilde{\Lambda}, \eta) = \frac{P(\tilde{\Lambda}, \eta | d_{GW17})}{P_0(\tilde{\Lambda}, \eta)}, \quad (5.9)$$

where  $P(\tilde{\Lambda}, \eta | d_{GW17})$  and  $P_0(\tilde{\Lambda}, \eta)$  are, respectively, the posterior and prior of  $\tilde{\Lambda}$  and  $\eta$  reported in [Abbott et al. \(2019\)](#). Note that in the analyses conducted in the previous Sections we used the posterior and the likelihood interchangeably since we always chose  $\tilde{\Lambda}$  and  $\eta$  priors to be uniform, i.e. they only differed up to a negligible multiplying constant. However, in this case, since the priors used in [Abbott et al. \(2019\)](#) are not uniform we need to properly re-weight the posterior to obtain the likelihood. On the other hand, in the case of AT2017gfo following the argument on the flat priors, we evaluate the likelihoods directly from the posteriors obtained in 5.2.2.

The resulting multimessenger distribution of  $\alpha$  is displayed in Fig. 5.23 in pink, superimposed on the distributions obtained for the analyses of GW170817 and AT2017gfo data alone, respectively in blue and red. Overall, the multimessenger distribution is dominated by the contribution of GW170817 which pushes the posterior against the lower prior bound at  $\alpha = 0.7$ . This behaviour, as discussed in [Sabatucci et al. \(2022\)](#), tends to be in tension with the posteriors of  $\alpha$  obtained from NICER collaboration mass and radius pulsar data ([Riley et al., 2019](#)). In the following we propose a possible solution based on the work of [Gamba et al. \(2021\)](#).

**A possible way out.** In [Gamba et al. \(2021\)](#) the authors explore the role of waveform approximants in introducing non-negligible systematic errors on the tidal parameters inferred from GWs. Indeed they re-analyze the strain data of GW170817 using a configuration similar to the one adopted in [Romero-Shaw et al. \(2020\)](#) but imposing a frequency cutoff at  $f_{max} \sim 1024$  kHz (instead of the 2048 Hz of [Romero-Shaw et al. \(2020\)](#)). This is achieved by lowering the sampling frequency from  $f_{samp} = 4096$  Hz to  $f_{samp} = 2048$  Hz, with  $f_{samp}$  defining the Nyquist frequency of the signal.

Interestingly, having excluded frequencies  $\gtrsim 1$  kHz, the recovered posterior for  $\tilde{\Lambda}$  does not show the double peak structure of [Romero-Shaw et al. \(2020\)](#) but instead the distribution shows a single peak at  $\tilde{\Lambda} \sim 500$ . Moreover, [Gamba et al. \(2021\)](#) show that the evidence of the match between the data and the approximant used, `IMRPhenomPv2_NRTidal`, does not improve significantly when increasing the

cut-off from  $f_{max} \sim 1$  kHz to  $f_{max} \sim 2$  kHz. This suggests that negligible SNR is accumulated in the range above  $\sim 1$  kHz and that the double peak structure is most likely caused by high frequency noise fluctuations rather than to a physically motivated effects.

In the following, we have repeated the analysis in Gamba et al. (2021) using the priors and hyperparameters specified in Tab. 5.10 and sampling the parameter space with `dynesty` (1000 live points). Note that we have marginalized analytically over the geocentric time, coalescence phase and luminosity distance. The obtained posterior for  $\tilde{\Lambda}$  is presented in Fig. 5.25. Similarly to Gamba et al. (2021), the posterior presents a single peak around  $\tilde{\Lambda} \sim 500$ . The obtained posterior of  $\tilde{\Lambda}$  is used to perform an alternative estimate of the posterior distribution of  $\alpha$  which is presented in Fig. 5.24 in blue. As expected the double peak structure also disappears for the distribution of  $\alpha$ . Moreover, the posterior's peak shifts to higher values of  $\alpha$  becoming compatible to the ones obtained in Sabatucci et al. (2022) from NICER data. The new multimessenger distribution obtained for  $\alpha$  (Fig. 5.23 in pink) also results compatible, with the posteriors in Sabatucci et al. (2022) although the contribution of the kilonova slightly moves the median towards lower  $\alpha$ .

parameter	prior
$\mathcal{M}_{chirp}$	Uniform(1.18,1.21) $M_\odot$
$q = m_2/m_1 \leq 1$	Uniform(0.125,1)
$\chi_{1z,2z}$	<code>bilby.gw.prior.AlignedSpin(0,0.05)</code>
$\tilde{\Lambda}$	Uniform(0,5000)
$\delta\tilde{\Lambda}$	Uniform(-5000,5000)
$d_L$	Uniform in comoving volume, $\in [10, 100]$ Mpc
$\cos \theta_{JN}$	Uniform(-1,1)
right ascension	3.44616 rad
declination	-0.408084 rad
hyperparameter	value
$f_{min}$	25 Hz
$f_{max}$	2048 Hz
duration	128 s
trigger GPS time	1187008882.43

**Table 5.10.** Priors and hyperparameters used in the re-analysis of GW170817 strain data inspired by Gamba et al. (2021). Note that  $\mathcal{M}_{chirp}$  is the chirp mass in the detector-reference frame,  $q$  is the mass ratio,  $\chi_{1z,2z}$  are the spins projections on the angular momentum direction,  $\tilde{\Lambda}$  and  $\delta\tilde{\Lambda}$  are the tidal parameters,  $d_L$  is the luminosity distance and  $\theta_{JN}$  is the inclination of the binary with respect to the line of sight.

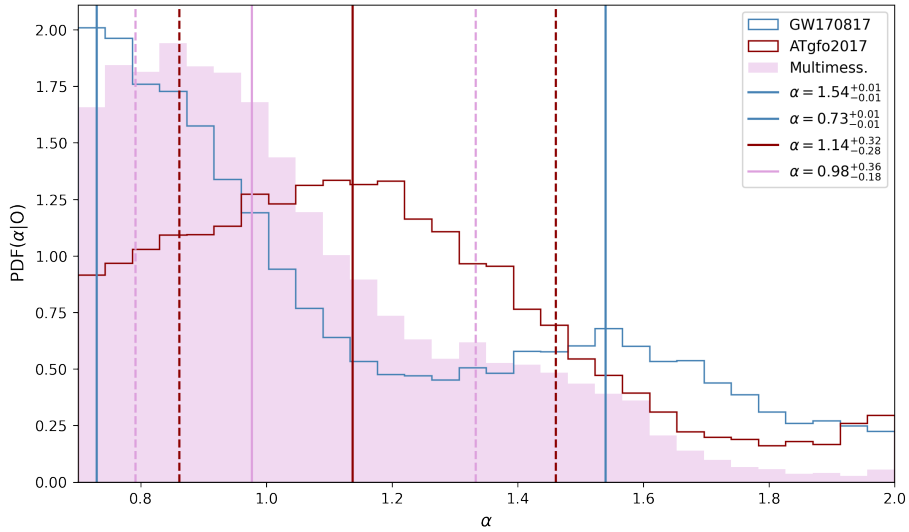


**Figure 5.23.** Posterior distribution of  $\alpha$  obtained from GW170817 analysis (blue), AT2017gfo analysis (red) and the multimessenger analysis (pink). The vertical lines denote the medians (solid) and 68% intervals (dashed) of the distributions, with the exception of the blue lines which denote the modes of the bimodal distribution obtained for GW170817 case. The value of the modes and their standard deviations were obtained by fitting the samples with a double gaussian.

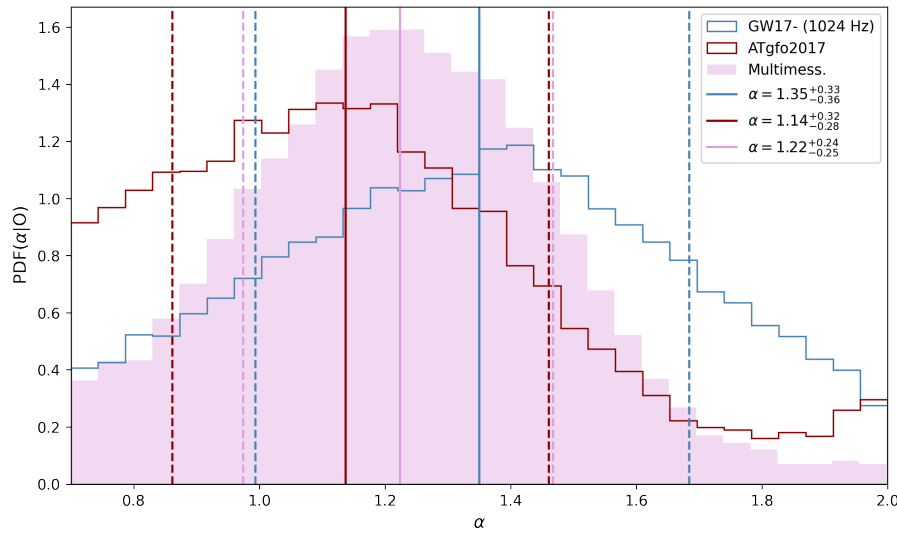


**Figure 5.24.** Posterior distribution of  $\alpha$  obtained from GW170817 re-analysis (blue), AT2017gfo analysis (red) and the multimessenger analysis (pink) fixing a frequency cut-off to 1024 Hz as in [Gamba et al. \(2021\)](#). The vertical lines denote the medians (solid) and the 68 % credible interval (dashed) of the distributions.

$f_{\text{samp}} = 4096 \text{ Hz}$	median
GW170817	$1.00^{+0.57}_{-0.22}$
Multimessenger	$0.98^{+0.36}_{-0.18}$
$f_{\text{samp}} = 2048 \text{ Hz}$	median
GW170817	$1.35^{+0.33}_{-0.36}$
Multimessenger	$1.22^{+0.24}_{-0.25}$

**Table 5.11.** 68% credible intervals around the median values recovered from  $\alpha$  posteriors obtained from GW170817 data and its combined study with AT2017gfo data.

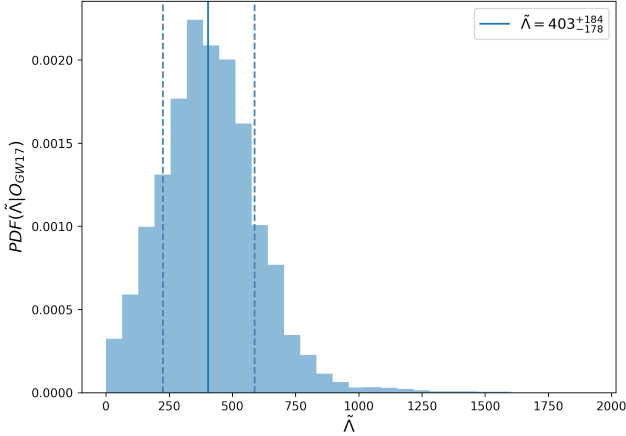


**Figure 5.25.** Posterior distribution of  $\tilde{\Lambda}$  obtained from the re-analysis of GW170817 strain data inspired by [Gamba et al. \(2021\)](#). The vertical lines denote the median (solid) and 68% interval (dashed) of the distribution.

### 5.3.2 Mock data

In the following we will repeat the analysis in [5.3.1](#) using the posteriors of  $\tilde{\Lambda}$  and  $\eta$  obtained in [5.1.2](#) and [5.2.3](#). More specifically, we will be using (i)  $\tilde{\Lambda}$  and  $\eta$  posteriors obtained from the injections of GW170817 mock signals in the HLV network and (ii)  $\tilde{\Lambda}$  and  $\eta$  posteriors obtained from the  $m_{ej}^D$  and  $v_{ej}^D$  distributions related to GW170817 mock kilonovae. We are now interested in quantifying the contributions of each of the two messengers to the final distribution of  $\alpha$ .

The multimessenger distribution of  $\alpha$  is presented in red in Figure [5.26](#) for the injection  $\alpha = 1$  (Figure [5.26a](#)) and  $\alpha = 1.5$  (Figure [5.26b](#)). In blue and yellow are presented, respectively, the posterior of  $\alpha$  retrieved from GW170817 and AT2017gfo mock signals individually. In Fig. [5.26](#) we can observe that, for both injections, the final multimessenger posterior is dominated by the contribution of the GW mock signals and the estimate of  $\alpha$  is  $\sim 7$  times more accurate in GW170817 case compared to AT2017gfo (see values reported in Table [5.7](#) and [5.9](#)).

Indeed, the procedure through which the  $\alpha$  distribution is recovered from the photometric data of the kilonova (see [5.17](#)) is predominantly affected by the uncer-

tainties on the NR fitted formula. These errors are mainly related to our incomplete knowledge on the processes behind the kilonova and the lack of observational data. However, this also underlines the importance for more sensitive instruments both in the electromagnetic band and the GW band. Following the advancement of GW interferometers new detections of NS-NS mergers will be observable, opening to the possibility of studying kilonovae emissions in different mass and distance ranges and broadening our understanding on the information they carry.

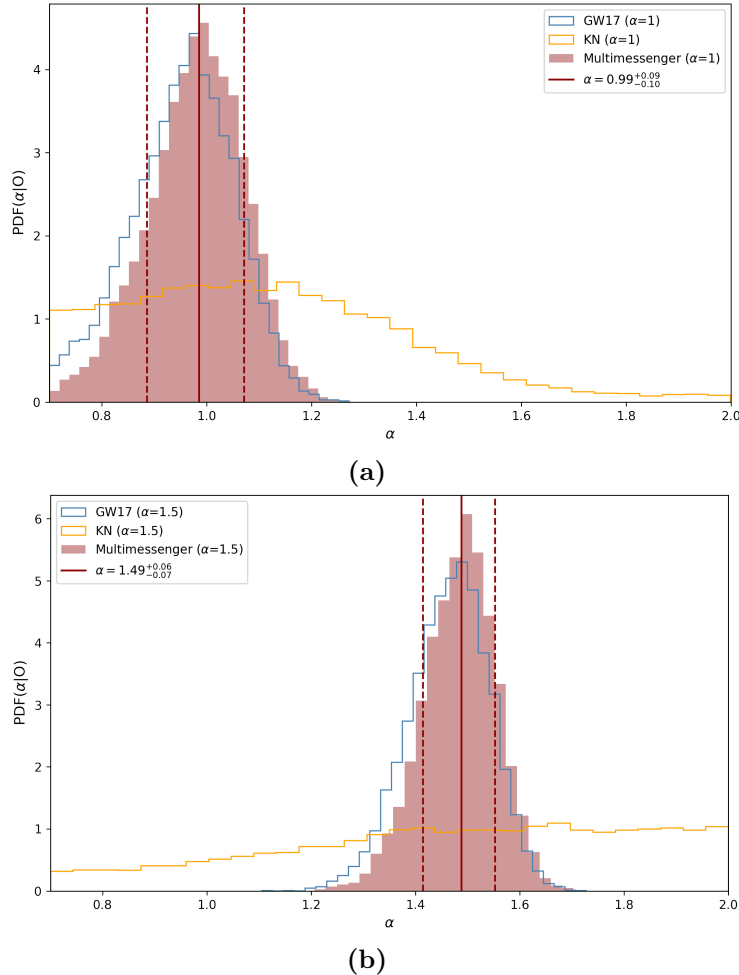


**Figure 5.26.** Posterior distribution of  $\alpha$  obtained from GW170817 mock signal analysis (blue), AT2017gfo mock signal analysis (red) and their multimessenger analysis (pink). The vertical lines denote the medians (solid) and 68 % credible intervals (dashed) of the distributions.

# Chapter 6

## Conclusions

In this work we studied a variety of approaches to infer the properties of NS nuclear matter from the signals produced by NS-NS mergers. In particular, our goal was to exploit the emission of these events powered in different bandwidths, to build a numerical pipeline which combines the information carried by the GW produced during the inspiral, with the postmerger kilonova emission, within the framework of Multimessenger Astrophysics. This was achieved by taking advantage of strategies developed in [Sabatucci et al. \(2022\)](#) and [Breschi et al. \(2021\)](#) and by defining a novel approach to infer joint constraints on a specific microphysical property of the stellar equation of state, i.e. the amplitude of three nucleon repulsive interactions at supranuclear densities. We have applied such strategy to simulated and real events, focusing in particular on the data obtained for the first binary NS event, GW170817, and its kilonova counterpart, AT2017gfo.

As reviewed in Chapter 2, the microscopic behaviour of NS matter, encoded by the EoS, ultimately determines the star observable features, such as its mass, radius and tidal deformability. The latter describes the response of the NS to external tidal fields, which we discussed in a Newtonian and a Relativistic frame in Section 2.4. Tidal fields play a central role in the late stages of evolution of coalescing NS systems, as they are strong enough to modify the binary orbital evolution and its GW emission. Such effects are discussed in Chapter 3, in which we described how tidal interactions affect the ejection of the neutron-rich material which produces the kilonova, and leave a measurable imprint on the inspiral GW emission through the tidal parameters  $\tilde{\Lambda}$  (3.5) and  $\delta\tilde{\Lambda}$  (3.6). These quantities, therefore, represent promising channels of information on the EoS, which is still highly uncertain for densities larger than nuclear saturation expected within stellar cores.

We focused on a specific EoS based on a non-relativistic many body nuclear model, described in Section 2.3. This EoS was modified as in [Maselli et al. \(2021\)](#) by introducing a free parameter, dubbed  $\alpha$ , which determines the strength of the three-body nucleon interactions, largely unconstrained by nuclear experiments above the saturation density. This parameter also controls the EoS stiffness and thus, the magnitude of the NS tidal deformability. One of the goals of the analysis carried out in this thesis was to assess the sensitivity of GW observations to constrain  $\alpha$ , and the improvements that can be achieved in this regard by next-generation interferometers compared to current facilities. For this purpose, after having introduced the statistical framework of Bayesian inference in Chapter 4, we moved to the analysis of the GW inspiral emission focusing first on simulated signals based on the properties of the two events GW170817 and GW190825. Mock signals were injected in the noise

strain of a network composed of LIGO Hanford, LIGO Livingston and Virgo at O4 design sensitivity, and of the Einstein telescope, a 3rd generation interferometer expected to be online by mid 2030s. We assumed for such simulations two values of  $\alpha$ , corresponding to soft and stiff EoS, finding no significant differences in the performance of the binary parameters estimation.

As a first step we recovered from the signals some of the NS-NS binary parameters, namely their chirp mass, spins, symmetric mass ratio and tidal coefficients  $\tilde{\Lambda}$  and  $\delta\tilde{\Lambda}$ , using `bilby`, a numerical pipeline for GW Bayesian inference. Our results show that measurements of  $\tilde{\Lambda}$  significantly benefit from the introduction of ET. For the case of GW170817 the uncertainty on this parameter at 68% credible interval decreases from  $\sim 10\%$  to  $\sim 5\%-4\%$ , while for the case of GW190425 the change is even more dramatic. Indeed, for the second binary event the tidal deformability is basically unconstrained by HLV observations while it is constrained with an uncertainty of  $\sim 17\%$  at 68 % credible interval for the injection in ET. On the other hand, regardless of the type of interferometer taken into account, no significant bounds could be inferred on the tidal parameter  $\delta\tilde{\Lambda}$ , which leads in general to a small effect on the GW phase.

Next, we have used the Fortran code described in Section 4.5 which implements the methodology proposed by [Sabatucci et al. \(2022\)](#), to perform the posterior sampling of the three-body nuclear force amplitude from the posteriors obtained in `bilby` for the binary tidal deformability  $\tilde{\Lambda}$  and the symmetric mass ratio  $\eta$ . We have observed that the improvements led by the introduction of ET on the posterior of  $\tilde{\Lambda}$  have a clear effect on the accuracy to which the injected value of  $\alpha$  is recovered. For the case of GW170817 mock signals, the uncertainty at 68% credible interval on the value of  $\alpha$  decreases approximately of a factor 3 passing from the injections in the HLV network to the ones in ET (from  $\sim 10\%$  to  $\sim 3\%-4\%$ ). On the other hand, no significant constraint is posed on  $\alpha$  for the injections of GW190425 in the HLV network, similarly to what was observed for the recovered posterior of  $\tilde{\Lambda}$ . However, when the mock signals are injected in ET,  $\alpha$  is recovered with an uncertainty of  $\sim 10\%$  at 68% credible interval. This analysis support and strengthen the idea that 3rd generation interferometers will represent a turning point on our understanding of nuclear matter in the extreme densities reached in NSs cores.

In Section 5.2 we have explored a generalization of the numerical pipeline implemented for the GW inference to the case of the kilonova AT2017gfo in order to assess its sensitivity to the nuclear properties of the NS internal composition. To this aim we exploited the results of [Breschi et al. \(2021\)](#) which, assuming an anisotropic 3-component ejecta model, retrieved the posterior distributions of the mass and velocity of the dynamical ejecta,  $m_{ej}^D$  and  $v_{ej}^D$ , from the photometric data of AT2017gfo. Posteriors for  $m_{ej}^D$  and  $v_{ej}^D$  can be mapped into posteriors of  $\tilde{\Lambda}$  and the mass ratio  $q$  exploiting semi-analytic relations based on numerical relativity simulations ([Nedora et al., 2021](#)). In this work we have reproduced the method described in [Breschi et al. \(2021\)](#) developing an independent Python code which implements the sampling of the posteriors of  $m_{ej}^D$  and  $v_{ej}^D$  derived from AT2017gfo to obtain the posteriors of  $\tilde{\Lambda}$  and  $q$ . After testing the compatibility of our results with those originally derived by [Breschi et al. \(2021\)](#), we used such data to infer the posterior of  $\alpha$ . The latter showed that AT2017gfo tends to exclude very large values of the three-body amplitude ( $\gtrsim 1.57$ ), i.e. very stiff EoSs. Next, we extended this analysis to mock kilonovae signals, based on events with masses and spins similar to those of GW170817 and GW190425, and assuming an equation of state with either  $\alpha = 1$  or  $\alpha = 1.5$ . While the results for GW170817 mock signals showed to be informative on the injected value of  $\alpha$ , the posteriors obtained for GW190425

tended to mimic the prior bounds on the parameter, i.e to be uninformative.

In Section 5.3 we defined and implemented a new numerical pipeline through which we (i) combined the information carried by the observed strain data of GW170817 in the O2 run and the photometric data of AT2017gfo analysed in Section 5.2, and (ii) attempted a generalization to the case of the mock GW and kilonovae signals studied for GW170817. For the strain data of GW170817 in (i) we evaluated the data likelihood as in [Sabatucci et al. \(2022\)](#) and found that the obtained posterior for  $\alpha$  for the GW data alone struggled to pose accurate bounds on the value of  $\alpha$ , with the posterior being sharply peaked around the lower bound at  $\alpha = 0.7$  set by the prior. Moreover, our results seem in tension with the posteriors derived in [Sabatucci et al. \(2022\)](#) from data collected by NICER observations of rotating pulsars, which suggest a value of  $\alpha$  around  $\sim 1.4$ . We tried to tackle this problem and alleviate the tension on  $\alpha$  by exploiting a recent study of [Gamba et al. \(2021\)](#) where the authors showed that the posterior obtained in [Abbott et al. \(2019\)](#) could be affected by non-negligible waveform systematics at high frequencies. The latter can be mitigated by lowering the sampling frequency of the signal from  $\sim 4$  kHz to  $\sim 2$  kHz. We repeated all our analysis using such frequency configuration, finding a new posterior on  $\alpha$  from the GW strain data of GW170817 which presents a single peak, fully compatible with the results inferred in [Sabatucci et al. \(2022\)](#) from NICER data. Moreover, the multimessenger distribution for  $\alpha$  resulting from the combination of this posterior with the one we inferred for AT2017gfo alone also results to be compatible within the 68% intervals with the pulsar data.

Next, in (ii) we combined the posteriors obtained for the injections of GW170817 mock signals into the HLV network with the ones obtained for GW170817 mock kilonovae in Section 5.2 to assess the individual contributions of the two signals to the multimessenger estimate of  $\alpha$ . Overall, the final posterior resulted dominated by the contribution of the GW data. This can be interpreted as a consequence of the lack of observational data on NS-NS mergers and kilonovae, which hamper an accurate description of the the kilonova features in terms of binary properties, free of modelling systematics. These sources of uncertainty are expected to be eventually reduced with the introduction of more sensitive instruments in the GW and EM band and the observations of new NS-NS mergers events.

The studies carried out in this work lay the ground for the development of a comprehensive data analysis strategy which takes into account all possible signals emitted by the coalescence, leading to a complete and accurate anatomy of binary neutron star mergers. In this perspective, further applications of our approach can be pursued following multiple directions. For instance, a natural extension of this work would be the inclusion of the post-merger signal of NS-NS mergers which remains unobserved for current detectors but represents a promising target for next-generation interferometers. Indeed, if a NS-NS merger results in a long-lived NS remnant the latter is expected to present a typical emission at  $\sim 1.5\text{-}4$  kHz, which corresponds to the oscillation frequency of the so called  $f_2$  mode. The latter represents an interesting channel of information for the "hot" EoS of the remnant and a few approaches have been already tested for the combined analysis of the inspiral and the post-merger signal (e.g. [Wijngaarden et al. \(2022\)](#)). For what concerns the electromagnetic emission of NS-NS mergers, the GRB produced after the merger could also provide new insights on the properties of NSs and their EoS (see for instance [Coughlin et al. \(2019\)](#)). Finally, all these data could be combined exploiting further sources, alternative to NS-NS mergers, as the pulsars observed by the NICER satellite (see [Maselli et al. \(2021\)](#) and [Sabatucci et al. \(2022\)](#); [Raaijmakers et al.](#)

(2021)), for a genuine multiband and multimessenger investigation of the nuclear matter microphsyical properties.

## Appendix A

# Example code in bilby

In the following we review step-by-step the code used for the benchmark injection of GW170817 mentioned in [5.1.1](#).

**Injection parameters.** First, we define the *injection parameters*, i.e. the properties of the binary system which define the GW signal:

```
injection_parameters = dict(
    mass_1_source=1.48, mass_2_source=1.26,\n
    chi_1=0., chi_2=0., luminosity_distance=40,\n
    theta_jn=2.56, psi=2.659, phase=1.3,\n
    geocent_time=1187008882.43,\n
    ra=1.097*np.pi, dec=-0.13*np.pi,\n
    lambda_1=183, lambda_2=505)
```

Here `mass_1_source`, `mass_2_source` and `chi_1`, `chi_2` are the stellar masses in solar-mass units in the source reference frame<sup>1</sup> and the dimensionless spin parameters; `luminosity_distance` is the luminosity distance in Mpc; `theta_jn`, `psi`, `phase` are the inclination angle between the observer line of sight and the orbital angular momentum, the polarisation angle, and the phase of the GW; `geocent_time` is the geocentric time at which the coalescence happens; `ra`, `dec` are the right ascension and declination of the source and `lambda_1`, `lambda_2` are the stars tidal deformabilities. The phase, spins, and inclination angles are all defined at some reference frequency ([Romero-Shaw et al., 2020](#)) (see **Waveform parameters** paragraph). Other parameters available in `bilby` describing a compact binary are listed in Tab. [A.2](#) and [A.3](#). Note that `injection_parameters` is a dictionary (`dict`) object. Dictionaries are frequently used in `bilby`. For instance, the priors of the various parameters will be defined within a dictionary (see **Parameter estimation** paragraph).

**Waveform duration and sampling frequency.** The next step is setting the duration of the injected signal, the sampling frequency and the time at which the waveform has to be generated<sup>2</sup>:

```
duration = 2 * 32\nsampling_frequency = 4 * 1024\nstart_time = injection_parameters['geocent_time'] + 2 - duration
```

---

<sup>1</sup>To set the value of the two masses in the interferometers reference frame we should have written instead `mass_1`, `mass_2`.

<sup>2</sup>The times are measured in seconds and the frequencies in Hz.

---

Note that the duration of the signal is fixed to be 64s, of which 2s past the geocentric time (the merger). The sampling frequency and the duration of the signal must be taken into account when considering the computational costs of producing the injected waveform. In fact, although the sampling frequency should be high enough to clearly depict the frequency-evolution of the signal, having a high sampling frequency and a long duration of the signal means more computational costs<sup>3</sup>.

**Waveform parameters.** Then, we need to specify some parameters concerning the numerical waveform that is going to be generated:

```
fmin = 30.
waveform_arguments = dict(
    waveform_approximant='TaylorF2',
    reference_frequency=50., minimum_frequency=fmin
)
```

The waveform approximant represents the model based on which the waveform is generated from the binary parameters. Different approximants are available based on the physical effects they account for and/or on the different approximations they rely on. The reference frequency, as mentioned in **Injection Parameters**, is the frequency to which some of the injection parameters are defined (e.g. the spins). Finally, the minimum frequency represents the starting frequency of the waveform. In our case it is fixed to 30 Hz.

These parameters, as well as the ones defined in the previous paragraphs, are used to produce the mock signal through the waveform generator:

```
waveform_generator = bilby.gw.WaveformGenerator(
    duration=duration, sampling_frequency=sampling_frequency,
    frequency_domain_source_model=
    bilby.gw.source.lal_binary_neutron_star,
    parameter_conversion=
    bilby.gw.conversion.convert_to_lal_binary_neutron_star_parameters,
    waveform_arguments=waveform_arguments)
```

In the `waveform_generator` definition are mentioned two additional input parameters to the ones we have already discussed: `frequency_domain_source_model` and `parameter_conversion`. The former is a function producing the frequency-domain strain of the GW emitted from the signal injection parameters and the waveform arguments discussed before<sup>4</sup>, while the latter translates the set of parameters defined in `bilby` to the parameters defined in `lalsuite`, the LIGO Scientific Collaboration Algorithm Library for gravitational-wave analysis (documentation at the [link](#)). Note that `waveform_generator` produces the waveform polarisations independently of the interferometer.

**Interferometers.** Let us set the interferometers in which we want to inject the signal:

```
interferometers = bilby.gw.detector.InterferometerList(
    ['H1', 'L1', 'V1'])
```

---

<sup>3</sup>This is why producing NS-NS coalescence waveforms is more costly from a computational perspective than producing BH-BH coalescence waveforms: the former remain longer in the sensitivity curves of the detectors (long duration) and their GW emission peaks at frequencies of  $\mathcal{O}(\text{kHz})$  (high sampling frequency required).

<sup>4</sup>One can alternatively define a `time_domain_source_model` and get the time-domain strain.

---

The interferometers network is made up by LIGO Hanford (H1), LIGO Livingston (L1) and Virgo (V1). By default these interferometers operate at design sensitivity and their properties (the minimum/maximum frequency detectable, the power spectral density etc.) are listed in bilby repository documentation ([link](#)). However, these default properties can be changed manually. For instance, in our case we need to use the PSDs released on GWOSC for the detection of GW170817 in the O2 run ([link](#)):

```
interferometers[0].power_spectral_density =
    bilby.gw.detector.PowerSpectralDensity(psd_file=path_psd_LIGOH)

interferometers[1].power_spectral_density =
    bilby.gw.detector.PowerSpectralDensity(psd_file=path_psd_LIGOL)

interferometers[2].power_spectral_density =
    bilby.gw.detector.PowerSpectralDensity(psd_file=path_psd_Virgo)
```

Note that `path_psd_LIGOH`, `path_psd_LIGOL` and `path_psd_Virgo` represent three strings containing the paths of the PSD files of the interferometers. The latter must be formatted as following: one column listing the frequencies in Hz (to which the interferometer is sensitive), and a second column listing the corresponding PSD value. Furthermore, we require the minimum frequency of the detectors to be the same as that of the injected waveform:

```
for ifo in interferometers:
    ifo.minimum_frequency = fmin
```

After having defined the interferometers properties, we need to set the noise. For instance, one can sample the noise directly from the PSD curve:

```
interferometers.set_strain_data_from_power_spectral_densities(
    sampling_frequency=sampling_frequency, duration=duration,
    start_time=start_time)
```

Note that the `set_strain_data_from_power_spectral_densities` returns a vector containing the noise strain of the interferometer sampled at `sampling_frequency` over an interval of time long `duration`. In our case, however, we are interested in performing a zero-noise injection:

```
interferometers.set_strain_data_from_zero_noise(
    sampling_frequency=sampling_frequency, duration=duration,
    start_time=start_time)
```

Moreover, we fix the random seed value right before the `interferometers.set_strain_data_from_power_spectral_densities` call:

```
np.random.seed(10201238)
```

This is optional but it is done to guarantee the reproducibility of our analysis.

**Signal injection.** To inject the signal in the interferometers network we write:

```
interferometers.inject_signal(
    parameters=InjectionParameters,
    waveform_generator=waveform_generator)
```

---

While to print out the strain detected by the three interferometers one can specify:

```
for ifo in interferometers:
    print(ifo.strain_data.time_domain_strain)
    print('\n')
```

Note that, before the injection, the object `ifo.strain_data` contains the noise strain of the interferometer.

**Parameter estimation.** Having injected the signal in the network, we now review how to recover the posteriors of the binary parameters we are interested in.

First, we define a dictionary object that contains the definitions of each parameter's prior:

```
priors = bilby.gw.prior.BNSPriorDict()
```

Here we have used one of the standard prior dictionaries available in `bilby.gw.prior(BNSPriorDict)` whose keys are set to be the parameters defining a binary NS system (source code available at this [link](#)).

Next, since we are not interested in sampling the inclination angle, the polarisation angle, the right ascension and the declination, we write:

```
for key in ['psi', 'ra', 'dec', 'theta_jn']:
    priors[key] = injection_parameters[key]
```

This way we are setting the values of these parameters to be equal to their injected value, i.e. the prior is a delta function at the true, injected value. By not sampling this subset of parameters we significantly reduce the computational cost of the posteriors sampling procedure, while not invalidating the estimate of the other parameters posteriors. Infact, the angular parameters are not strongly correlated to the physical parameters that will be recovered and that characterize the binary system.

If we want to cut out some parameters from the parameters space then we can use the Python `pop()` built-in function on the the priors dictionary:

```
priors.pop('mass_1')
priors.pop('mass_2')
priors.pop('lambda_1')
priors.pop('lambda_2')
priors.pop('mass_ratio')
```

Finally, we set the priors of the remaining parameters:

```
priors['chirp_mass'] = bilby.core.prior.Uniform(
    1., 1.4, name='chirp_mass', unit='M_{\dot{}}')

priors['symmetric_mass_ratio'] = bilby.core.prior.Uniform(
    0.18, 0.25, name='symmetric_mass_ratio')

priors['lambda_tilde'] = bilby.core.prior.Uniform(0, 5000,
    name='lambda_tilde')

priors['delta_lambda_tilde'] = bilby.core.prior.Uniform(-5000, 5000,
    name='delta_lambda_tilde')
```

---

```
priors['lambda_1'] = bilby.core.prior.Constraint(minimum=0,maximum=5000)
priors['lambda_2'] = bilby.core.prior.Constraint(minimum=0,maximum=5000)
priors['chi_1'] = bilby.core.prior.Uniform(-0.05, 0.05, name='chi_1')
priors['chi_2'] = bilby.core.prior.Uniform(-0.05, 0.05, name='chi_2')

priors['luminosity_distance'] = bilby.gw.prior.UniformSourceFrame(
    name='luminosity_distance', minimum=20., maximum=1e2)
```

Here we have exploited some of the standard prior classes available in `bilby`. The `Uniform` prior function returns a uniform distribution between the lower and upper bounds specified as input parameters, while the `Constraint` prior function is used to remove portions of the parameters space by setting constraints on the range of possible values of a certain parameter. For instance, in this case we are reducing the parameters space volume of `lambda_tilde`, `delta_lambda_tilde` by constraining the possible values for `lambda1`, `lambda2`. In order for this to work one must additionally specify the conversion relation between the constrained parameters and the sampled ones. In our case a default conversion function between the tidal parameters is defined within the `BNSPriorDict` object<sup>5</sup>. The `name` and `unit` optional inputs are specified to assign the labels that will be plotted along with the posterior of the sampled parameters.

We now move to define the data likelihood:

```
likelihood = bilby.gw.GravitationalWaveTransient(
    interferometers=interferometers,
    waveform_generator=waveform_generator,
    time_marginalization=True, phase_marginalization=True,
    distance_marginalization=True, priors=priors)
```

Here we are using the `GravitationalWaveTransient` function which computes the log-likelihood in the frequency domain assuming a colored Gaussian noise model (Thrane & Talbot, 2019). Note that we are marginalizing the likelihood over the time of coalescence, phase and luminosity distance in order to reduce the runtime.

**Posterior sampling.** Having defined the priors and the likelihood, we can move to sampling the parameter space:

```
result = bilby.run_sampler(
    likelihood=likelihood, priors=priors,
    sampler='dynesty', npoints=1000,
    injection_parameters=injection_parameters,
    outdir='outdir', label='run_benchmarkGW17',
    conversion_function=
        bilby.gw.conversion.generate_all_bns_parameters)
```

Note that the we are using `bilby` built-in `dynesty` fixing the number of live points to 1000 (Speagle, 2020). Finally, to produce the corner plot of the results shown in Fig. A.1 we must specify:

---

<sup>5</sup>Within a `BNSPriorDict` object there are also default conversion functions for the mass parameters.

---

```
result.plot_corner()
```

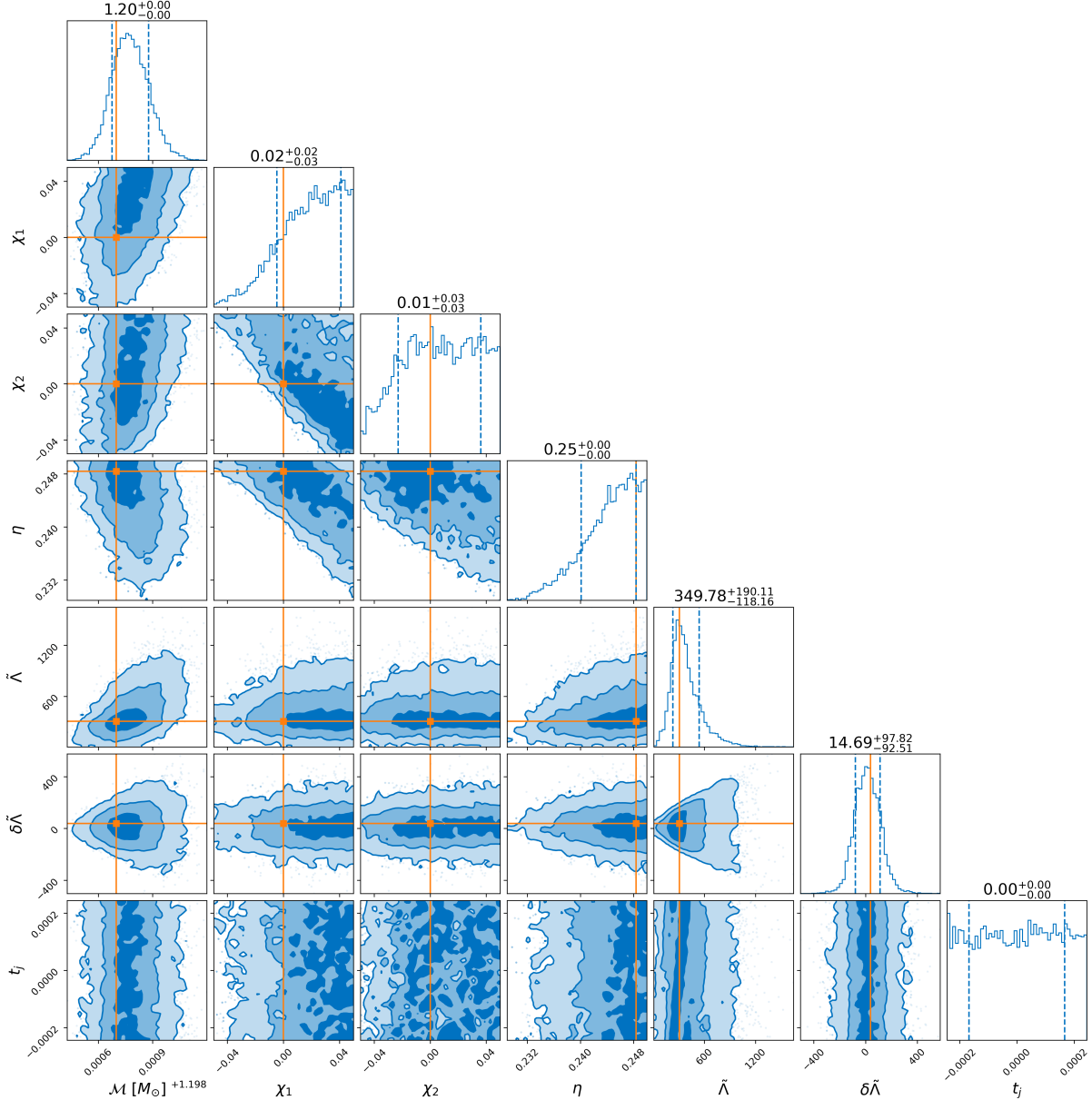


**Figure A.1.** Corner plot produced for the tutorial. The injected parameters are compatible with the properties of event GW170817.

Name	Description	LATEX label	Units
mass_i	Detector-frame (redshifted) mass of the $i$ th object	$m_i$	$M_\odot$
chirp_mass	Detector-frame chirp mass $\mathcal{M} = (m_1 m_2)^{3/5}/(m_1 + m_2)^{1/5}$ (Finn & Chernoff 1993; Poisson & Will 1995; Blanchet et al. 1995)	$\mathcal{M}$	$M_\odot$
total_mass	Detector-frame combined mass of the primary and secondary masses	$M$	$M_\odot$
mass_ratio	The ratio of the secondary and primary masses $q = m_2/m_1 \leq 1$	$q$	–
symmetric_mass_ratio	A definition of mass ratio which is independent of the identity of the primary/secondary $\eta = q/(1+q)^2$	$\eta$	–
mass_i_source	Source-frame mass of the $i$ th object $m_i^{\text{source}} = m_i/(1+z)$ (Krolak & Schutz 1987)	$m_i^{\text{source}}$	$M_\odot$
chirp_mass_source	Source-frame chirp mass $\mathcal{M}^{\text{source}} = \mathcal{M}/(1+z)$	$\mathcal{M}^{\text{source}}$	$M_\odot$
total_mass_source	Source-frame total mass $M^{\text{source}} = M/(1+z)$	$M^{\text{source}}$	$M_\odot$
a_i	Dimensionless spin magnitude of the $i$ th object	$a_i$	–
tilt_i*	Zenith angle between the spin and orbital angular momenta for the $i$ th object	$\theta_i$	rad
cos_tilt_i*	Cosine of the zenith angle between the spin and orbital angular momenta for the $i$ th object	$\cos \theta_i$	–
phi_jl1*	Difference between total and orbital angular momentum azimuthal angles	$\phi_{\text{JL}}$	rad
phi_l2*	Difference between the azimuthal angles of the individual spin vector projections on to the orbital plane	$\phi_{12}$	rad
chi_i* (a.k.a. spin_i_z)	$i$ th object aligned spin: projection of the $i$ th object spin on to the orbital angular momentum $\chi_i = a_i \cos(\theta_i)$	$\chi_i$	–

**Figure A.2.** Tab E1 from Romero-Shaw et al. (2020) in which are reported the definitions of parameters typically considered for compact binary coalescences inference in `bilby`. Subscript  $i = 1, 2$  indicates whether the parameter refers to the primary (1) or secondary (2) binary object. Subscript  $k = x, y, z$  refers to a quantity measured in the  $x, y$ , or  $z$  direction;  $z$  points along the binary axis of rotation, while the  $x, y$  directions are orthogonal to each other and  $z$ . Additional subscripts: \* – defined at a reference frequency, † – parameter cannot be sampled, only generated in post-processing, × – parameter cannot yet be sampled or generated in post-processing.

Name	Description	LATEX label	Units
chi_i_in_plane*†	$i$ th object in-plane spin: magnitude of the projection of the $i$ th object spin on to the orbital plane $\chi_i^\perp =  a_i \sin(\theta_i) $	$\chi_i^\perp$	–
chi_eff*†	Effective inspiral spin parameter $\chi_{\text{eff}} = (\chi_1 + q\chi_2)/(1+q)$ (Santamaría et al. 2010; Ajith et al. 2011)	$\chi_{\text{eff}}$	–
chi_p*†	Effective precession spin parameter $\chi_p = \max\{\chi_1^\perp, q(3q+4)/(4q+3)\chi_2^\perp\}$ (Hannam et al. 2014; Schmidt, Ohme & Hannam 2015)	$\chi_p$	–
spin_i_k*†	$k$ th component of $i$ th object spin in Euclidean coordinates	$S_{i,k}$	–
lambda_da_i	Dimensionless tidal deformability of the $i$ th object	$\Lambda_i$	–
lambda_tilde	Combined dimensionless tidal deformability (Flanagan & Hinderer 2008; Favata 2014)	$\bar{\Lambda}$	–
delta_lambda_tilde	Relative difference in the combined tidal deformability (Favata 2014; Wade et al. 2014)	$\delta \bar{\Lambda}$	–
eccentricity*†	Orbital eccentricity defined at a reference frequency	$e$	–
argument_of_periaxis*	The angle between the secondary mass and the ascending node of the orbit when the secondary mass is at periaxis	$\omega$	rad
x	Right ascension	$\alpha$	rad
ra	Declination	$\delta$	rad
dec	Zenith angle in the detector-based sky parametrization	$\kappa$	rad
azimuth	Azimuthal angle in the detector-based sky parametrization	$\epsilon$	rad
luminosity_distance	Luminosity distance to the source	$d_L$	Mpc
comoving_distance	Comoving distance depending on specified cosmology	$d_C$	Mpc
redshift	Redshift depending on specified cosmology	$z$	–
geocent_time	GPS reference time at the geocenter, typically merger time	$t_{\text{c}}$	s
IFO_time	GPS reference time at the detector with name IFO, e.g. H1_time, typically merger time	$t_{\text{IFO}}$	s
time_jitter	Shift to apply for time array used in time marginalization	$\delta t$	s
psi	Polarization angle of the source	$\psi$	rad
phase*	Binary phase at a reference frequency	$\phi$	rad
theta_jn	Zenith angle between the total angular momentum and the line of sight	$\theta_{\text{IN}}$	rad
cos_theta_jn	Cosine of the zenith angle between the total angular momentum and the line of sight	$\cos \theta_{\text{JN}}$	–
iota*	Zenith angle between the orbital angular momentum and the line of sight	$\iota$	rad
cos_iota*	Cosine of the zenith angle between the orbital angular momentum and the line of sight	$\cos \iota$	–

**Figure A.3.** Tab E2 from Romero-Shaw et al. (2020). Same prescriptions as Tab E1 in Fig. A.2.

# Bibliography

- Abbott B. P., et al., 2017a, [The Astrophysical Journal](#), 848, L12
- Abbott B. P., et al., 2017b, [The Astrophysical Journal Letters](#), 848, L13
- Abbott B. P., et al., 2019, [Phys. Rev. X](#), 9, 011001
- Abbott B. P., et al., 2020, [Astrophys. J. Lett.](#), 892, L3
- Angelini M., 2022, Lecture notes on Montecarlo Methods, Available online at :<https://elearning.uniroma1.it/course/view.php?id=7464>
- Arnett W. D., 1982, [The Astrophysical Journal](#), 253, 785
- Ascenzi S., Oganesyan G., Branchesi M., Ciolfi R., 2021, [Journal of Plasma Physics](#), 87, 845870102
- Ashton G., et al., 2019, [The Astrophysical Journal Supplement](#), 241, 27
- Blanchet L., 2014, [Living Reviews in Relativity](#), 17, 2
- Breschi M., Perego A., Bernuzzi S., Del Pozzo W., Nedora V., Radice D., Vescovi D., 2021, [Monthly Notices of the Royal Astronomical Society](#), 505, 1661
- Chatzioannou K., 2020, [General Relativity and Gravitation](#), 52, 109
- Coughlin M. W., Dietrich T., Margalit B., Metzger B. D., 2019, [Monthly Notices of the Royal Astronomical Society: Letters](#), 489, L91
- Cutler C., Flanagan E. E., 1994, [Phys. Rev. D](#), 49, 2658
- Dietrich T., Hinderer T., Samajdar A., 2021, [General Relativity and Gravitation](#), 53, 27
- Faber J. A., Rasio F. A., 2012, [Living Reviews in Relativity](#), 15, 8
- Ferrari V., Gualtieri L., Pani P., 2020, General relativity: the physical theory of gravity with applications to compact objects and gravitational-wave sources. CRC Press, [doi:10.1201/9780429491405](https://doi.org/10.1201/9780429491405)
- Foreman-Mackey D., Hogg D. W., Lang D., Goodman J., 2013, [Publications of the Astronomical Society of the Pacific](#), 125, 306–312
- Gamba R., Breschi M., Bernuzzi S., Agathos M., Nagar A., 2021, [Phys. Rev. D](#), 103, 124015
- Geyer C. J., 1991, In Computing Science and Statistics: Proceedings of 23rd Symposium on the Interface Foundation, p. 8

- Goodman J., Weare J., 2010, *Communications in Applied Mathematics and Computational Science*, 5, 65–80
- Hastings W. K., 1970, *Biometrika*, 57, 97
- Hinderer T., 2008, *The Astrophysical Journal*, 677, 1216–1220
- Hotokezaka K., Kiuchi K., Kyutoku K., Muranushi T., Sekiguchi Y.-i., Shibata M., Taniguchi K., 2013, *Phys. Rev. D*, 88, 044026
- Kasen D., Metzger B., Barnes J., Quataert E., Ramirez-Ruiz E., 2017, *Nature*, 551, 80–84
- Kippenhahn R., Weigert A., Weiss A., 2012, Stellar Structure and Evolution. Astronomy and Astrophysics Library, Springer Berlin Heidelberg, Berlin, Heidelberg, doi:10.1007/978-3-642-30304-3, <http://link.springer.com/10.1007/978-3-642-30304-3>
- Mapelli M., 2017, Lecture notes on Gravitational Wave Progenitors, Available online at :<http://web.pd.astro.it/mapelli/lectures.html>
- Maselli A., Sabatucci A., Benhar O., 2021, *Physical Review C*, 103, 065804
- Metropolis N., Rosenbluth A. W., Rosenbluth M. N., Teller A. H., Teller E., 1953, *J. Chem. Phys.*, 21, 1087
- Metzger B. D., 2020, *Living Rev Relativ*, 23, 1
- Miller M. C., 2018, Lecture notes on Practical Astrostatistics, Available online at: <https://www.astro.umd.edu/~miller/teaching/astrostat/>
- Nedora V., et al., 2021, *The Astrophysical Journal*, 906, 98
- Pang P. T. H., Tews I., Coughlin M. W., Bulla M., Van Den Broeck C., Dietrich T., 2021, *The Astrophysical Journal*, 922, 14
- Poisson E., Will C. M., 2014, Structure of self-gravitating bodies. Cambridge University Press, p. 63–137, doi:10.1017/CBO9781139507486.003
- Raaijmakers G., et al., 2021, *The Astrophysical Journal Letters*, 918, L29
- Radice D., Perego A., Zappa F., Bernuzzi S., 2018, *The Astrophysical Journal*, 852, L29
- Read J. S., Lackey B. D., Owen B. J., Friedman J. L., 2009, *Phys. Rev. D*, 79, 124032
- Regge T., Wheeler J. A., 1957, *Physical Review*, 108, 1063–1069
- Riley T. E., et al., 2019, *Astrophys. J. Lett.*, 887, L21
- Romero-Shaw I. M., et al., 2020, *Monthly Notices of the Royal Astronomical Society*, 499, 3295
- Sabatucci A., Benhar O., Maselli A., Pacilio C., 2022, arXiv e-prints
- Sharma S., 2017, *Annual Review of Astronomy and Astrophysics*, 55, 213–259

- Speagle J. S., 2020, [Monthly Notices of the Royal Astronomical Society](#), 493, 3132
- Tanaka M., 2016, [Advances in Astronomy](#), 2016, 1–12
- Thorne K. S., Campolattaro A., 1967, Non-Radial Pulsation of General-Relativistic Stellar Models. I. Analytic Analysis for  $L \geq 2$ , [Astrophysical Journal](#), vol. 149, p.591, [doi:10.1086/149288](https://doi.org/10.1086/149288)
- Thrane E., Talbot C., 2019, [Publ. Astron. Soc. Aust.](#), 36, e010
- Tonetto L., Sabatucci A., Benhar O., 2021, [Phys. Rev. D](#), 104, 083034
- Villar V. A., et al., 2017, [Astrophys. J. Lett.](#), 851, L21
- Wijngaarden M., Chatzioannou K., Bauswein A., Clark J. A., Cornish N. J., 2022, [Phys. Rev. D](#), 105, 104019